UNIVERSITÀ DI PISA

DEPARTMENT OF PHYSICS

Master of Science in Physics
Curriculum: Fundamental Interactions

First Measurement of one Pion Production in Charged Current Neutrino and Antineutrino events on Argon

Author:

Giacomo Scanavini

Supervisor:

Dr. Ornella Palamara (Fermilab)

Internal Supervisor:

Prof. Alessandro Baldini (INFN Pisa)

Academic Year

2016 - 2017

Abstract

This thesis presents a work done in the context of the Fermilab Neutrino Intensity Frontier. In this analysis, the cross section of single charged pion production in charged-current neutrino and antineutrino interactions with the argon nucleus target are measured. These measurements are performed using the Argon Neutrino Test (ArgoNeuT) detector exposed to the Fermilab Neutrino From The Main Injector (NuMI) beam operating in the low energy antineutrino mode. The signal is a charged-current ν_μ interaction in the detector, with exactly one charged pion exiting the target nucleus, with momentum above 100 MeV/c. There shouldn't be any π^0 or kaons in the final state. There is no restriction on other mesons or nucleons. Total and differential cross section measurements are presented. The results are reported in terms of outgoing muon angle and momentum, outgoing pion angle and angle between outgoing pion and muon. The total cross sections, averaged over the flux, are found to be 8.2 ± 0.9 (stat) $^{+0.9}_{-1.1}$ (syst) $\times$ 10^{-38} cm^2 per argon nuclei and 2.5 ± 0.4 (stat) ± 0.5 (syst) $\times$ 10^{-37} cm^2 per argon nuclei for antineutrino and neutrino respectively at a mean neutrino energy of 3.6 GeV (antineutrinos) and 9.6 GeV (neutrinos). This is the first time the single pion production in charged-current interactions cross section is measured on argon nuclei.

Acknowledgements

A scientist, like an artist, is touched by the people and experiences that influence him. I wish here to take this occasion to acknowledge people who I have met and somehow contributed to the realization of this work.

First of all, I wish to thank the Neutrino Physics Center and all its coordinators, Dr. Bonnie Fleming, Dr. Deborah Harris and Dr. Stephen Parke for the outstanding fellowship they awarded me which gave me the possibility to spend 5 great months at Fermilab where I conduct the work presented in this thesis.

I am grateful to all members of the ArgoNeuT collaboration for supporting my research activity, for treating me as a colleague from day one, always giving me respect and kindness while teaching me how to do physics and for all the good advice on my work. I especially wish to acknowledge the spokesperson Dr. Mitchell Soderberg for welcoming me in what I personally consider a great group where a young physicist can learn and grow.

Dr. Tingjun Yang is part of this awesome collaboration but he deserves a special treatment. He taught me everything I know on how to conduct a cross section measurement, I had the fortune to work alongside him and I would like to repeat in the future this incredible cooperation because I am sure he has a lot more to teach me. I am very thankful to you for your mentoring. I hope one day to become at least half of the great physicist you are.

I am grateful to my supervisor Prof. Alessandro Baldini for taking the decision to be my internal supervisor and the subsequent patience and time he has spent holding such role. In particular for the help he gave me with my applications to the Ph.D. program.

Dr. Ornella Palamara, you provided me the opportunities to work on this thesis and constantly encouraged me, advised me and believed in me since the summer of 2015 when we first met. You guided me in my first research experiences and helped me set up the next few years of my life. I will always be in debt. Thank you for being such an awesome supervisor and for helping me throughout this work and even more. I look forward to the forthcoming years under your guidance.

Thanks to all the people who shared with me the journey to the great achievement of the Master Degree, in particular Tommaso, a great friend who was able to ease the hard work, with who I shared almost everything in this last period.

Thanks to all my friends, especially my lifetime friends, Amalia, Antonella, Andrea, Cecilia, Cinzia, Cristina, Damiano, Eleonora B., Eleonora R., Emma, Francesco, Michele, Nicola, Samuele, Simone and Viola. My life wouldn't be the same without you all. You are those who better know me and who I mostly want to share this moment with. I hope our friendship never fade, even when I will be away in the next few years. Lorenzo, a special mention goes to you for being the best friend one could possibly wish for.

Last but not least, I would like to seriously thank my family, in particular my parents, for all the effort they put in order to allow me an education and all the support and help they constantly provided me during the realization of this thesis and in my entire life.

Contents

List of Figures

List of Tables

Introduction

Neutrino oscillation is of great theoretical and experimental interest, as the features of the process can shed light on several properties of the neutrino. In particular, it implies that the neutrino has a non-zero mass, which requires a modification to the Standard Model. Although the possibility of neutrino flavor change had been discussed ever since neutrinos were first discovered experimentally in 1956, it was only around the turn of the millennium that two convincing discoveries validated the actual existence of neutrino oscillations: the disappearance of atmospheric μ neutrinos by the Super-Kamiokande experiment, and the evidence for conversion of electron-type neutrinos from the Sun into μ or τ neutrinos by the Sudbury Neutrino Observatory (SNO) experiment. These discoveries are of fundamental importance and constitute a major breakthrough and were recognized with the 2015 Nobel Prize for Physics. Neutrino oscillations and the connected issues of the nature of the neutrino, their masses and possible CP violation among leptons, are today major research topics in particle physics. The Fermi National Laboratory is currently involved in both the Short-Baseline Neutrino (SBN) and the Long-Baseline Neutrino (LBN) physics programs. The former, which brings together three Liquid Argon Time Projection Chamber (LArTPC) detectors has the main goals of resolving a class of experimental anomalies in neutrino physics and performing the most sensitive search to date for sterile neutrinos at the eV mass-scale through both appearance and disappearance oscillation channels. The latter, with a far detector composed of four vast LArTPCs, each of 17 kt of argon mass, will study neutrino oscillations with the most intense high-energy neutrino beam, with a distance of 1300 km between the near and far detectors.

Neutrino oscillation experiments depend critically on an accurate model of neutrino interactions. These models have to predict, not only the signal and background populations that oscillation experiments expect at near and far detectors, but they must also predict how the neutrino energy gets transferred to the particles that leave the nucleus after the neutrino interacts. Cross section measurements are then of fundamental importance to any neutrino oscillation experiment because of the

prediction on the expected number of events. The more precise the cross sections are measured the more accurate the results in neutrino oscillation experiments will be. Since oscillation experiments rely on kton-scale far detectors, they are forced to use common relatively heavy materials such as carbon, water, argon or iron as nucleus target. In the neutrino-nucleus interaction, at the MeV and GeV energy ranges of the accelerator-based neutrino experiments, nuclear effects play a massive role in determining the final state. Even for an element as light as carbon, the nuclear effects are predicted to be substantial. Moreover, they behave very differently from nucleus to nucleus. The whole United States accelerator based neutrino physics program, at both short and long-baselines, will be serving LArTPCs as detectors and the key involvement of argon in these programs arises the necessity to measure neutrino-argon nucleus cross sections with a very high precision.

This thesis presents the measurement of neutrino-argon cross section of charged-current single pion production events with any number of nucleons in the final state. This measurement has never been done before on argon. The calculation of this cross section was realized analyzing data collected by the Argon Neutrino Test (ArgoNeuT) detector, a LArTPC exposed to the Neutrinos at the Main Injector (NuMI) neutrino beam, placed at the Fermi National Laboratory (Fermilab) in the United States, Batavia, Illinois. Currently running and future experiments at Fermilab will carry out the same cross section measurement, improving the results with a higher precision.

The general outline of this thesis is the following, Chapters 1 presents an overview of the current neutrino physics, including how the field of neutrino physics reached its current state, Chapter 2 briefly describes the accelerator complex at Fermilab and Chapter 3 delineates the detector technologies used to achieve this measurement, with a particular focus on the ArgoNeuT detector. Finally, Chapter 4 presents the analysis and the cross section measurement in the ArgoNeuT detector.

Chapter 1

Neutrino Physics

In this Chapter the neutrino is introduced as a particle predicted in the Standard Model, from its postulation to its discovery. Furthermore the main natural and artificial sources of neutrinos are briefly listed and the most important and peculiar behavior of these particles, the neutrino oscillation, is presented with experimental evidences collected by several experiments. Finally the importance and the challenges in neutrino interaction measurements are presented, and some future directions on the possible neutrino field researches are given with examples, results and anomalies of past experiments.

1.1 History of Neutrino Physics

To prevent the violation of the law of energy conservation in the β-decay, a neutral particle, the neutrino, is emitted along with the β particle. The neutrino (ν) was first postulated by Wolfgang Pauli, 1930, in order to explain this phenomenon. Enrico Fermi developed the first theoretical explanation of the β-decay [1], and his theory, the four-point β-decay, required the existence of a neutral particle that he called "neutrino":

$$n \rightarrow p + e^- + \overline{\nu}_e$$

The reaction above is an example of a weak interaction happening at the quark level, where one of the neutron down-quarks converts to an up-quark through the emission of a boson W^-. Due to the chargeless and weak interacting properties of the neutrino, its detection happened only in 1956 by Frederick Reines and Clyde Cowan [2], more than 20 years after its first postulation. A similar interaction to

the β-decay was used in the process to detect the neutrino:

$$p + \overline{\nu}_e \rightarrow n + e^+$$

Unlike neutrinos, neutrons and positrons are relatively easy to observe. Reines and Cowan simply exposed a detector filled with water to a high intensity source of electron antineutrinos, the nuclear reactor at the Savannah River plant in Georgia, USA. The antineutrinos coming from the reactor interacted with the protons in the detector producing a neutron and a positron in each interaction. The event was detected observing the annihilation of the positron with an electron in the water tank, which produces a couple of gamma rays, and the capture of the neutron by a Cadmium nucleus, which was doped in the water tank and emits a gamma ray of energy 2.2 MeV in the de-excitation process, delayed by 5 μs with respect to the electron-positron annihilation. Reines and Cowan observed about three neutrinos per hour in their detector when the reactor was functioning, while, when the reactor was shut off they no longer observed neutrinos. Since the first discovery of the neutrino, neutrinos and their interactions have played a central role in the development of the Standard Model. Pauli originally proposed only one type of neutrino, but other two types were detected, the muon (ν_μ) neutrino [3] and the tau (ν_τ) neutrino [4], respectively in the 1962 and 2000. Three flavors of neutrinos have been discovered corresponding to three flavors of charged leptons, matching them into couples.

Years later, neutrino physics was dramatically altered with the discovery of neutrino oscillation (Section 1.3), predicted by Bruno Pontecorvo, which opened the door to many new questions, including measurements of Charge Conjugation-Parity (CP) violation and possible sterile states of neutrinos. It all started in the 1960s, when the field of neutrino physics had an unresolved anomaly known as the Solar Neutrino Problem, and it lasted for 40 years. The model of the interactions in the Sun allows to predict the flux of the electron neutrino arriving on Earth [5]. Many neutrino experiments, measuring the neutrino flux from the Sun, observed a significant deficit compared to predictions [6]. Finally, in 2002, the Sudbury Neutrino Observatory (SNO) experiment published definite evidence of the solar neutrino oscillation [7], which supported observations of the atmospheric neutrinos from the Super-Kamiokande experiment [8] (Figure 1.1), and solar neutrino from GALLEX and SAGE [9]. The Solar Neutrino Problem found then its solution. The discovery that neutrinos can convert from one flavor to another and therefore have non-zero masses is a major milestone for elementary particle physics. It represents compelling experimental evidence for the incompleteness of the Standard Model as a descrip-

tion of nature. For this reason in 2015 the Nobel Prize in Physics was awarded to Takaaki Kajita of the Super-Kamiokande Collaboration and to Arthur B. McDonald of the SNO Collaboration for the clear evidence of the neutrino oscillation in two different scenarios.
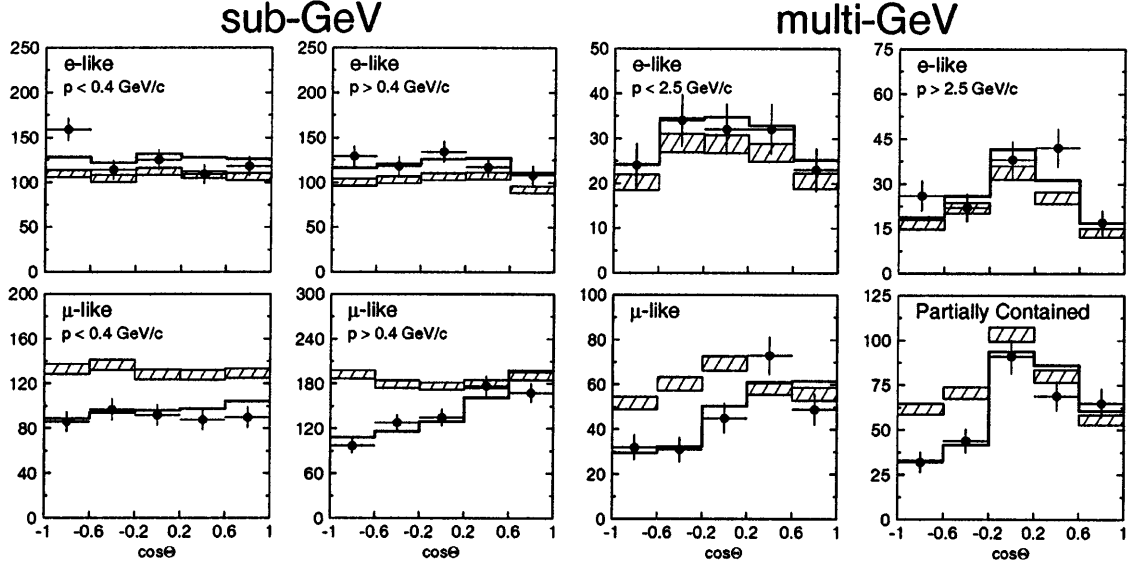
Figure 1.1: Distribution of zenith angle for muon-like and electron-like events for the sub-GeV (collected Cherenkov energy less than 1330 MeV) and multi-GeV (collected Cherenkov energy more than 1330 MeV) data sets from the Super-Kamiokande experiment, published in [8]. Upward-going particles have $\cos\theta < 0$ and downward-going particles have $\cos\theta > 0$. The hatched region shows the MC expectation for no oscillations normalized to data. The bold line is the best-fit expectation for $\nu_\mu \leftrightarrow \nu_\tau$ oscillations. The deficit of upward going muon neutrino above 1 GeV is the definitive evidence for atmospheric neutrino oscillation.

The exact mass of each type of neutrino is nowadays unknown, only upper limits are available ($m_{\nu_e} < 2.2eV/c^2$, $m_{\nu_\mu} \lesssim 170keV/c^2$, $m_{\nu_\tau} \lesssim 28MeV/c^2$), and future experiments have the goal to lower them [10], [11]. An important measurement, the number of active neutrino species, comes from the Large Electron-Positron collider (LEP) experiments at CERN (Switzerland). Since neutrinos can also interact via neutral-currents, where the outgoing lepton is not charged, the neutrinos can exchange a neutral Z^0 boson with the target material. One in five Z-bosons produced at LEP decayed into a "light neutrino", which is a neutrino whose mass is $m_\nu < m_{Z^0}$. The Standard Model relation between this decay width and the cross section for Z-boson production and subsequent decay into hadrons makes it possible to infer the number of light neutrino species. As a result the average, taking into account four different results from different experiments at LEP was measured to be 3.10 ± 0.04 [12], as seen in Figure 1.2.
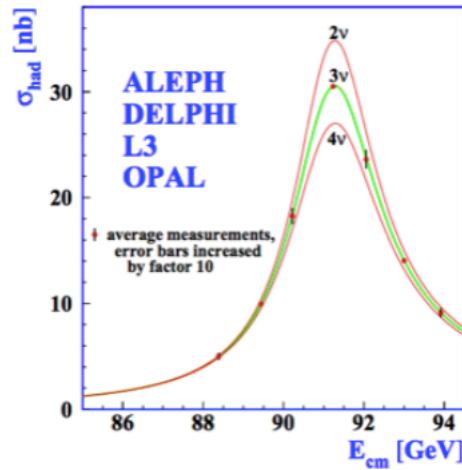
Figure 1.2: Measurement of the hadron production cross section as a function of the LEP centre-of-mass energy around the Z-boson resonance. Combined results from the four LEP experiments are shown. Curves represent the predictions for two, three and four neutrino species.

1.2   Neutrino Sources

Neutrinos are incredibly common on Earth, more than a trillion neutrinos pass through an average sized human hand every second. By far the most powerful nearby source of neutrinos is the Sun, which produces them in several different interactions, the most common of which is the proton-proton fusion. More powerful sources of neutrinos are known to exist, such as supernova [13]. On our planet neutrinos are produced in the geothermal reactions of the Earth core, but also in the upper part of the atmosphere where they are produced in the interactions of cosmic particles and in the following decays of the outgoing particles. There are also artificial sources of neutrinos, most commonly nuclear reactors. Neutrinos coming from reactors are less energetic than those coming from the Sun but the local neutrino flux can be quite high. Other artificial sources are neutrinos beams produced at accelerator complexes such as Fermilab (USA), CERN (Switzerland), and J-PARC (Japan). Artificial neutrino beams can provide a high intensity source of neutrinos over a large range of energies, and offer many other benefits as well. A detailed understanding of the source of neutrinos is vital to the success of every neutrino experiment, and Chapter 2 explores accelerator neutrino beams in more detail.

1.3 Neutrino Oscillation

Neutrino oscillation are the foundation and the starting point for modern neutrino experiments and can be used to probe the mass hierarchy of the neutrinos, other than being a very interesting and curious behavior. A description of the theory of neutrino oscillation and a summary of experimental evidences are presented hereafter.

1.3.1 Neutrino Oscillation: Theory

Neutrinos, when produced through electroweak interactions, are produced in flavor eigenstates. To date, there are known to be three flavors of neutrinos: ν_e, ν_μ, and ν_τ. Each of these neutrinos, as suggested by their name, corresponds to a charged lepton. The conservation of lepton flavor dictates that the number of leptons of a particular flavor is conserved during an interaction. As an example, the decay of a muon to an electron, an existing process in nature, would violate lepton flavor conservation if not for the presence of neutrinos:

$$\mu^- \to e^- + \overline{\nu}_e + \nu_\mu$$

Although the most striking evidence for the violation of lepton flavor conservation is the neutrino oscillation, there are hints that lepton flavor could be violated by charged leptons as well, an example is [14]. For neutrino oscillation, the violation of lepton flavor is a direct result of the fact that neutrinos in the lepton eigenstates are a superposition of the mass eigenstates:

$$\nu_e = \alpha \nu_1 + \beta \nu_2 + \gamma \nu_3$$

where the numerical neutrino states represent the neutrinos with a well defined mass. It should be noted, from a historical perspective, that in fact neutrinos were originally considered to be massless in the Standard Model. The discovery of neutrino oscillation instead provided definitive evidence that neutrinos have mass. The interesting phenomenon arises from the fact that neutrinos, produced in lepton flavor states, do not stay stably in those states. The most common way to mathematically describe neutrino oscillation is through the Pontecorvo-Maki-Nakagawa-Sakata matrix [15], [16], or PMNS matrix:

$$\begin{pmatrix} \nu_e \\ \nu_\mu \\ \nu_\tau \end{pmatrix} = \begin{pmatrix} U_{e1} & U_{e2} & U_{e3} \\ U_{\mu 1} & U_{\mu 2} & U_{\mu 3} \\ U_{\tau 1} & U_{\tau 2} & U_{\tau 3} \end{pmatrix} \begin{pmatrix} \nu_1 \\ \nu_2 \\ \nu_3 \end{pmatrix}$$

In this matrix, under the standard assumptions of neutrino oscillation, the rows and columns are normalize such that the matrix is unitary: $\sum_{j=1}^{3} |U_{\alpha j}|^2 = 1$. It is very common for the PMNS matrix to be parameterize in terms of mixing angles:

$$\begin{pmatrix} U_{e1} & U_{e2} & U_{e3} \\ U_{\mu 1} & U_{\mu 2} & U_{\mu 3} \\ U_{\tau 1} & U_{\tau 2} & U_{\tau 3} \end{pmatrix} = \begin{pmatrix} 1 & 0 & 0 \\ 0 & cos\theta_{23} & sin\theta_{23} \\ 0 & -sin\theta_{23} & cos\theta_{23} \end{pmatrix} \times$$

$$\begin{pmatrix} cos\theta_{13} & 0 & sin\theta_{13}e^{-i\delta_{CP}} \\ 0 & 1 & 0 \\ -sin\theta_{13}e^{i\delta_{CP}} & 0 & cos\theta_{13} \end{pmatrix} \times$$

$$\begin{pmatrix} cos\theta_{12} & sin\theta_{23} & 0 \\ -sin\theta_{23} & cos\theta_{12} & 0 \\ 0 & 0 & 1 \end{pmatrix}$$

The value of this expansion is such that the individual mixing angles are observable with different experimental setups. The additional phase, δ_{CP}, is needed if neutrinos violated CP symmetry and is non-zero only if neutrino oscillation violates CP symmetry; this has not yet been observed experimentally. Some theories, for example, suggest that neutrino violation of CP symmetry is responsible for the matter-antimatter asymmetry in the Universe. In general, an experiment probing neutrino oscillation would start with an ensemble of neutrinos prepared in a particular flavor state ν_α:

$$\nu_\alpha = U_{\alpha 1}\nu_1 + U_{\alpha 2}\nu_2 + U_{\alpha 3}\nu_3$$

The state of the neutrino ν_α evolves according to the standard time evolution operator, and so at a later time t, the neutrino state becomes

$$\nu_\alpha(t) = U_{\alpha 1}\nu_1(t) + U_{\alpha 2}\nu_2(t) + U_{\alpha 3}\nu_3(t)$$

where $\nu_j(t) = e^{-i(E_j t - \vec{p}\,\vec{x})}\nu_j(t=0)$ using the plane wave solution, with energy E_j, for the neutrinos. Since each neutrino has a different mass, the three components of a neutrino flavor state become out of phase as time passes. Since neutrino masses are known to be very small, and the neutrinos detected in experiments have typically energies of MeV or higher, all observed neutrinos are ultra-relativistic and the energy expression in the time evolution of the neutrino flavor state can be simplified with $E_j \approx E + \frac{m_j^2}{2E}$ and an eventual difference can be expressed as $E_j - E_k \approx \frac{m_j^2 - m_k^2}{2E}$. The probability for a neutrino, that started in the state α and is observed in the state β

at a later time t is:

$$P_{\alpha \to \beta} = |\langle \nu_\beta | \nu_\alpha \rangle|^2 = |\sum_j U_{j\alpha} U_{j\beta} e^{-i \frac{m_j^2}{2E} t}|^2$$

Neutrino oscillation searches observe the neutrinos at a distance far away from the source. Assuming the neutrinos travel at the speed of light, so that the distance L can be expressed as $L = ct$ (and typically setting $c = 1$), the useful oscillation probability expression for neutrino experiments is

$$P_{\alpha \to \beta} = |\sum_j U_{j\alpha} U_{j\beta} e^{-i m_j^2 \frac{L}{2E}}|^2$$

For the particular scenario of neutrino oscillation with only two types of neutrinos, the oscillation probability is often expressed as

$$P_{\alpha \to \beta} = 2(cos\theta sin\theta)^2 \left[1 - cos^2 \left(\frac{E_2 - E_1}{t} \right) \right]$$
$$= sin^2(2\theta) sin^2 \left(\frac{\Delta m_{21}^2 L}{4E} \right)$$

where θ is the mixing angle between the flavor eigenstates and the mass eigenstates, Δm_{21}^2 is the mass squared difference of the neutrino mass eigenstates, L is the traveled distance from the point where the neutrino was produced and E is the neutrino energy.

1.3.2 Neutrino Oscillation: Experimental Evidences

This section provides a brief overview of some of the notable oscillation experimental results to date. A much more complete summary of neutrino oscillation, both theory and experimental evidence, is available from the Particle Data Group [17].

Solar Neutrino Problem

The Standard Solar Model makes a definite prediction of the number of neutrinos produced by the Sun, while the observation of Ray Davis and John Bahcall at the Homestake experiment are approximately one third of the neutrinos they expected [18]. This observation was subsequently reproduced and confirmed by a number of following experiments [19], [20], [21], [22], [23], [24]. This phenomena was called the "Solar Neutrino Problem". The many neutrino detectors observing the solar neutrinos produced different measurements of their observed fluxes, compared to predictions from Standard Solar Models, Figure 1.3.
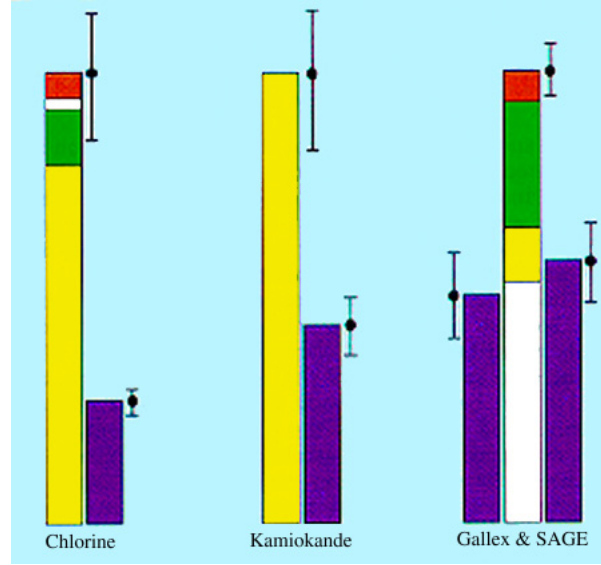
Figure 1.3: Solar neutrino flux measured (purple) by the four first-generation detectors show large deficits when compared with Standard Solar Model predictions. The different predicted total fluxes, normalized here to unity, comprise various individual solar processes, indicated by colors: white for pep fusion ($^1_1H + ^1_1 H + e^- \rightarrow ^2_1 D + \nu_e$); green for electron capture by ^{7}Be ($^7Be + e^- \rightarrow ^7 Li + \nu_e$); yellow for ^{8}B decay ($^8B \rightarrow ^8 Be^* + e^+ + \nu_e$); and red for the stellar carbon-nitrogen-oxygen cycle, which is calculated to play only a small role in the Sun. Figure from [25].

Each experiment, anyways, observed a different deficit of neutrinos. The reason for this difference lies in the fact that experiments searching for solar neutrinos had different detecting thresholds, and the solar neutrino flux is not constant over energy (Figure 1.4).

This strongly implied that the resolution of the Solar Neutrino Problem needed to account for a dependence on neutrino energy, consistent with neutrino oscillation. Furthermore, the neutrino oscillation in the Sun was affected by the interactions of neutrinos with matter, known as the Mikheev-Smirnov-Wolfenstien (MSW) effect [26]. Eventually, with the results of Super-Kamiokande and SNO experiments the squared mass separation, required to explain the solar neutrino deficit in terms of oscillations, was measured. This measurement was later confirmed by the KamLAND experiment which also was able to demonstrate experimentally the sinusoidal dependence of the neutrino oscillation [27], in Figure 1.5.

The KamLAND results [28] indicated that the solar neutrino mass splitting is $\Delta m^2_{solar} = 7.5^{+0.19}_{-0.20} \cdot 10^{-5} eV^2/c^4$, while the oscillation mixing angle is $tan^2(\theta_{solar}) = 0.452^{+0.035}_{-0.033}$.
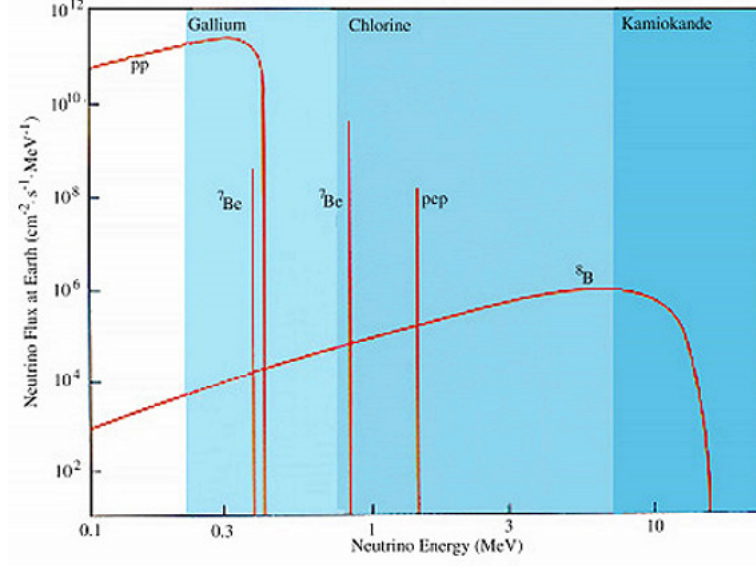
Figure 1.4: Predicted solar neutrino flux vs neutrino energy. The different flux regions observed by the first-generation detectors are shown. Light blue for Gallium, azure for Chlorine and blue for Kamiokande. Figure from [25].
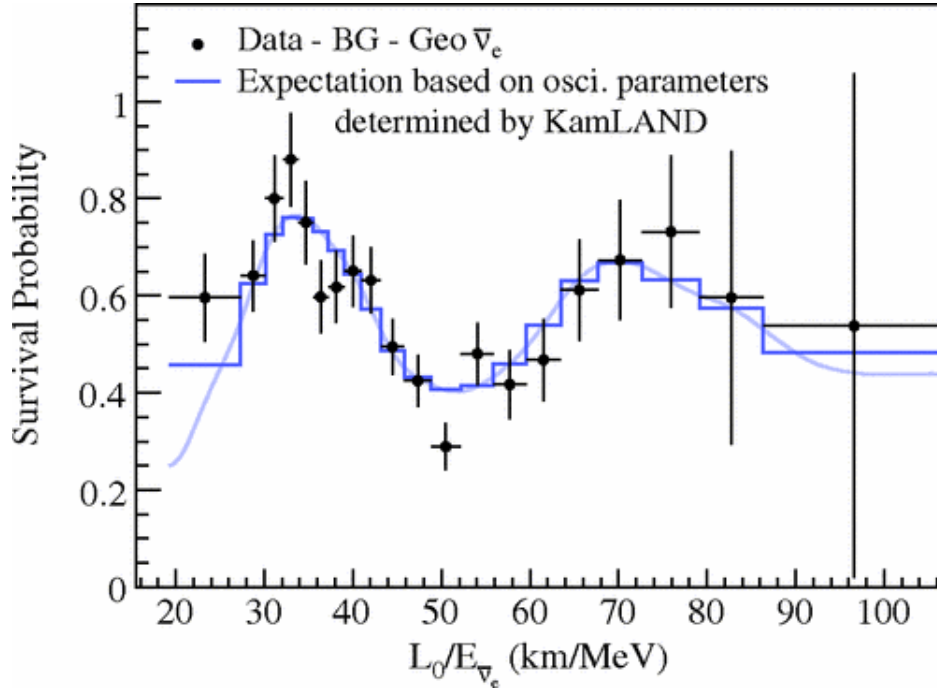
Figure 1.5: Ratio between the observed $\overline{\nu}_e$ number of events (after background and geo-neutrino subtraction) and the expectation for no oscillation vs L_0/E for the KamLAND experiment. The data points are plotted considering $L_0 = 180$ km. The sinusoidal dependence is visible and data agree well with the best fit oscillation hypothesis. Figure [27].

Atmospheric Neutrinos

Earth is continuously bombarded with particles in the upper atmosphere, producing, among other things, a flux of neutrinos primarily from the decay of pions and kaons [29]. The atmospheric flux is often predicted as a function of the zenith angle, and this allows neutrino oscillation experiments to study neutrinos over a very large range of distances: while the shortest distances of travel from production are dozens of kilometers, directly above the detector, neutrinos produced in the atmosphere and coming from the opposite side of the Earth must be considered too, $1.2 \cdot 10^4$ kilometers away from the detector. The atmospheric neutrino flux is composed primarily of ν_μ, $\overline{\nu}_\mu$, ν_e, and $\overline{\nu}_e$ neutrinos in approximately a 2:1 ratio for $(\nu_\mu + \overline{\nu}_\mu) : (\nu_e + \overline{\nu}_e)$ [17]. Compelling evidence for the oscillation of atmospheric muon neutrinos was presented by the Super-Kamiokande collaboration in 1998 [8], shown in Figure 1.1. Since the Super-Kamiokande detector, which is a Cherenkov detector, is unable to distinguish muons from antimuons, there is no ability of sign selection and the oscillation result is presented as a combined oscillation of muon neutrinos and antineutrinos. Because of the distances involved and the energy range of the neutrinos, the solar neutrino mixing is not plausible as an explanation for the oscillation of atmospheric neutrinos. In addition, the electron neutrino component of the flux is in general agreement with the observed data, assuming no oscillations. Therefore, the explanation is that atmospheric muon neutrinos oscillate predominantly into tau neutrinos. A subsequent study confirmed the statistical observation of tau neutrinos in atmospheric oscillations [30]. The atmospheric neutrino oscillation suggests a mass splitting that is in the range of $\Delta m_{atm}^2 \sim 10^{-3} eV^2/c^4$, significantly higher than the observed solar neutrino mass splitting.

On-Axis Neutrino Beams: K2K and MINOS

The precision measurement of the atmospheric neutrino mixing and mass splitting was determined using long-baseline neutrino oscillation experiments with neutrino beams. The first such experiment, KEK to Kamiokande (K2K), observed oscillations through the disappearance of accelerator-produced muon neutrinos [31](Figure 1.6 left). Main Injector Neutrino Oscillation Search (MINOS) was the second long-baseline neutrino oscillation experiment, with a beam of neutrinos from Fermilab traveling to Soudan in Minnesota. MINOS reported oscillation of muon neutrinos as well as muon antineutrinos due to the ability of the Neutrinos at the Main Injector (NuMI) beam to run in an antineutrino enhanced configuration [32]. MINOS is a magnetized detector, allowing sign selection of the muons it observes. The advantage of MINOS and K2K over the results of Super-Kamiokande is that the source of

neutrinos is controlled, the energy spectrum is relatively narrow banded and the length for oscillations is fixed (250 km for K2K, 735 km for MINOS). Because the parameters of the experiments are more tightly controlled, MINOS and K2K are both able to measure the parameters of atmospheric oscillation with a relatively high precision. MINOS full data set measures the atmospheric oscillation parameters as $\Delta m^2_{atm} = 2.41^{+0.09}_{-0.10} eV^2/c^4$, with $sin^2(2\theta_{atm}) = 0.950^{+0.035}_{-0.036}$ [33].
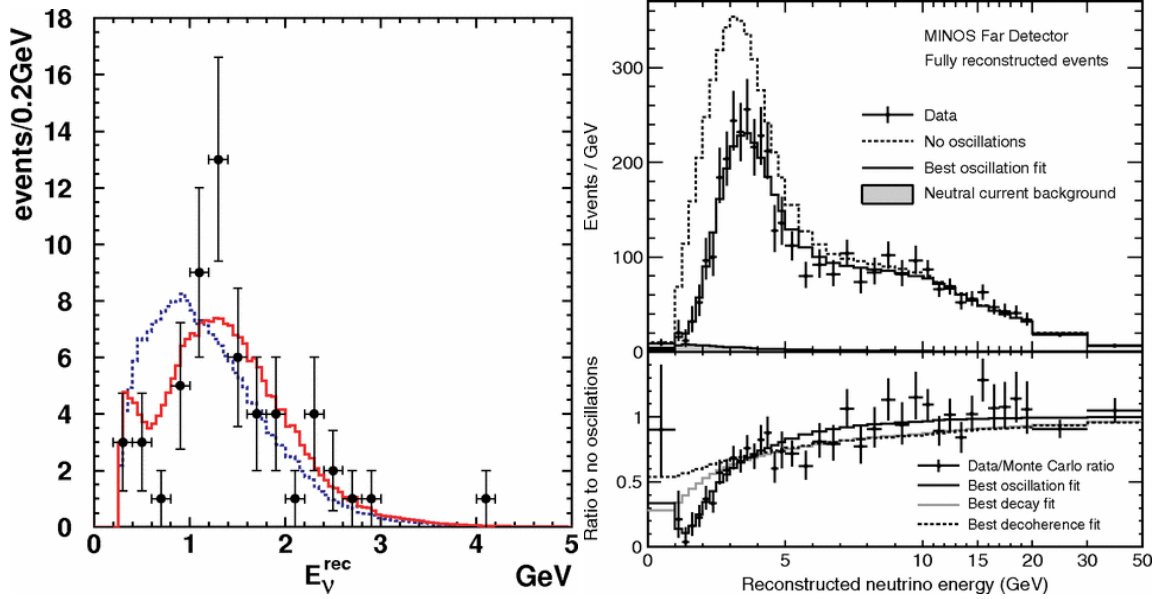
Figure 1.6: (Left) The reconstructed E_ν distribution for muon-like events for the K2K experiment. Data are represented by pints with error bars. The solid line (red) is the best fit spectrum with neutrino oscillation and the dashed line (blue) is the expectation without oscillation. Histograms are normalized by the number of events observed, 58. (Right Top): The energy spectra of fully reconstructed events in the MINOS Far Detector classified as charged-current interactions. The dashed histogram represents the spectrum assuming no oscillations, while the solid histogram reflects the best fit of the oscillation hypothesis. (Right Bottom): The ratio between the number of data events (background-subtracted) and the expectation for no oscillation hypothesis vs the reconstructed neutrino energy for the MINOS experiment. Lines show the best fits for: oscillations, neutrino decay and neutrino decoherence.

Off-Axis Neutrino Beam: T2K, NOνA

As one moves off of the axis of a neutrino beam, the flux from the beam decreases and narrows in energy. For an oscillation experiment, a mono-energetic and point-like neutrino source is ideal, and an off-axis neutrino beam is closer to this ideal situation. Both the T2K and NOνA experiments use this to study neutrino oscillation. In particular, since NOνA is a fine grained detector, they are able to observe the

appearance of electron neutrinos coming from the $\nu_\mu \to \nu_e$ oscillations. More details can be found in [34] and [35].

Reactor Neutrino

Nuclear reactors provide a high intensity flux of electron antineutrinos in the $\sim$ MeV range, so an experiment at around 1 km can probe $\overline{\nu}_e$ disappearance due to mass splittings in the range of $10^{-3}eV^2/c^4$. The first experiment to actively search for $\overline{\nu}_e$ disappearance due to a non-zero θ_{13} mixing angle was CHOOZ in France. CHOOZ found no evidence for non-zero θ_{13}, but set an upper limit on the mixing angle and proposed a follow up experiment to improve sensitivity to lower this limit [36]. Double-CHOOZ [37], Daya Bay [38], and Reno [39] all reported significant observation of $\overline{\nu}_e$ disappearance from reactor neutrinos. The latest results from Daya Bay [40] are reported in Figure 1.7.
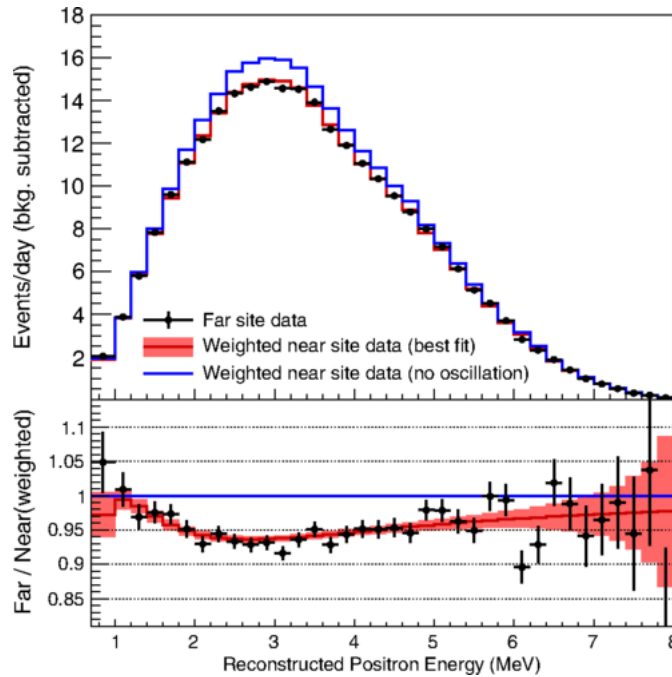
Figure 1.7: (Left Top): Background-subtracted reconstructed positron energy spectrum observed in the far site for the Daya Bay experiment (black points). Expectation excluding (blue line) or including (red line) the oscillation hypothesis are shown too. The spectra were efficiency-corrected and normalized to one day of measurement. (Left Bottom): Ratio between the spectra shown in the plot above and the no-oscillation case. The shaded area includes the systematic and statistical uncertainties from the near site measurements.

1.4 Neutrino Interaction Measurements

Today studies of the properties of neutrino (mass and mixing) have a primary role, but still a lot about neutrino interactions needs to be understood in view of future experiments aiming at understanding neutrino properties. Neutrino cross section depends on the type of interaction (neutral-current or charged-current), the neutrino energy range (MeV, GeV or TeV) and the neutrino target (electron, nucleus, nucleon, quark). Precise neutrino nucleus cross section measurements are interesting measurements per se, but also a fundamental prerequisite for every neutrino oscillation experiment. As a result, interest in neutrino scattering measurements has recently increased. A correct interpretation of the outcome of neutrino oscillation experiments requires precise understanding of neutrino and antineutrino cross section in a rather challenging regime (GeV energy range). In this energy range several distinct neutrino scattering mechanisms start to play a role and the description of neutrino scattering becomes increasingly more complicated, see Figure 1.8. The three main categories are: quasi-elastic scattering (QE), resonant production (RES) and deep inelastic scattering (DIS). In a small energy range different interactions can occur and the dominant interaction channels change rapidly.
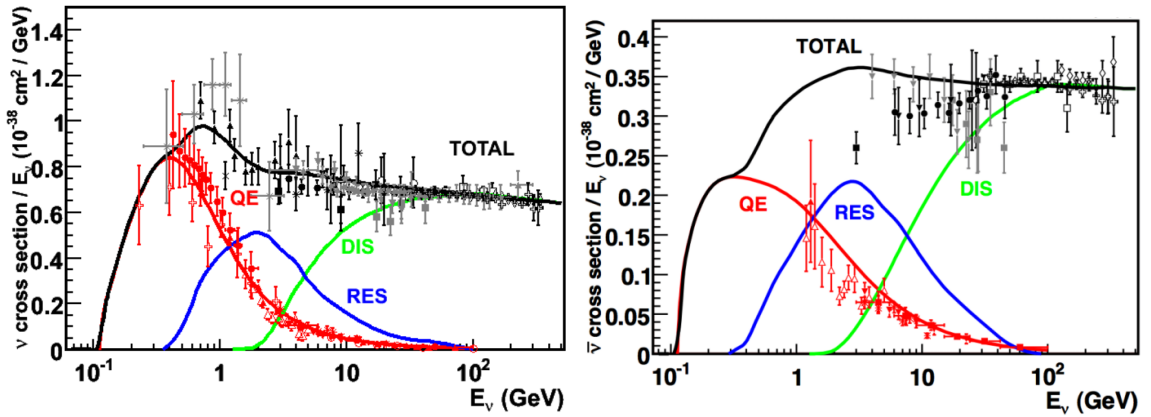
Figure 1.8: Muon neutrino (left) and muon antineutrino (right) charged-current cross section measurements as a function of neutrino energy. The contributing processes in this energy region include quasi-elastic (QE) scattering, resonance production (RES), and deep inelastic scattering (DIS). A reference of these cross sections measurements can be found in [41].

Neutrino scattering at intermediate energies is generally complicated and is not yet well measured. Neutrino and antineutrino charged-current cross section measurements, in the neutrino energy range of the few GeV, are shown in Figure 1.8. Data have large uncertainties (20-40%) or show discrepancies between different data set and MC predictions. Flux normalization, due to poor knowledge of hadron pro-

duction, has large uncertainties and is usually the dominant uncertainty in neutrino cross section measurements (approximately 15-20%). Most of our knowledge of neutrino cross sections in this energy range comes from experiments conducted in the 1970's and 1980's using either bubble chamber or spark chamber detectors, that collected relatively small data samples (tens to a few thousand events). With the discovery of neutrino oscillation and the advent of higher intensity neutrino beams this situation has been rapidly changing and more and more experiments have started to collect neutrino scattering data in this energy range (ArgoNeuT, K2K, MiniBooNE, MINERνA, MINOS, NOMAD, SciBooNE, and T2K). Modern day neutrino experiments use complex nuclei as neutrino target. With this choice nuclear effects arise and must be well understood. These nuclear effects can range from the emission of single or multiple nucleons to more complex topology with multiple pions or other hadrons, all in addition to the leading lepton. Some hadrons can't make their way out of the nucleus and end up absorbed by it. As a result, final state particle topology and kinematics are significantly altered in neutrino cross section measurements (in the energy range from hundreds of MeV to a few GeV). Due to intra-nuclear re-scattering (final state interaction (FSI), processes like pion absorption, charge exchange, etc) and effects of correlation between target nucleons, even a genuine QE interaction can often be accompanied by the ejection of additional nucleons, emission of many de-excitation gamma's and sometimes by soft pions in the final state. Nuclear effects depend on the number and type of nucleons in the nucleus and therefore are different for different types of nuclei. Modeling neutrino interactions becomes very complicated. Improved experimental measurements and theoretical calculations in the intermediate energy region will be especially important for reducing systematic uncertainties in future precision neutrino oscillation experiments.

1.5   Future Directions in Neutrino Physics

Despite oscillations, many properties of neutrinos remain unknown. Forthcoming neutrino experiments will focus on:

1. the direct measurements of neutrino mass by precision measurements of tritium decay;

2. whether or not neutrinos are their own antiparticle by searching for neutrino-less double-β decay;

3. the mass hierarchy of neutrinos;

4. the search for CP violation in the neutrino sector;

5. the number of existing neutrino species besides the already known ones, if any, and eventually sterile neutrinos.

Items 1 and 2 are studied in β and double-β decay experiments, while 3 and 4 are performed in long-baseline neutrino oscillation experiments. Motivations for the ongoing and forthcoming searches for sterile neutrinos, item 5, are described below.

1.5.1 Short-Baseline Neutrino Anomalies

Over the past two decades, there have been a number of anomalous results from short-baseline experiments from a variety of neutrino experiments. Individually, each experiment lacks the significance to be convincing and claim discovery beyond the Standard Model physics. Taken together, however, these data can be interpreted as an oscillation on a mass splitting scale that is inconsistent with the three neutrino mixing model. A complete analysis of the global, experimental picture of neutrino oscillation is given by oscillation analysis such as [42] and [43]. There is indication that anomalous neutrino oscillation could be occurring at short-baselines.

LSND and MiniBooNE Experiments Anomalies

In 1995, the Liquid Scintillator Neutrino Detector (LSND) at Los Alamos National Laboratory published the results of its first search for $\overline{\nu}_\mu$ to $\overline{\nu}_e$ oscillations [44]. It used a liquid scintillator detector making observations of electron antineutrinos through the inverse β-decay reaction on carbon. The neutrinos came from a decay-at-rest pion source, in the range from 20 to 50 MeV. In the inverse β-decay reaction, signature is a prompt positron emission, followed by a 2.2 MeV gamma from neutron capture. LSND observed $89.7 \pm 22.4 \pm 6.0$ $\overline{\nu}_e$ candidate events above background over five years of data taking, corresponding to a significance of 3.8σ. Most recently, the MiniBooNE collaboration published evidence of an excess of electron neutrino candidate events in both neutrino and anineutrino mode at the Fermlab Booster Neutrino Beam (BNB) [45]. The significance of the results, in Figure 1.9, is 3.4σ for neutrino mode and 2.8σ for antineutrino mode.

Since electrons and photons both produce similar electromagnetic cascades, MiniBooNE, a Cherenkov type detector, is unable to distinguish with high efficiency between low energy electron and single photon events. This implies that the excess can't be successfully explained without further investigation.
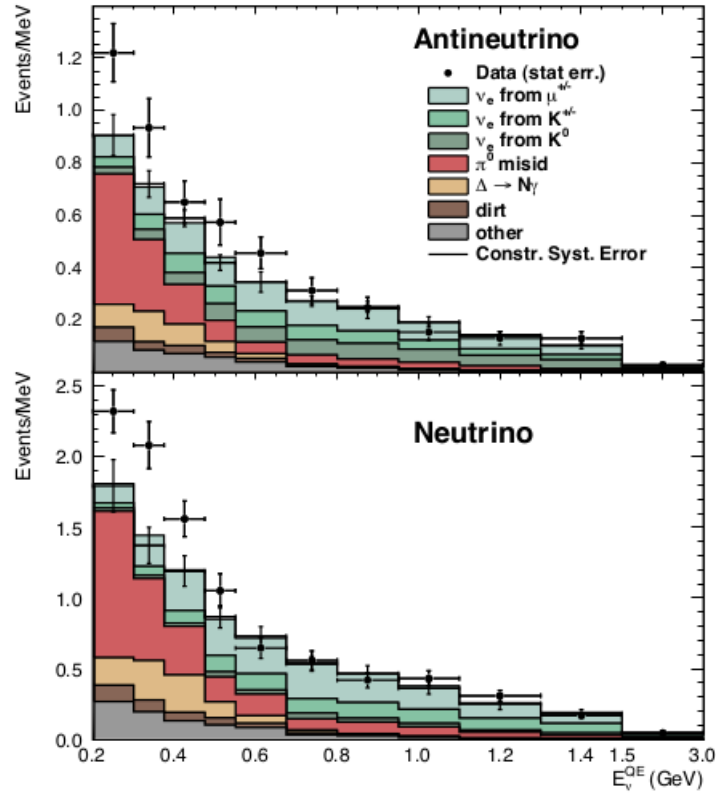
Figure 1.9: Electron neutrno energy distributions for charged-current events in antineutrino mode (top) and neutrino mode (bottom) beam configurations. The observed electron neutrino candidate events are more than the expected. This excess could imply a discrepancy in the muon neutrino oscillation process that will be investigated by future experiments.

Reactor and Solar Experiments Anomalies

The GALLEX and SAGE solar neutrino detectors have been tested in the so-called "Gallium radioactive source experiments" which consist in the detection of electron neutrinos produced by intense artificial ^{51}Cr and ^{37}Ar radioactive sources placed inside the detectors [46]. These radioactive nuclei decay through electron capture, emitting ν_e at energies below 1 MeV. The neutrinos emitted by the radioactive sources have been detected through the same reaction used for the detection of solar neutrinos $\nu_e + ^{71}Ga \rightarrow e^- + ^{71}Ge$. In total four source experiments have been performed. The average ratios, measured over predicted ^{71}Ge production rates in the GALLEX and SAGE source experiments, is R $= 0.86 \pm 0.05 \pm 0.10$. Thus, the number of measured events is about 2.7σ smaller than the prediction. This is the "Gallium anomaly", which could be also a manifestation of short-baseline electron neutrino disappearance.

A recent evaluation of the expected reactor antineutrino spectra have been provided for ^{235}U, ^{239}Pu, ^{241}Pu, and ^{238}U increasing the mean flux by about 3% [47]. To a good approximation, this re-evaluation can be applied to all reactor neutrino experiments. Combining the results of experiments presenting a reactor-detector distance less than 100 m, the ratio between observed event rate and predicted event rate is observed to be 0.976±0.024. Considering the recent flux evaluation, this ratio shifts to 0.943±0.023. This takes the name of reactor antineutrino anomaly and it is supported by the experimental results from the Daya Bay collaboration [48] (See Figure 1.10).

This anomaly is consistent with an oscillation of reactor $\bar{\nu}_e$ into an unobserved sterile state, which may hint to a 3+N neutrino model explanation (3 standard neutrinos + N "sterile" neutrino states). Several, running or in preparation, experiments have the goal of searching for sterile neutrinos.
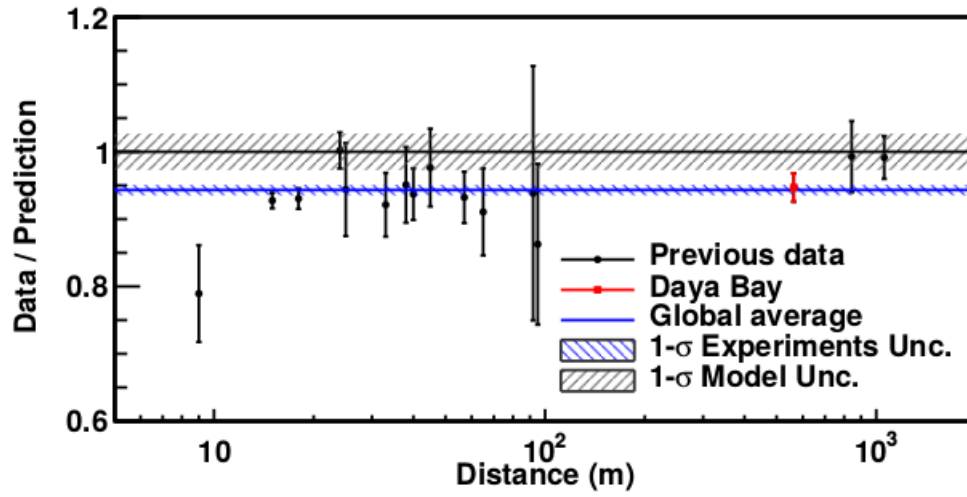
Figure 1.10: Measured reactor $\overline{\nu}_e$ rates, normalized to the theoretical predictions, as a function of the reactor-detector distance. The theoretical predictions consider a 3-flavor neutrino oscillation process. The blue shaded region represents the global normalized rate average and its 1σ uncertainty, while the black shaded region represents the 2.7% model uncertainty. The Daya Bay measurement is shown at the baseline of 573 m (red).

Chapter 2

Neutrino Beams

This Chapter describes the Fermilab accelerator based neutrino beams. The Booster Neutrino Beam (BNB) is described in Section 2.3, which is relevant to the Fermilab Short Baseline Neutrino (SBN) Program, and the Neutrinos from Main Injector (NuMI) beam, which is relevant for the ArgoNeuT and MINOS experiments, is described in Section 2.4.

2.1 Accelerator Based Neutrino

Neutrino beams are very popular in modern experiments because of the advantages they can offer. First, neutrino beams made at accelerator complexes are properly designed, this means that the beam is often optimized for a specific physics goal, in particular by tuning the energy spectrum and energy range of the neutrino beams. As an example, the NuMI beam, described in Section 2.4, was designed to run in three different modes in order to cover an entire neutrino energy range from 1 to 20 GeV. Another advantage to neutrino beams at accelerators is the pulse structure of the beam. Neutrino beams are made by colliding bunches of protons with a solid target material, this means that the timing of the proton bunches defines the time structure of the neutrino beams.

2.2 Fermilab Accelerator Complex

At Fermilab, until August 2012, a Cockroft-Walton generator was the starting point of the accelerator complex. Now a radio-frequency quadrupole, or RFQ, is the birthplace of particle beams for the laboratory's many experiments. It provides the particle beam source for the entire accelerator complex and takes low-energy proton beam from an ion source, accelerates and "bunches" it into separate packets

of particles, and injects it into Fermilab's linear accelerator, or Linac. The RFQ accelerates the beam from 35 keV to 750 keV. The protons are accelerated up to 400 MeV in the Linac and at the end of it enter the Booster, a synchrotron. Over the course of thousands of rotations around the Booster, the protons are accelerated up to 8 MeV of kinetic energy. The Booster can nominally operate at 15 Hz. From the Booster, protons can be extracted to the Boster Neutrino Beam (BNB) target. The majority of protons, however, enter the Main Injector to be accelerated to higher energies, up to 120 GeV. A schematic view of the Fermilab accelerator complex can be seen in Figure 2.1
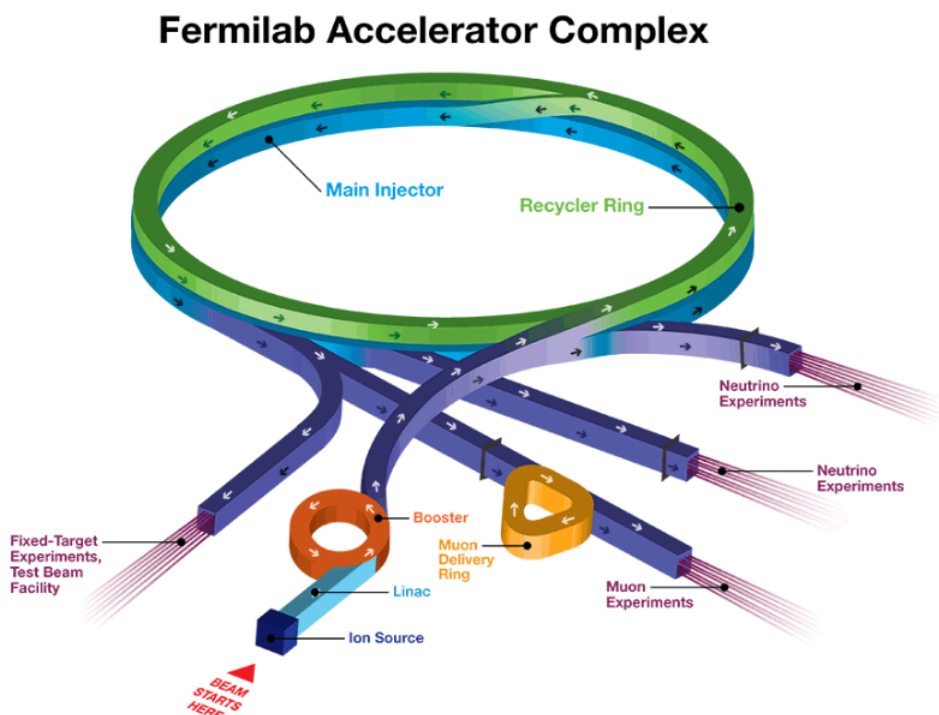
Figure 2.1: Schematic view of the Fermilab accelerator complex with the three main components: (light blue) Linac, (orange) Booster and (green) Main Injector.

2.3   Booster Neutrino Beam (BNB)

The BNB is the Fermilab lower energy neutrino beam, it was the primary beam for MiniBooNE experiment, it is now for MicroBooNE experiment, and it will be for the entire Short Baseline Neutrino (SBN) Program. The BNB has been running since the MiniBooNE experiment, in 2002.

2.3.1 BNB Design

The BNB was designed for, and by, the MiniBooNE collaboration. MiniBooNE was a Cherenkov detector, searching for electron neutrino appearance. Since the primary background for MiniBooNE consisted in photons from neutral pion productions in the detector, the BNB flux was designed to run low energy neutrinos, the flux peak is at an energy lower than ∼1 GeV. 8 GeV protons, 8.89 GeV/c momentum, from the Fermilab Booster complex are transported to a Beryllium target, encased in a magnetic focusing horn. The protons collide with the Beryllium and produce hadrons, which are focused into the forward direction by the focusing horn. The hadrons enter a decay pipe of 50 meters, where they decay in flight into lighter particles including neutrinos. At the end of the decay pipe there is a beam stop in order to allow only neutrinos to proceed further. A graphical representation of the magnetic focusing horn can be seen in Figure 2.2.
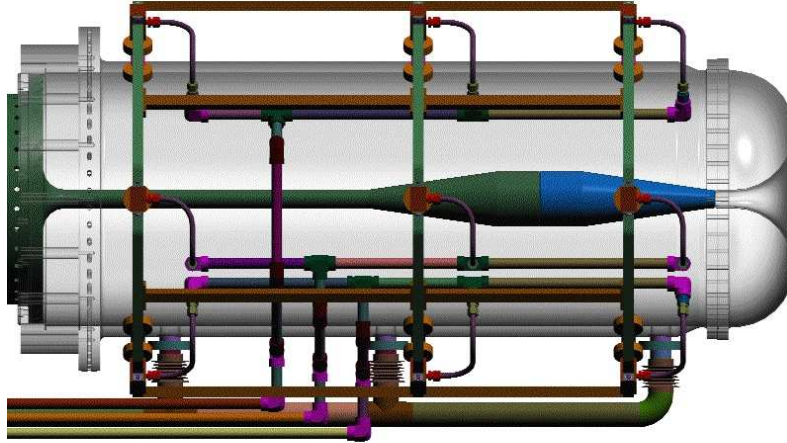
Figure 2.2: The Booster Neutrino Beam horn and focusing magnet in the center. Figure from [49].

A schematic of the proton entry, horn location, decay pipe and beam stop are shown in Figure 2.3.

The batches of protons delivered to the Booster target are pulsed, typically at a rate not higher than 5 Hz, and each bunch is approximately 1.6 μs in duration. Each bunch of protons from the Booster typically contains approximately $4{\cdot}10^{12}$ protons. These protons collide with the Beryllium target, which is 70 cm long and divided in seven segments. This length is enough to make over 80% of the protons interact in the target material. The number of protons on target is measured upstream
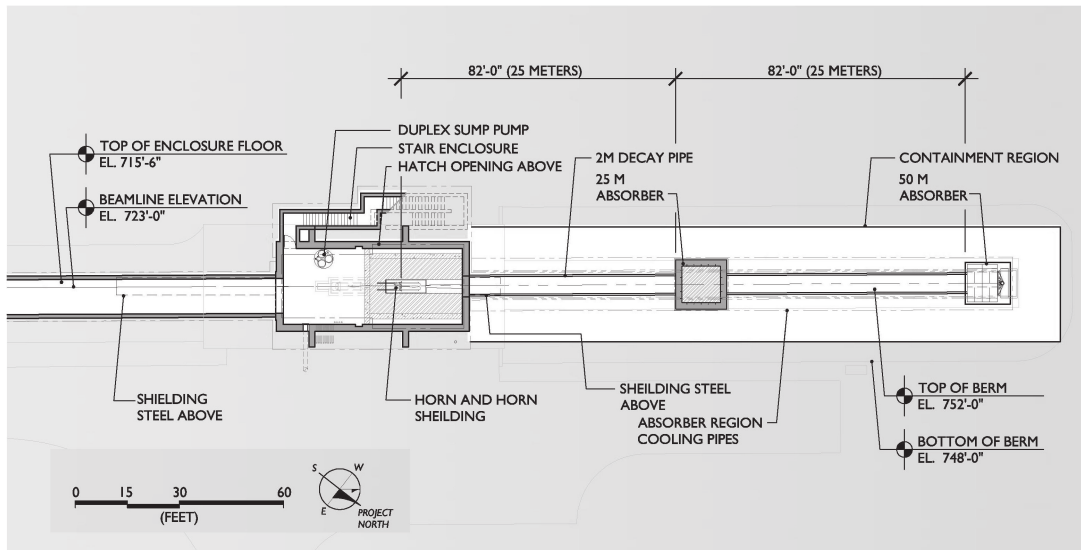
Figure 2.3: The Booster Beam target hall and decay pipe. Protons enter from the left, and hadrons decay in the decay pipe for up to 50 m before the beam absorber. Figure from [49].

of the target by two magnetic toroids, and the uncertainty on the number of protons delivered is on the order of 1-3% typically. Upon interacting, protons produce lighter hadrons such as pions and kaons. The spectra of produced hadrons is the source of the largest uncertainty in the BNB. The hadrons produced by the protons at the target are focused with the magnetic horn which produces an azimuthal, pulsed magnetic field in time with the proton delivery. The primary source of the neutrinos in the BNB is from decays of in flight pions, though there is a significant contamination from kaon decay and muon decay, where muons come also from the pion decay. Kaons and muons also produce a contamination of electron neutrinos in the primarily muon neutrino beam. The estimation of the flux, by neutrino type and by originating particle, at the MiniBooNE location can be seen in Figure 2.4. This estimate of the flux is produced with a sophisticated Monte Carlo simulation, discussed in detail in [49].

Table 2.1 is included here to showcase the precision at which MiniBooNE constrained the BNB, an accomplishment that future experiments are building upon.

2.4   Neutrinos from the Main Injector (NuMI)

The NuMI beam was projected with the MINOS experiment. The NuMI beam was designed to be configurable and to run in multiple modes: Low Energy, Medium Energy, and High Energy. The various energy spectra are shown in Figure 2.5.

This section will be a very brief summary of some important facts about the
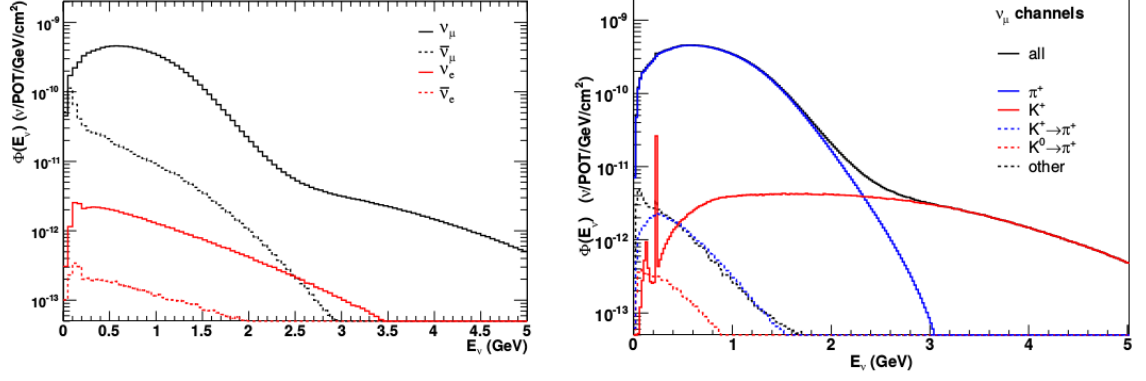
Figure 2.4: (Left) Total predicted flux at the MiniBooNE detector by neutrino species with BNB horn focusing in neutrino mode. (Right) Muon neutrino flux by parent meson species with horn in neutrino mode. Figure from [49].

Table 2.1: Fractional flux uncertainties, by species of neutrino, from the MiniBooNE flux calculation.

Source Of Uncertainty	ν_μ	$\bar{\nu}_\mu$	ν_e	$\bar{\nu}_e$
Proton Delivery	2.0%	2.0%	2.0%	2.0%
Proton Optics	1.0%	1.0%	1.0%	1.0%
π^+ Production	14.7%	1.0%	9.3%	0.9%
π^- Production	0.0%	16.5%	0.0%	3.5%
K^+ Production	0.9%	0.2%	11.5%	0.3%
K^- Production	0.0%	0.2%	2.1%	17.6%
Horn Field	2.2%	3.3%	0.6%	0.8%
Nucleon Cross Sections	2.8%	5.7%	3.3%	5.6%
Pion Cross Sections	1.2%	1.2%	0.8%	0.7%
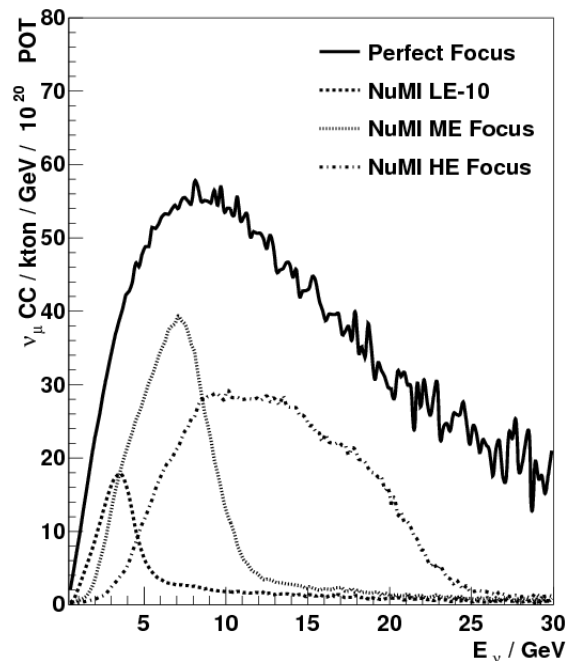
Figure 2.5: The various energy tuning configurations for NuMI. The analysis performed for this work is based on the Low-Energy mode, in antineutrino mode.

NuMI beam. The NuMI target is very similar to the BNB target, though it is more complex for the following reasons:

- The distance between the target itself and the focusing horns is adjustable to allow the different running configurations.

- There are two focusing horns instead of just one. The first horn, located close to the target, and the second horn, downstream, effectively act as a charged hadron focusing system. With a higher energy source of protons compared to the BNB, the two horns are necessary to focus the higher energy secondary particles from the target.

- Downstream of the target and horn area is the NuMI decay pipe, which is 675 m in length. After the decay pipe there is 240 m of rock, followed by the near detector for the MINOS experiment.

The schematic of the target, horn, and decay pipe are shown in Figures 2.6.

The NuMI flux is simulated with a FLUKA simulation in a very similar way that has been used for the BNB. It also benefits from the constraints from dedicated hadron production experiments [50], [51], and in measurements from the detectors
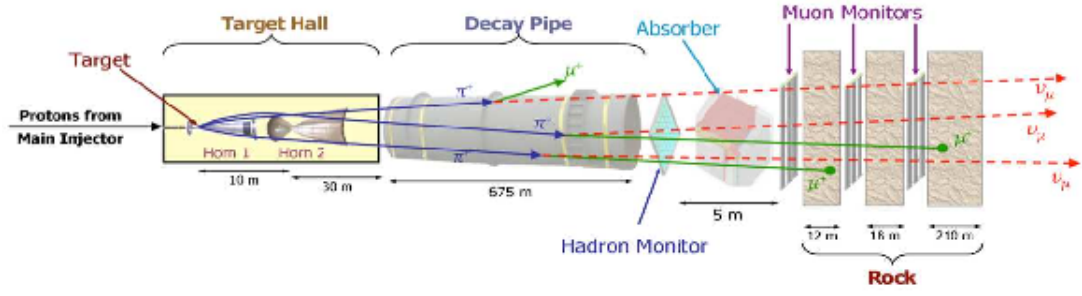
Figure 2.6: Sketch of the beam target, horns, and decay pipe responsible for the production of the NuMI beam.

along the beam line [52]. The flux models in the simulation of the beam are generally accurate to 10 or 20%, however experimental constraints and flux tuning can decrease the uncertainty to less than 10% [52]. ArgoNeuT, the detector that collected the data of this thesis, was placed in the MINOS near detector hall between MINOS and the Minerνa experiments. The neutrino flux shown in Figure 2.7 is the computed ArgoNeuT flux without the addition of the constraints, in the NuMI Low Energy mode.
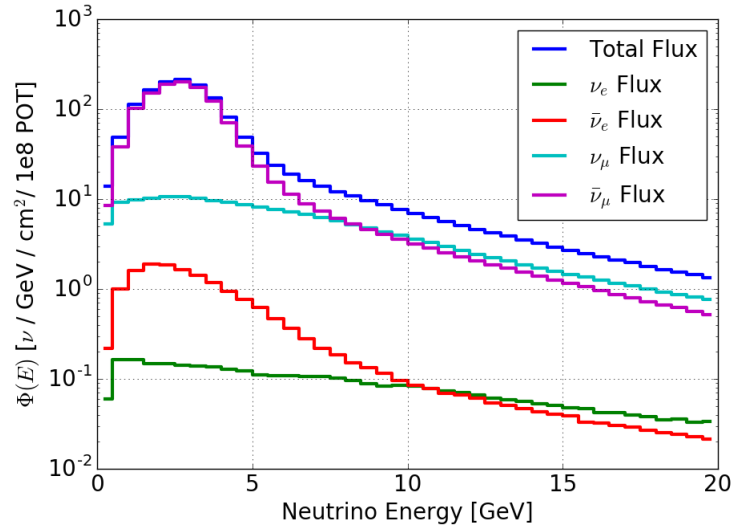
Figure 2.7: The predicted flux of the NuMI beam in Low Energy mode at the ArgoNeuT position. All neutrino species present in the flux are shown.

Chapter 3

ArgoNeuT and Future LArTPCs

In the first part of this Chapter general information about Time Projection Chamber (TPC) detectors and Liquid Argon Time Projection Chamber (LArTPC) detectors, their general functioning and the reasons behind the choice to use this particular detectors are described. The second part of this Chapter focuses more on the Argon Neutrino Test (ArgoNeuT) detector as a prototype of future LArTPCs and on how it produces an image of a neutrino argon interaction. Finally, future LArTPC detectors are described in the last Section.

3.1 Time Projection Chamber (TPC)

The Time Projection Chamber (TPC), is a revolutionary particle detector concept first proposed in 1974 by David Nygren at Lawrence Berkeley National Lab. Since its creation, the TPC has found applications in a broad array of particle physics experiments, such as collider experiments at the LHC [53], precision measurements of muon properties [54], dark matter experiments [55] and more. Very key propriety for the TPC technology are the versatile and robust ability to track charged particles. In general, a TPC is a volume filled with some inert material and an electric field applied to the medium. In some cases a magnetic field is applied too. The electric field is generally applied by using a high voltage cathode as one surface of the detector. The opposing surface, the anode, is typically instrumented with read-out equipment. TPCs are designed to observe electrically charged particles, in particular, a high energy charged particle, such as an electron, a muon, etc., travel through the detector and ionize the substance in it as it passes, leaving a trail of electrons and ions. The applied electric field, emanating from the cathode, serves to separate the charged particles produced in the ionization and move the electrons towards the anode of the detector. Drifted electrons form the basis of the measure-

ment. They appear as a projection of the original track on the anode of the detector, and the distance from the anode is determined by the time it take to the electrons to drift. This is the reason why they are called Time Projection Chamber.

3.2 LArTPC Concept

The LArTPC was invented in 1974 by Bill Willis and Veljko Radika [56], and initially proposed for neutrino physics in 1977 by Carlo Rubbia [57]. At the time of its conception, neutrino physics was dominated by bubble chamber detectors like Gargamelle [58], renowned for its remarkable resolution of particle topology. Initially, the LArTPC was proposed as a way to combine high spatial resolution detectors with calorimetry measuring detectors in one unique apparatus. The original advantages of the LArTPC technology were pointed out in 1977 and this list has the intent to summarize them:

- "It is dense": The relatively high density of liquid argon, at $1.4\,\mathrm{g/cm^3}$, provides a sufficiently high neutrino interaction rate such that high statistics measurements are possible and practical to achieve.

- "It does not attach electrons and permits long drift times": Since a long drift time is essential to large scale detectors to both maximize the mass of the detector and minimize the number of read-out channels, the fact that argon itself does not attach free electrons is an essential ingredient to LArTPCs.

- "It has a high electron mobility": The high mobility makes drifting electrons from particle ionization in a short time a feasible task.

- "It is cheap": A detector can not be scaled to massive sizes unless the fundamental building blocks of it are affordable.

- "It is easy to obtain and purify": Purification challenges have largely been overcome for LArTPCs. In particular, the MicroBooNE experiment has demonstrated a viable way to achieve high purity argon without purging the detector of impurities first.

- "It is inert and can be liquified with liquid nitrogen": This makes the cryogenic systems for LArTPCs reasonable to purchase and implement. 40 years after the original proposal, it is remarkable how relevant the initial advantages remain.

Since the original proposal, some additional advantages of LArTPCs have been noted and are worth mentioning. For example, the scintillation of liquid argon has been successfully characterized [59] and is measurable in coincidence with the drift ionization. For large detectors, especially surface detectors, this allows the ability to match scintillation light to ionization tracks in order to reject events such as cosmic particles. It also allows the implementation of a hardware-based trigger to filter neutrino interactions online. For even modest sized LArTPCs, this can be an essential aspect to control data rates and ease computing requirements.

3.3 General Functioning of LArTPCs

As a neutrino interacts in a LArTPC, it produces particles traveling away from the vertex of the interaction: muons, protons, neutrons, pions (charged and neutral), photons, electrons and so on. Electrically charged particles ionize the argon atoms as they moves through the detector. Ionization is a statistical quantity, but the average expected ionization depends strongly on the momentum and mass of the particle in question [60]. The ionization per unit distance, measured most frequently in the units MeV/cm, is a very powerful tool for calorimetric identification of particles (Section 3.5.5), and will be used in the analysis of this thesis. Neutral particles, instead, such as neutrons and photons, do not ionize the argon atoms as they pass through the detector. However, these particles can still interact with the argon and produce charged particles which are tracked by the TPC instrumentation. Neutrons frequently scatter off of an argon nucleus and produce a recoiling proton, which can be observed in the detector. Photons can produce electromagnetic showers through Compton scattering and pair production. After the particles from the neutrino interaction have produced ionization in the detector, the electric field separates the ions and electrons from each other and makes them drift respectively toward the cathode and the anode. This separation is not perfect due to the recombination of electrons and ions, which depends mostly on the strength of the electric field and the amount of ionization produced. This phenomenon has been studied in detail in the ArgoNeuT detector [61]. In general, this effect causes a quenching of the observed electrons compared to the true ionizing power. The ionization electron tracks are projected onto the anode along the electric field lines. The read-out of the electron track image is obtained by configuring the anode as a system of parallel wire-planes, more than or at least two, biased at specific potentials to enhance "transparency" of the successive wire plane to drifting electrons. With this configuration, each segment of a track induces a pulse signal, called "hit", on one wire in each plane (in normal

cases). The coordinate of the wire in the plane provides the hit position, so that multiple and independent localization of the track segment can be accomplished.

Timing of the pulse information, combined with the drift velocity information, determines the drift-coordinate of the hit, thus providing full three dimensional (3D) image reconstruction capability. In liquid argon, no charge multiplication occurs. The signal pulse height is therefore proportional to the amount of ionization charge in the track segment. A precise measurement of the deposited energy along the track can thus be extracted for an effective particle identification. By summing the charge over the entire track length in liquid argon, calorimetry information can be obtained for each reconstructed particle. Figure 3.1 shows with a sketch how an event occurring in a LArTPC is reconstructed in a 3D image.
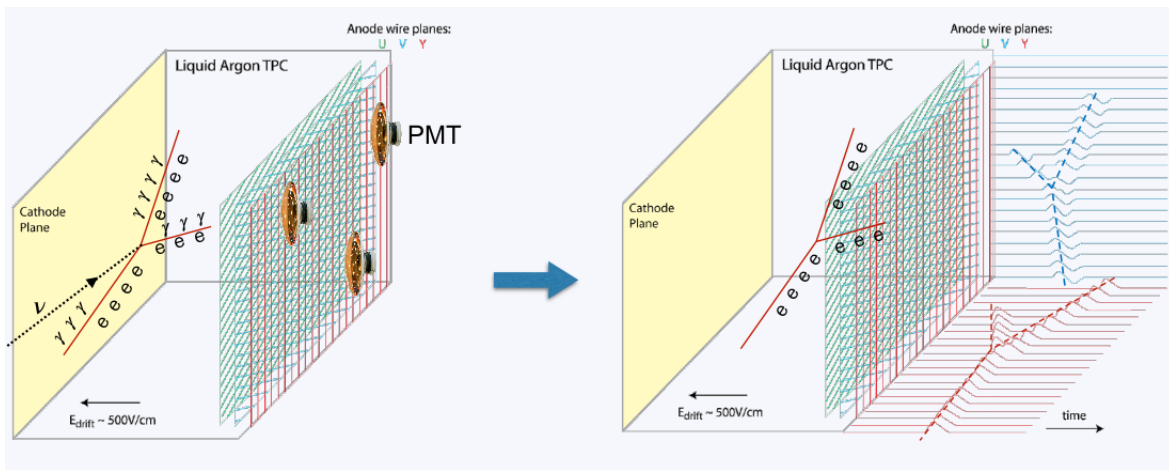
Figure 3.1: On the left: Sketch of a neutrino event in the LArTPC, showing the positions of the cathode, the anode, the paddles and the direction of the electric field. On the right: The charged particles produce hits on the wired planes, creating a couple of 2D view of the event. Combining the 2D views with the drift coordinate the event can be reconstructed in a 3D image.

3.4   The Argon Neutrino Test (ArgoNeuT) Detector

The Argon Neutrino Test (ArgoNeuT) experiment on the NuMI beam at Fermilab (see Section 2.4) was the first LArTPC in a low energy neutrino beam, the first LArTPC in a neutrino beam in the USA, and the beginning of the Fermilab and USA LArTPC program. Figure 3.2 shows the detector in the NuMI hall, in front of the MINOS near detector.

It was initially proposed as a test experiment to study the performance of a
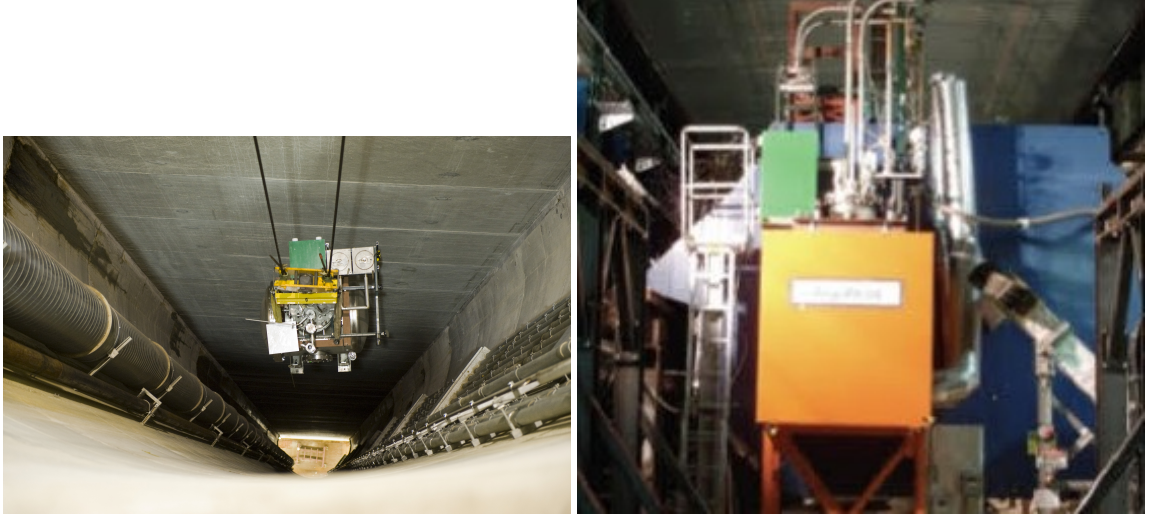
Figure 3.2: Left: the ArgoNeuT detector is lowered in the MINOS near detector pit. Right: the ArgoNeuT detector (orange in the picture) is placed in front of the MINOS near detector.

LArTPC in a neutrino beam, but has since produced a number of important physics papers that were first of their kind. The ArgoNeuT detector collected neutrino and antineutrino events in the Fermilab NuMI beamline at the MINOS near detector hall from September 2009 through February 2010. The NuMI beamline operated in antineutrino mode, and data collection corresponded to $1.25 \cdot 10^{20}$ protons on target (POT) during which both the ArgoNeuT and MINOS near detector were operational. ArgoNeuT made the first measurements of inclusive muon neutrino charged-current cross sections on argo [62], it characterized the performance of the detector [63], [61], it has made high impact measurements of short-range correlated pairs and back to back protons [64] and coherent pion production [65] and the first observation of low energy electron neutrinos in a LArTPC [66]. The ArgoNeuT TPC is a rectangular parallelogram volume of liquid argon that measures 40 cm high (Y direction), 47 cm wide (X direction), and 90 cm long (Z direction). This volume corresponds to about 170 liters, 235 kg, of liquid argon. The TPC is inserted in double-wall, vacuum jacketed and super-insulated cryostat able to contain 550 liters of pure liquid argon, $\sim$0.76 t, and is located about 1 km away from the NuMI target, 100 m below ground level. In its running configuration, neutrinos from Fermilab NuMI beam (See Section 2.4) enter nearly parallel to the Z direction, with a slight downward direction, in particular cosx = 0, cosy = -0.058, cosz = 0.998. On the left side of the detector in the beam direction is the high voltage cathode, providing a uniform electric field of 500 V/cm throughout the TPC (corresponding to approximately -23 kV of voltage at the cathode). Opposite the cathode is the

anode, composed of three wire planes, of which only two are instrumented for read-out. More pictures of the ArgoNeuT detector can be found in 3.3.
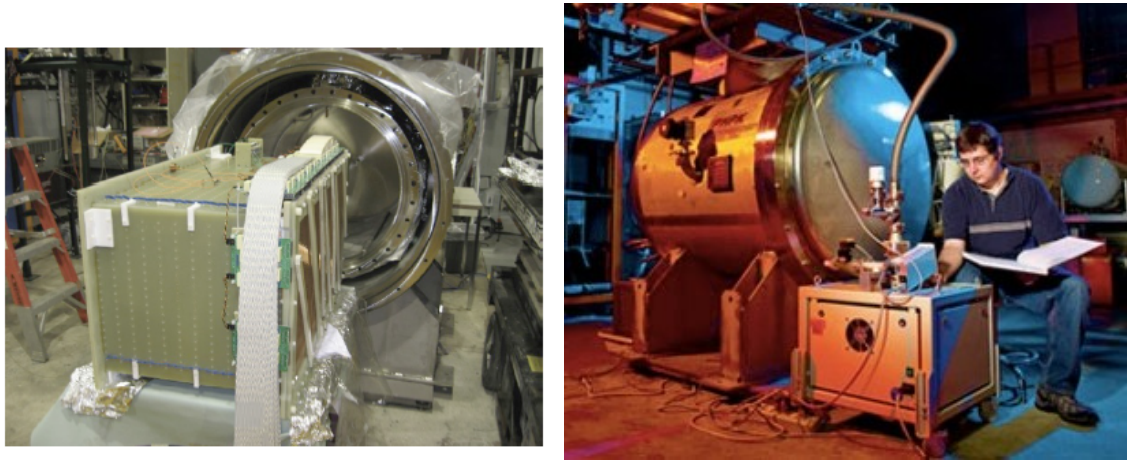
Figure 3.3: Left: the ArgoNeuT TPC positioned just outside of its cryostat. The wire planes and the read-out electronics are visible on the right side of the TPC. Right: the ArgoNeuT cryostat during the test phase.

The uniformity of the electric field in the ArgoNeuT detector is maintained with a system of field shaping electrodes. The electrodes are plated on to the interior surface of the volume between the cathode and anode, and are held at a linearly decreasing voltage from cathode to anode. In ArgoNeuT, the field shaping strips are 1 cm wide and separated by 1 cm from each other, there are 23 strips in total. This technique, however, is used in a variety of TPC experiments. Once the electrons have been separated from the ions, they drift towards the read-out wires of the TPC. Although argon itself does not attach electrons, impurities in the argon can do so. The amount of drifting electrons declines as a function of the distance they have drifted. This decline is well modeled with an exponential decline, and the decay constant is referred to as the electron "lifetime". Proper calorimetry must take the lifetime of the electrons into account on a hit by hit basis to correctly account for the effect of the impurities in the liquid argon. In ArgoNeuT, the electron lifetime is measured in data by comparing the amplitude of hits from crossing muons at different drift distances, as seen in Figure 3.4.

The ArgoNeuT detector has three planes of wires at the anode, with a spacing gap of 4 mm between each other, only two of which are instrumented. The first plane, composed of 225 wires oriented vertically, serves as a shielding plane for the other wires and to provide shaping to the electric field through the TPC. The second plane, referred to as the "induction plane", contains wires that are set at +60 degrees with respect to the beam axis. As electrons cross the shield plane, they approach the induction plane wires. The wires are electrically biased, however, such that the
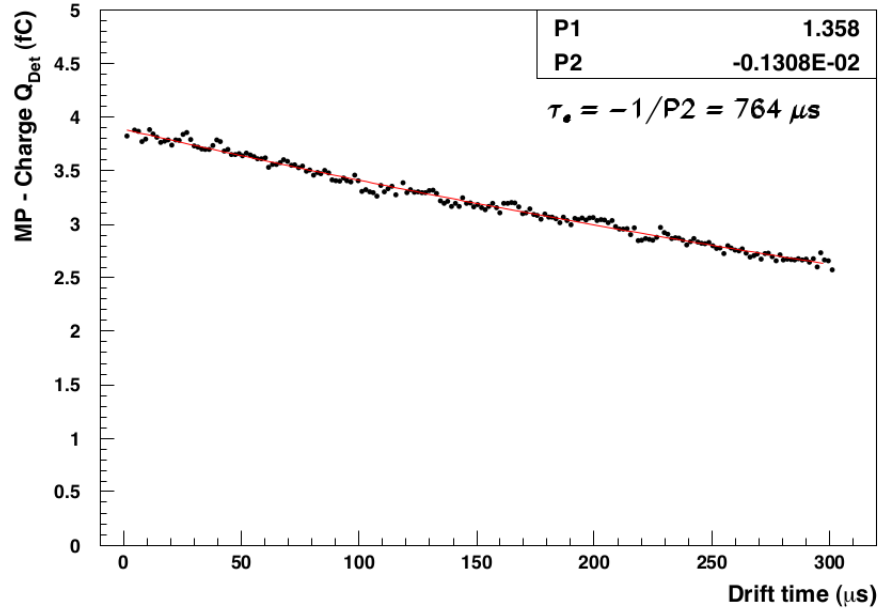
Figure 3.4: With the exponential fit the electron lifetime is found to be 764 μs.

electrons drift around the individual wires. The approaching and subsequent passing of electrons induces a current on these wires (hence the name "induction plane") and the bipolar pulse shape is recorded by the read-out electronics for wires that observe electrons. See Figure 3.5 for examples of this pulse.

The final set of wires, named the "collection plane", is biased such that it collects the drifting electrons onto it, they are observed as a pulse of charge by the electronic system. The collection plane is set at an angle of -60 degrees with respect to the beam direction. The two instrumented planes each have wire spacing of 4 mm and sample at 5.05 MHz. In total, the instrumented planes have 240 wires in each plane. Since the wires are at an angle with respect to the TPC axis, not all wires have the same length. Most wires, 144 out of 240 in each plane, are 46.2 cm long. The shortest wires are instead 3.7 cm long. The sense wires are read-out with a system of electronics samples every 198 ns. The signal to noise ratio is 15 or higher for minimally ionizing particles in the TPC. A much exhaustive description of the ArgoNeuT read-out electronics can be found in [67]. A sketch of the ArgoNeuT detector and wire planes can be seen in Figure 3.6.

The ArgoNeuT experimental layout is complemented by a system of four planes of scintillator ("paddles") to augment the trigger system. Each paddle consists of 16 scintillator bars with wavelength-shifting fibers glued onto the bars. The scintillator bars are 58.5 cm in length, with the innermost eight scintillator bars 3 cm in width and the outermost eight scintillator bars 4 cm in width. The fibers from all 16
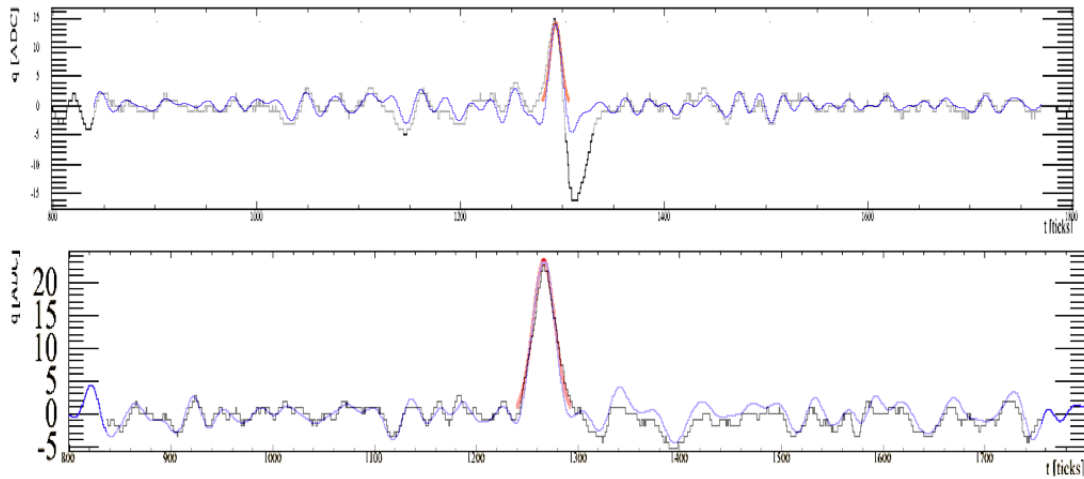
Figure 3.5: Raw and deconvoluted signal shapes from the ArgoNeuT detector. On the top the induction pulse is shown. The bipolar shape of the pulse in the induction plane is corrected during the deconvolution stage. On both planes, a Gaussian hit fitting technique is used to determine the amount of charged recorded. Figure from [67].
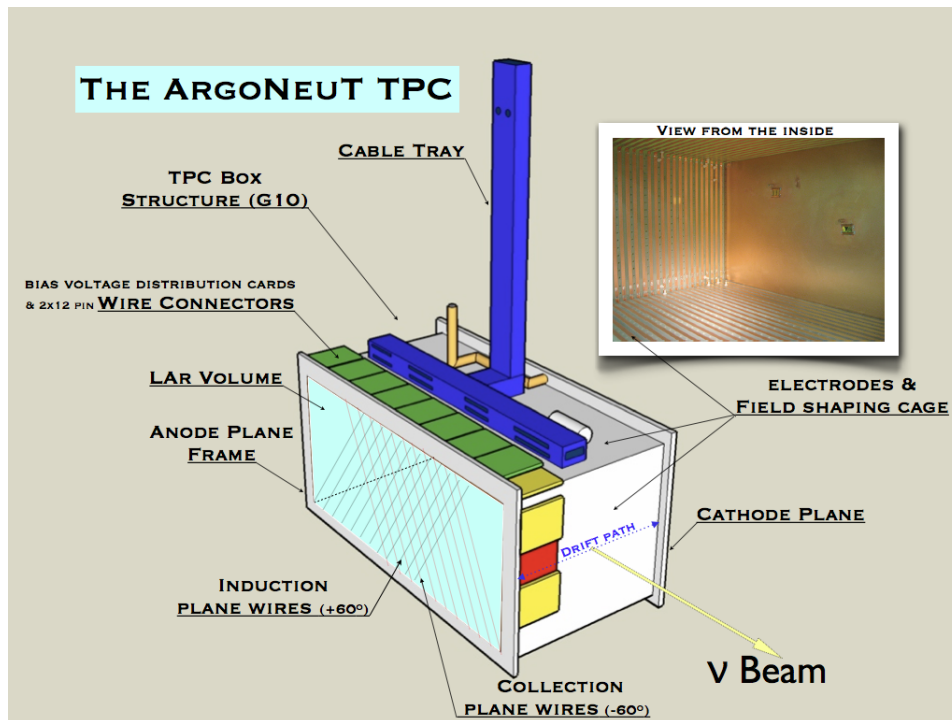
Figure 3.6: Pictorial view of the ArgoNeuT LArTPC. Details of the anodic structure with the ($\pm$60 degrees) inclined wire-planes are indicated. In the top right corner, a picture of the inside of the LArTPC volume shows the cathodic plane and the copper strips of the field shaping cage. Figure from [67].
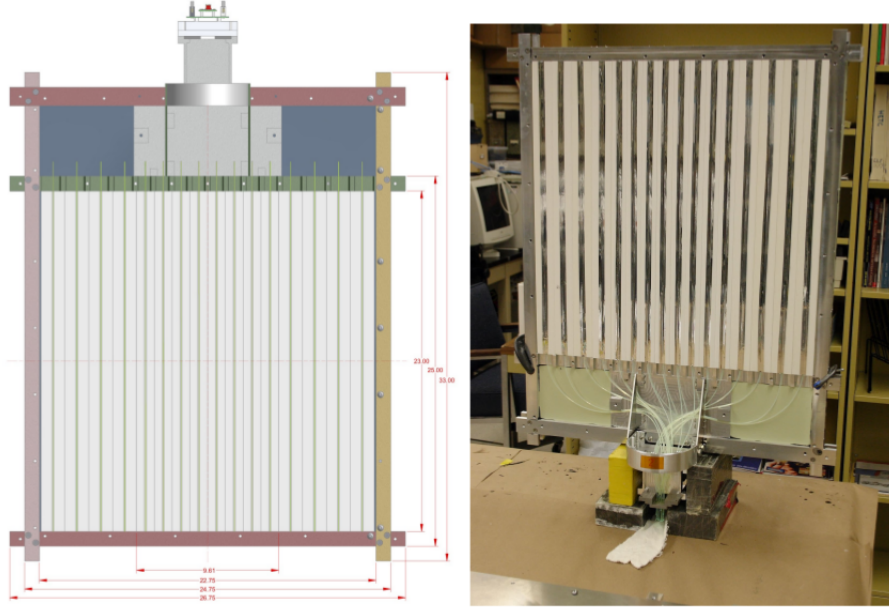
Figure 3.7: [Left] Schematic drawing of ArgoNeuT scintillator paddle design, and [Right] a paddle under construction. Figure from [67].

scintillator strips of the paddle are routed to a multianode photomultiplier tube, as shown in Figure 3.7.

The photomultiplier tubes (one per paddle) are operated at a slightly different (negative) voltage bias adjusted to achieve equal single count rate ($\sim$30 Hz). A pair of paddles with scintillator strips oriented at 90 degrees with respect to one another are located on both the upstream and the downstream end of the cryostat. The paddles are approximately centered on the TPC area. The signals from the scintillator paddles are passed to NIM discriminators, which in turn pass their output signals to a Time-To-Digital Converter board in a CAMAC crate. Arrival times of pulses above threshold are recorded relative to the arrival of the signal from the Fermilab accelerator complex, which indicates delivery of protons to the NuMI target. Figure 3.8 shows the time at which at least one upstream and one downstream ArgoNeuT scintillator paddle recorded signals above threshold with respect to NuMI spills. The characteristic structure of the NuMI beam [68], which is delivered in either 5 or 6 batches per spill (in 5-batch mode either the first or last batch is not delivered to NuMI) over a Δt spill = 9.7 μs window, is clearly evident. The delay of $\sim$215 μs between the accelerator signal and the beam arrival time as well as the spill duration are consistent with expectation. The scintillator paddles are not used to trigger on events, but rather are intended to reduce the uncertainty on the absolute time of interactions (t_0) detected by the TPC. Since there is no internal light collection in

ArgoNeuT, t_0 cannot be determined to a resolution smaller than the Δt spill beam window without incorporating some external constraint. By combining the TPC information with the scintillator paddle information, the uncertainty on the t_0 can be substantially reduced leading to improved resolution on the drift-coordinate of particle tracks, which in turn improves the ability of ArgoNeuT to match tracks to the MINOS-ND.
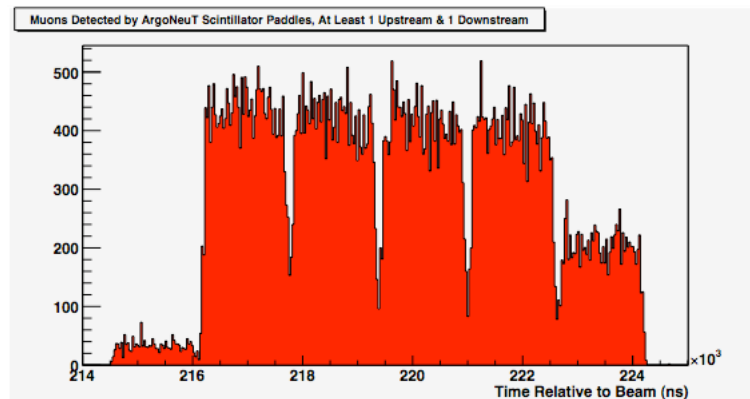
Figure 3.8: [Left] Timing for spills that triggered at least one upstream and one downstream ArgoNeuT scintillator paddle. Figure from [67].

ArgoNeuT is only 90 cm long, and since the NuMI beam has neutrino energies of some GeV, it is extremely rare for muons produced in ArgoNeuT to stop within the detector. ArgoNeuT was placed directly upstream of the MINOS near detector, which is a magnetized tracking detector [69]. This gave ArgoNeuT a distinct trait that no other LArTPC had had: muon sign selection for muons produced in ArgoNeuT that enter the MINOS near detector. This enabled several precision measurements of muon neutrino cross sections on argon by looking for neutrinos that interact in ArgoNeuT, and tracking muons from neutrino interactions through the MINOS near detector [62]. For the analysis presented in this thesis, MINOS is used as a muon spectrometer for sign recognition and momentum measurements.

3.5   ArgoNeuT - Event Imagining and Reconstruction

One of the major advantages of a LArTPC to other neutrino detection technologies is the ability to do precision imaging and calorimetry. In this section, the standard chain of reconstruction algorithms is described to show how the high resolution images are transformed into physics data. Each wire in the detector measures a signal of electrons as they drift, as a function of time. When the wires are arrayed
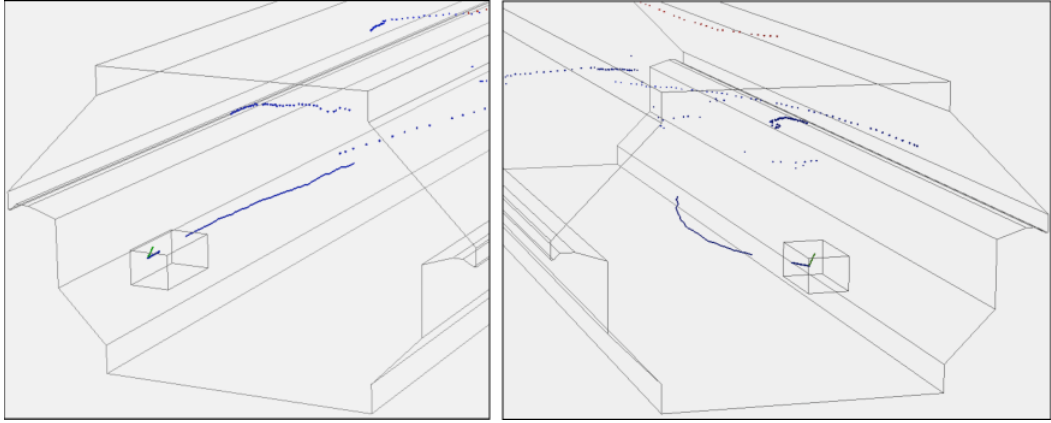
Figure 3.9: An event is presented, showing the ArgoNeuT detector, the small box in the foreground, and MINOS near detector in the background. The blue tracks represent TPC data on ν_μ CC interactions that are succesfully tracked and matched into the MINOS near detector. Figure from [67].

in an image in sequential order, such that the x-axis corresponds to wire number and the y-axis corresponds to time tick, 2D images are formed, such as in Figure 3.10.
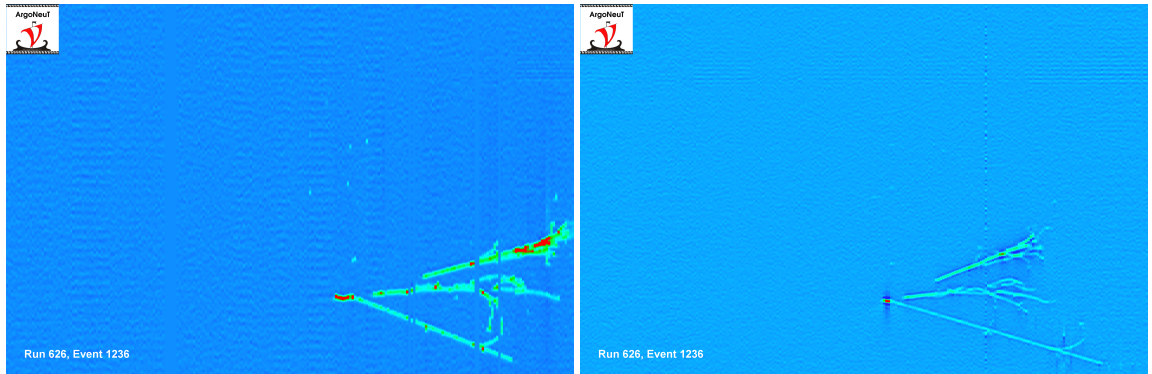
Figure 3.10: Example of an ArgoNeuT event. The horizontal direction, from left to right, represents increasing wire number. The vertical direction is the drift distance. An artificial color scaled is applied to highlight charge deposition above noise levels. Left image is the collection plane, right one is the induction plane.

3.5.1 Deconvolution

The reconstruction of these images into a 3D event starts at the lowest level, with a filtration and a deconvolution of the wire signals. In general, the number of electrons recorded by a given wire as a function of time is not perfectly matched by the ADC signals read by the detector, due to the response of the detector electronics and noise effects. To correct for this, a deconvolution process is needed and applied to

each wire. As seen in Figure 3.11, the response of the detector to a delta function introduces a spread of signal which is removed using a scheme with the Fast Fourier Transform (FFT).
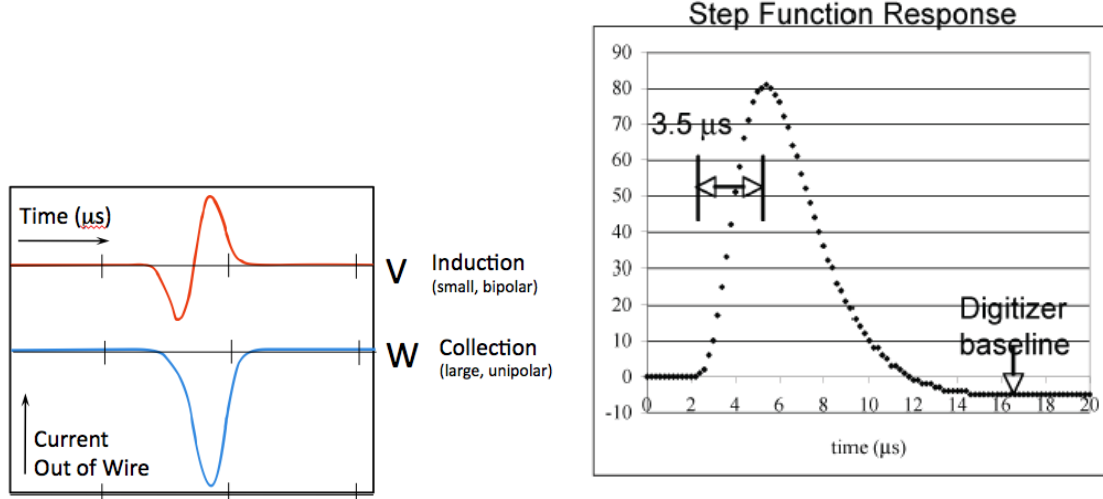
Figure 3.11: On the left, an image of the idealized detector response to drift electrons in the induction and collection plane. On the right, the response of the elctrons filter and digitalization to a delta function pulse. Figure from [67].

The response of each channel is measured with external pulse generators. The convolution theorem then allows the removal of the detector response by taking the inverse Fourier transform of $\dfrac{v[t]}{r[t]}$, where $v[t]$ is the Fourier transform of the recorded waveform and $r[t]$ is the Fourier transform of the channel response. Figure 3.5 shows the result of applying deconvolution to ArgoNeuT data in the collection and induction planes. In addition, the deconvolution for the induction plane removes the bipolar behavior to make hit finding easier.

3.5.2   Hit Finding

For each wire in the detector, a hit finding algorithm is used to locate the regions of the read-out with electron deposition signals. While there are several different hit finding algorithms available in LArSoft [70], the official LArTPC reconstruction software, they all follow a generalized procedure.

- A deconvolved (and noise filtered) wire signal is scanned for regions of signal above a specified threshold. The threshold of hit finding depends on whether the signal is from collection or induction planes as the two planes have different signal to noise ratios.

- The regions of interest are fitted, typically with a Gaussian, to allow a precise determination of the time tick, peak and integral of the deposited charge.

In some cases, hits that are close to each other from different particles will have overlapping regions. In these cases, the multiplicity of the region above threshold can be determined to help tracking algorithms accurately distribute hits between different particles. An example of this is seen in Figure 3.12. In general, complicated regions with multiple hits are fit with several Gaussian functions summed together.
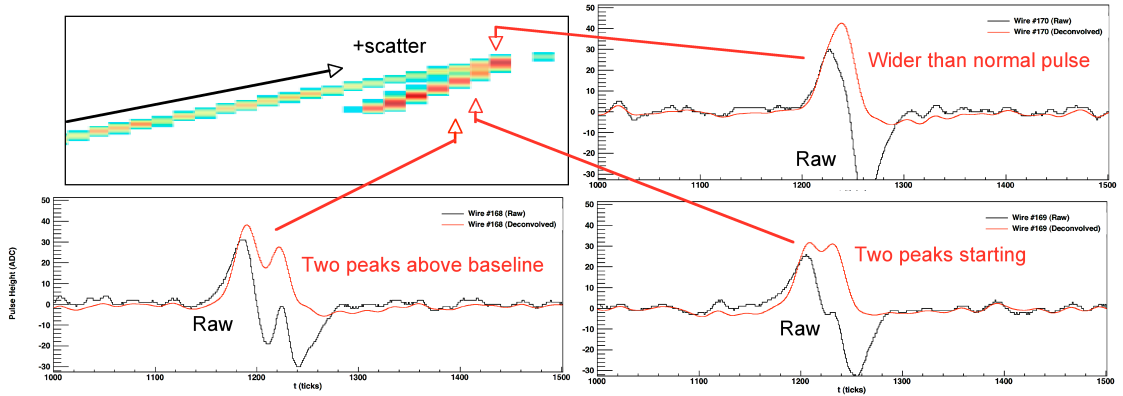
Figure 3.12: A neutrino vertex as seen in the induction plane in the ArgoNeuT detector. The top left shows the reconstructed signals above threshold. The other figures show the wire signal moving away from the vertex: the initial signal is wider than normal, and as the tracks diverge in the detector the two peaks are resolved. Figure from [67].

3.5.3 Cluster, Tracking and 3D Reconstruction

Once the wire is signals have been deconvolved, and the signal depositions have been reconstructed as hits, a number of higher level steps separates hits and physics data. First, hits must be grouped together according to which particle they are originated from. In general, this is an extremely difficult problem with no simple answer. For particles like muons and protons, which produce simple, linear tracks of hits in the detector, it is not impossible and a lot of progress has been made. For more complicated events, such as electromagnetic showers and deep inelastic scatter events, clustering remains the weakest point of the reconstruction chain. For a track like particle, in general, the groups of hits are associated together into clusters by finding sets of hits that are well aligned linearly. These clusters are then matched across the planes of the detector (two planes in ArgoNeuT). Though the planes offer different projections of the 3D events into 2D, the drift direction (vertical direction in 3.10) is a common axis in every projection. The most useful metric to determine if

two clusters are from the same track in the argon is the time it took those clusters to drift to the wires. Once clusters from multiple planes have been matched together, the wire information between the two clusters can be used to determine where in the Y-Z plane the clusters overlap. This is because each wire intersects the other plane wires at most once, so if a charge deposition from one plane is matched to one on another plane, it uniquely determines the location of the 3D charge (The X coordinate comes from the drift time, knowing the drift velocity in liquid argon, $v_d = 1.57 \pm 0.02$ mm/μs [67]). A great detail of knowledge and techniques can be found here [71].

3.5.4   Calibration

The calibration of the response to charge depositions on the wires was performed with large sample of crossing muons as reported in [63]. Muons induced from upstream neutrino interactions (known as "through-going muons" in ArgoNeuT) have been used as a known source of ionization in the detector. To calibrate the detector, the dE/dx of each deposition measured by the wires of the TPC can be collected into a histogram and the shape is fit with a Gaussian and a Landau distributions convoluted.

The calibration constants are calculated by imposing the most probable value of the distribution, which is a parameter of the fit, to be 1.73 MeV/cm, the theoretical value corresponding to the mean momentum of the through-going muons, which is 7 GeV/c. This process repeats until the calibration constant produces a distribution of hits that agrees with theoretical values of ionization per centimeter. The calibration used for the analysis presented in this thesis includes:

- new calibration constants calculated on a wire-by-wire basis;

- calibration constants calculated for both the collection and the induction plane.

The average calibration constants for each plane are determined to be 36.4 ± 2.48 [fC/(ADC·(time sampling))] for the collection plane, and 143 ± 10.3 [fC/(ADC·(time sampling))] for the induction plane.

3.5.5   Particle Identification and Calorimetry

In a LArTPC, the calorimetric identification of particles is based upon the behavior of charged particles moving through the argon. The energy deposited per centimeter is ruled by the Bethe-Bloch equations, as reported in Figure 3.13.
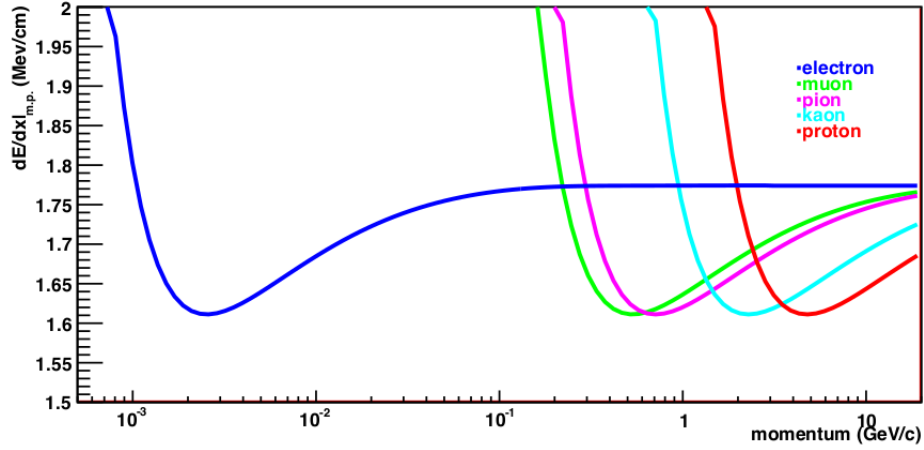
Figure 3.13: Energy loss per centimeter as a function of the momentum in liquid argon for a variety of particles.

As a particle travels in a media and loses energy, its amount of ionization decreases until it reaches a minimum before the ionization spikes to very high values. The observed dE/dx values for a given particle increases as the particle comes to a rest. As seen in Figure 3.14, the measurement of dE/dx versus residual range allows calorimetric separation of particles. In particular, protons are easily separated from muons and pions with this measure. Some difficulties occur in cases when a certain particle, produced in the detector, leaves it without stopping in it. Because of the behavior of the dE/dx versus residual range, the most interesting part is in fact the ending part before the particle come to rest, not knowing the values of this variable in the final section of the track can result in misidentification.

Since LArTPCs also offer bubble chamber quality images, the topology of an event can give excellent ways to distinguish particles. As seen in Figure 3.15, particles like muons and pions that are difficult to distinguish with calorimetry can often be separated based on subsequent interactions within the TPC.

3.6   Current and Future LArTPCs

The whole United States accelerator based neutrino physics program has selected the LArTPC detectors to be the detectors of future neutrino field researches. They provide full 3D imaging, precise calorimetric energy reconstruction, efficient particle identification and allow for exclusive topology recognition and nuclear effects exploration from detailed studies of the hadronic part of the final states. All these features make the LArTPC detectors the ideal detectors for the few-GeV neutrino
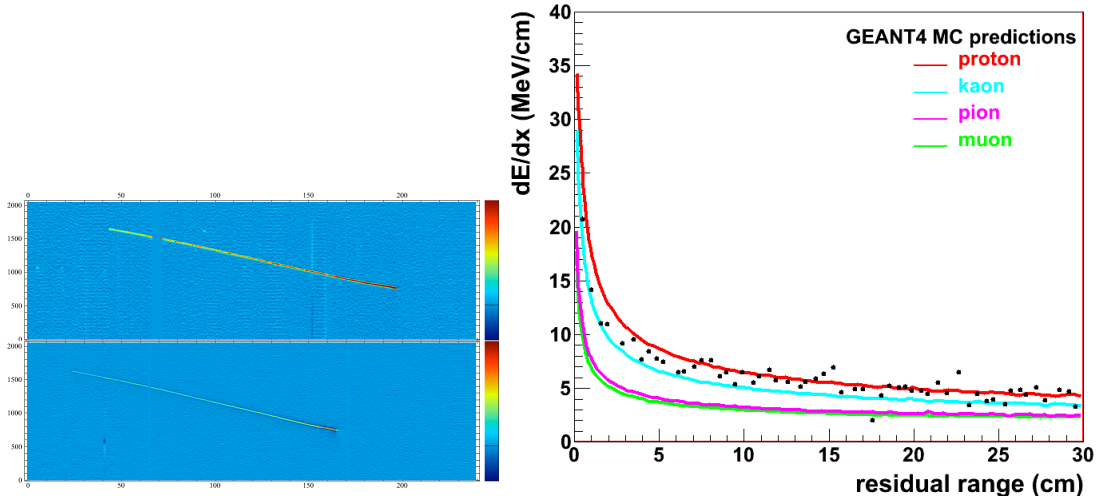
Figure 3.14: (Left) A fully contained particle in the ArgoNeuT detector, where top refers to the collection plane view while bottom refers to the induction plane view. The values of dE/dx versus residual range are used to identify the reconstructed track. (Right) Theoretical dE/dx versus residual range for various particles in liquid argon. The black points represent the GEANT4 MC prediction for the particle reported on the left. The particle is identified as a proton.

scattering measurements. ArgoNeuT, the main subject of this chapter, was the first LArTPC in a neutrino beam in the USA and the start of the USA LArTPC neutrino program. ArgoNeuT collected data on the NuMI beam in 2009-2010. In the same period another LArTPC was already proposed, MicroBooNE. Since then, LArTPCs have become the detector of choice for neutrino physics in the GeV energy range in the United States. Today MicroBooNE is working and collecting data on the Booster Neutrino Beam (BNB, see Section 2.3) at the Fermi National Laboratory, and in a few years other two LArTPCs will join MicroBooNE, the Short-Baseline Near Detector (SBND) and ICARUS-T600 detector to form what has been called the Short-Baseline Neutrino Program (SBN). Another very larg size LArTPC has already been proposed and is currently in the design phase, DνNE, a four cryostats detector that will hold combined a total of 68,000 tons of liquid argon as the target material, it will operate in the next future and will be part of the Long-Baseline Neutrino Program as far detector [72]. MicroBooNE, SBND and ICARUS-T600 are briefly described in the following sections.

3.6.1   MicroBooNE

MicroBooNE [73] is the successor to MiniBooNE [74] and is designed to confirm or rule out the MiniBooNE "Low Energy Excess", described in Section 1.5.1. Micro-
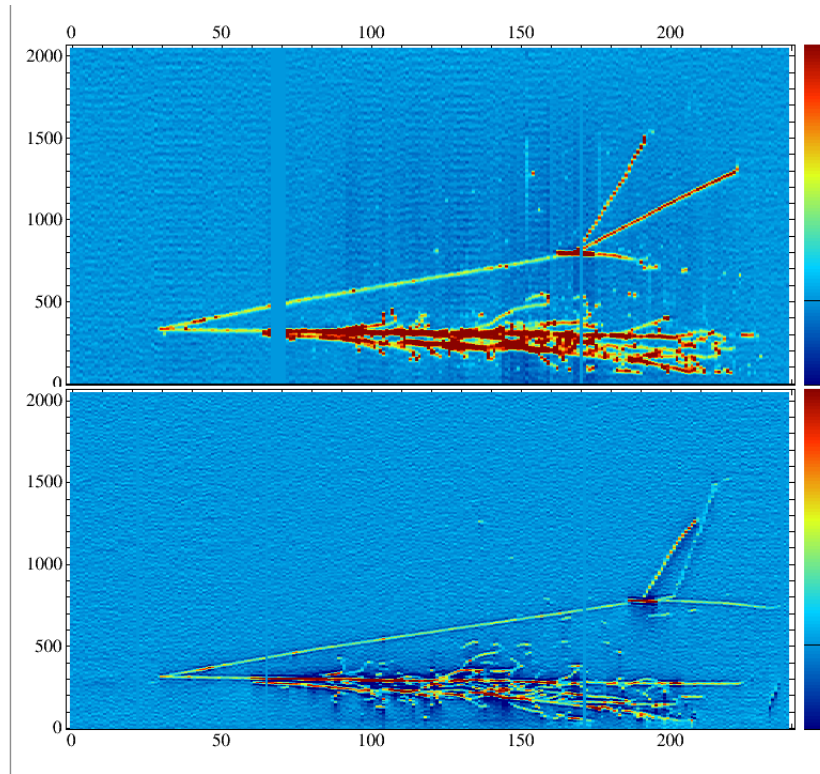
Figure 3.15: An ArgoNeuT event with an electromagnetic shower and a pion inter-acting with an argon nucleus through a hadronic interaction. The resulting topology of many particles from the secondary interaction can be used to identify this track as a pion and not as a muon. Top view is the collection plane, bottom view is the induction plane.

BooNE is a large TPC, 170 tons of total liquid argon mass of which about 89 tons of active volume, see Figure 3.16, located on-axis in the BNB, 470 m away from the BNB target.
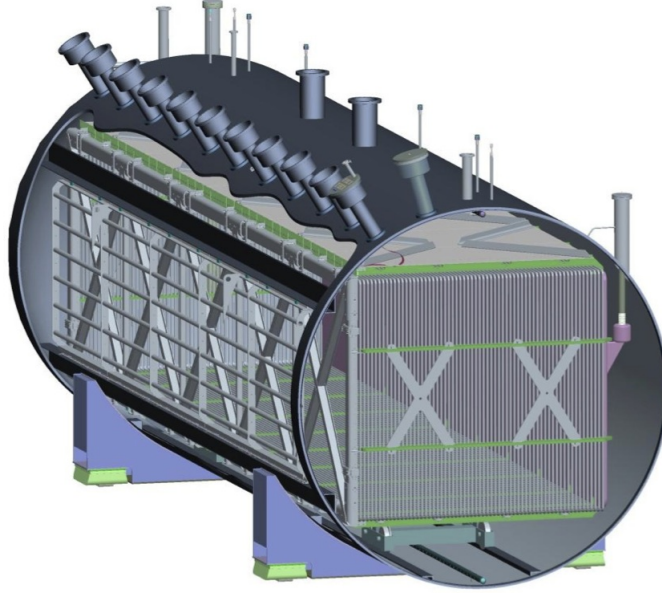
Figure 3.16: A schematic image of the MicroBooNE detector as it was designed. The beam enters from the bottom right side of the detector, along the longest axis. The high voltage cathode is on the right while the sense wires are on the exposed left side where the cryostat has been cut away.

The most notable differences, other than size, with respect to ArgoNeuT, are the third instrumented wire plane and the PMT system for light collection. Additionally, the wire spacing in MicroBooNE is 3 mm, decreased from 4 mm in ArgoNeuT. On the physics side, MicroBooNE is providing exceptional data for studying neutrino interactions, particularly in understanding nuclear physic effects in neutrino interactions. MicroBooNE has the finest 3D resolution of any calorimetric neutrino detector to date, allowing it to measure the outgoing hadrons (protons, pions, neutrons, kaons, etc.) from a neutrino interaction. MicroBooNE expects high statistics in many interesting neutrino cross section channels, as shown in Table 3.1.

MicroBooNE also introduces a number of important Research and Development (R&D) achievements to the field of LArTPCs. It is the first large scale LArTPC to achieve high purity without evacuating the cryostat. Instead, the TPC used a purge of high purity argon gas to push impurities out of the cryostat before cooling the cryostat and filling with liquid argon. In this way, critical impurities were removed from the detector. Additionally, MicroBooNE employs cold read-out electronics immersed in the liquid argon. Another significant improvement that MicroBooNE

Table 3.1: Estimated event rates using GENIE (v2.8) in a $6.6 \cdot 10^{20}$ POT exposure of MicroBooNE, located 470 m from the neutrino source, the BNB. In enumerating proton multiplicity, there is a kinetic energy threshold on protons of 20 MeV. The 0 π topologies include any number of neutrons in the event. This study uses a 17 cm fiducial volume cut in MicroBooNE, which gives a fiducial volume of 61 t.

Process		No. Events
	ν_μ Events by Topology	
CC Inclusive		122,100
CC 0 π	ν_μ N $\rightarrow \mu$ + Np	78,500
	$\cdot \nu_\mu$ N $\rightarrow \mu$ + 0p	16,500
	$\cdot \nu_\mu$ N $\rightarrow \mu$ + 1p	44,200
	$\cdot \nu_\mu$ N $\rightarrow \mu$ + 2p	8,300
	$\cdot \nu_\mu$ N $\rightarrow \mu + \geq$ 3p	9,500
CC 1 $\pi^\pm$	ν_μ N $\rightarrow \mu$ + nucleons + 1$\pi^\pm$	30,300
CC $\geq$ 2 $\pi^\pm$	ν_μ N $\rightarrow \mu$ + nucleons + $\geq$ 2 $\pi^\pm$	2,700
CC $\geq$ 1 π^0	ν_μ N $\rightarrow \mu$ + nucleons + $\geq$ 1 π^0	13,400
NC Inclusive		45,900
NC 0 π	ν_μ N $\rightarrow \mu$ + nucleons	29,900
NC 1 $\pi^\pm$	ν_μ N $\rightarrow \mu$ + nucleons + 1$\pi^\pm$	6,900
NC $\geq$ 2 $\pi^\pm$	ν_μ N $\rightarrow \mu$ + nucleons + $\geq$ 2 $\pi^\pm$	900
NC $\geq$ 1 π^0	ν_μ N $\rightarrow \mu$ + nucleons + $\geq$ 1 π^0	9,200
	ν_e Events	
CC Inclusive		820
NC Inclusive		290

brings that ArgoNeuT did not have is the addition of a light collection system. A light collection system is essential for detectors like MicroBooNE running on the surface and not deep underground. The MicroBooNE light collection is composed of 8 inch Photo-Multiplier Tubes (PMTs) arrayed behind the wire planes. Argon scintillates at a vacuum ultraviolet wavelength (to which liquid argon is transparent), but the PMTs detect visible light. So, each PMT has a wavelength shifting plate to convert the vacuum ultra violet to visible light detectable by the PMTs. On the surface, MicroBooNE is exposed to a high flux of cosmic rays, as many as ten cosmic ray interactions in the detector each read-out window of 4.8 ms. On the other hand, the detector is exposed to the neutrino beam for just several μs. Though the wire information can not be used to identify precisely when an interaction occurred in the TPC, the PMT information detects flashes of light with each particle interaction and can localize interactions in a much tighter region of time. This provides two advantages: first, if the time of an interaction is known (particularly cosmic interactions), the corrections that must be applied as a function of drift distance (such as lifetime corrections) can be accurately applied. Second, and more important for a successful operation of the detector, the PMT system provides a triggering system for the beam interactions. MicroBooNE began taking neutrino data in the fall of 2015, and collected approximately $4.4 \cdot 10^{20}$ POT (about 2/3 of its data set) by May 2017. MicroBooNE will lead the Fermilab Short-Baseline Program forward as the first running LArTPC on the BNB, which is an exciting step forward in the USA LArTPC program.

3.6.2 Future LArTPCs

The future SBN will include three LArTPCs located on-axis in the Booster Neutrino Beam (BNB) at Fermilab. The three detector, Short-Baseline Near Detector (SBND), MicroBooNE and ICARUS-T600, will be located, respectively 110, 470 and 600 m away from the BNB target, on the same axis. The SBN Projects was proposed with the intent to provide definitive measurements of the LSND and MiniBooNE anomalies and to search for sterile neutrinos. As mentioned above, MicroBooNE is the newest LArTPC to the Fermilab SBN, but there are two other LArTPCs planned to begin operation within several years on the BNB at Fermilab. In this brief Section, a few selected details of these detectors are listed as they are both critical components of the SBN program and essential to resolving short-baseline neutrino anomalies.

Short-Baseline Near Detector (SBND)

Along the BNB, SBND will be the LArTPC closest to the neutrino source. It is currently under design and construction, with final assembly taking place in 2017 and 2018, once ready the total volume will contain 220 tons of liquid argon with an active volume of 112 tons. Unlike MicroBooNE, SBND is a dual drift TPC with the high voltage cathode in the middle of the TPC, and three sets of read-out wires on each side. SBND is driving forward the USA LArTPC program with important R&D tasks, including the manufacture of Cathode Plane Assemblies (CPA) and Anode Plane Assemblies (APA). Like MicroBooNE, SBND will feature a light collection system and an external cosmic ray tagging (CRT) system to trigger neutrino events and accurately determine cosmic timing, see Figure 3.17.
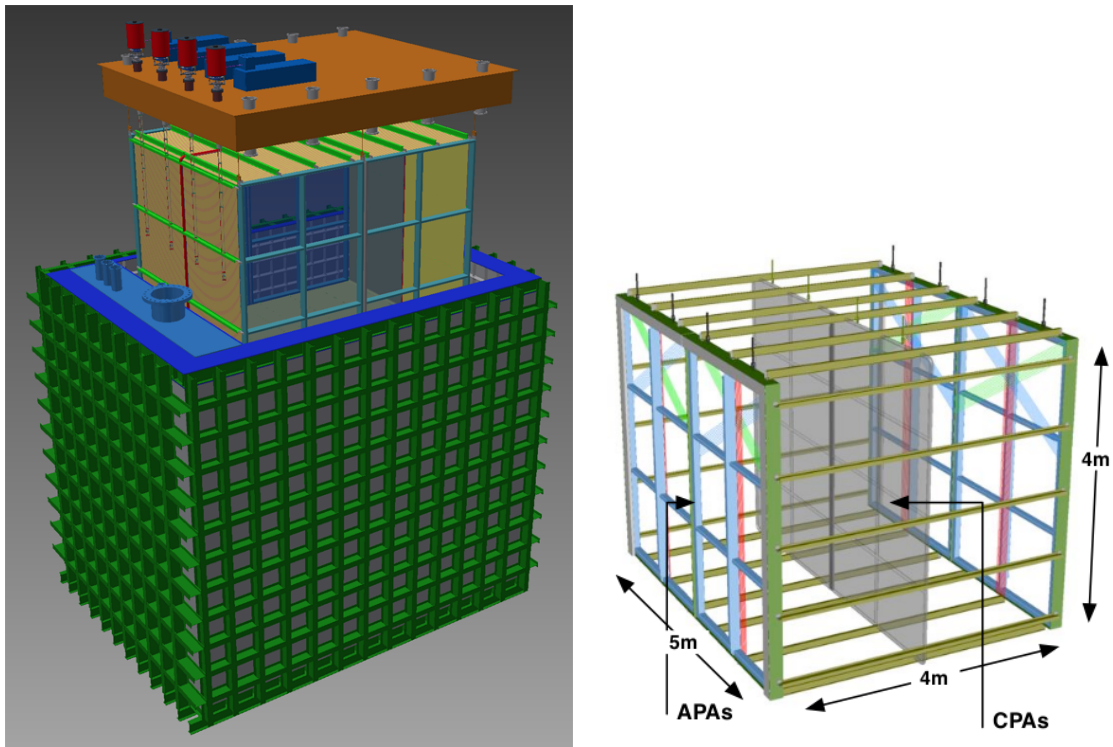
Figure 3.17: (Left) A conceptual design of the SBND detector. (Right) A model of the TPC, showing the four bridged APAs and the central CPAs.

Due to the proximity of SBND to the BNB target, 110 m, and the high power of the BNB, SBND will have the highest statistics measurements of neutrino interactions of any LArTPC to date. With over 1 million events per year, SBND records statistics equivalent to the MicroBooNE data set in just one month (and it matches the statistics of ArgoNeuT in just one day!). I personally worked in the summer of 2015 as a summer student at Fermilab, where I spent 3 months, with the SBND collaboration on expectations for neutrino argon interactions. I was given a simulation

Table 3.2: Estimated event rates for muon and electron neutrino charged-current 0π final state channels using GENIE (v2.8) in the SBND active volume for a $6.6 \cdot 10^{20}$ POT exposure. In enumerating proton multiplicity, we assume an energy threshold on proton kinetic energy of 21 MeV. The 0π topology includes any number of neutrons in the event. Tables from [75].

CC 0 π ν_μ events		
Process	**N. events**	**Stat. uncert. (%)**
INCLUSIVE	3,503,955	0.05
QE	3,064,670	0.06
RES	357,035	0.17
DIS	79,847	0.35
0p	765,347	0.11
1p	2,014,640	0.07
2p	356,401	0.17
3p	163,532	0.25
4p	89,408	0.33
$\geq$5p	114,627	0.30

CC 0 π ν_e events		
Process	**N. events**	**Stat. uncert. (%)**
INCLUSIVE	22,279	0.67
QE	18,551	0.73
RES	2,694	1.93
DIS	964	3.22
0p	4,535	1.48
1p	12,177	0.91
2p	2,307	2.08
3p	1,268	2.81
4p	759	3.63
$\geq$5p	1,234	2.85

made with GENIE (v2.8) in the SBND active volume corrresponding to a period run of 3 years, $6.6 \cdot 10^{20}$ proton on target (POT), and I analyzed charged-current 0π and 1π final state channels and rare channels such as neutrino elastic scattering [75]. Some results from this study are reported below, see Tables 3.2 and 3.3.

With this expected event rate, SBND can probe rare neutrino interactions with high statistics. The high event rate also allows precision measurements of final state topologies of neutrino interactions, which in turn is essential for tuning neutrino interaction models for DνNE.

ICARUS-T600

ICARUS-T600 is the first large scale LArTPC. The detector is approximately 760 tons of total volume, 476 tons of active argon divided into two modules (known as T300 each). The two modules were deployed together at the Gran Sasso National Laboratories (LNGS) in Italy, underground, where they were exposed to the CERN Neutrinos to Gran Sasso (CNGS) neutrino beam in 2011-2013. The ICARUS-T600 detector is the biggest LArTPC ever realized. Its construction finalized many years of R&D studies by the ICARUS Collaboration [76], [77], [78] with prototypes of growing mass developed both in laboratory and with industry involvement. Nowa-

Table 3.3: Estimated event rates for muon and electron neutrino charged-current 1π final state channels using GENIE (v2.8) in the SBND active volume for a $6.6 \cdot 10^{20}$ POT exposure. In enumerating proton multiplicity, we assume an energy threshold on proton kinetic energy of 21 MeV. The 1π topology includes any number of neutrons in the event. Tables from [75].

CC 1 π ν_μ events				CC 1 π ν_e events		
Process	**N. events**	**Stat. uncert. (%)**		**Process**	**N. events**	**Stat. uncert. (%)**
INCLUSIVE	1,056,440	0.10		INCLUSIVE	9,775	1.01
QE	18,785	0.73		QE	164	7.81
RES	809,550	0.11		RES	6,866	1.21
DIS	218,570	0.21		DIS	2,584	1.97
0p	279,525	0.19		0p	2,667	1.94
1p	537,112	0.14		1p	4,667	1.46
2p	155,347	0.25		2p	1,316	2.76
3p	41,585	0.49		3p	505	4.45
4p	19,985	0.71		4p	282	5.95
$\geq$5p	22,878	0.66		$\geq$5p	338	5.44
Pion type	**N. events**	**Stat. uncert. (%)**		**Pion type**	**N. events**	**Stat. uncert. (%)**
π^+	1,036,750	0.10		π^+	9,506	1.03
π^-	19,691	0.71		π^-	269	6.10

days, it represents the state of the art of this technique and it marks a major milestone in the practical realization of large scale liquid argon detectors. The pre-assembly of the ICARUS-T600 detector began in 1999 in Pavia (Italy); one of its two modules was brought into operation in 2001. In preparation for the underground operation at LNGS, a test run lasting three months was carried out with exposure to cosmic rays on the surface, allowing for the first time an extensive study of the main detector features [79]. After the CNGS beam was decommissioned, it was decided to transport the ICARUS-T600 detector from Italy to Fermilab to be used as far detector in the SBN Program. ICARUS-T600 is significantly more massive than both MicroBooNE and SBND, and so it offers the chance to record oscillation spectra from anomalous neutrino oscillations with high statistics. It will be placed 600 m away from the BNB target. Currently, ICARUS-T600 is at CERN where it has been refurbished and upgraded, before it will be shipped to Fermilab for installation in the next months (see Figure 3.18).

Figure 3.18: (Left) The ICARUS-T600 on its way to CERN. (Right) The first transported module inside the clean room at CERN.

Chapter 4

Analysis of CC 1π Production at ArgoNeuT

As described in Section 1.5, the production of one pion in the final state of a neutrino interaction is one of the most relevant in the few GeV neutrino energy range. This Chapter describes the results of the measurements of the cross sections of charged-current single pion production events on argon in the ArgoNeuT detector on the NuMI beam at Fermilab. The Chapter is organized as follows: Section 4.1 gives an overview of the analysis introducing data and Monte Carlo (MC) samples used in the measurement, Section 4.2 describes in details the selection cuts applied to the samples for the event selection, Section 4.3 illustrates how to extract the signal using an estimated background sample. Systematic uncertainties are listed in Section 4.4, while Section 4.5 shows the procedure to carry out the differential and total cross sections.

4.1   Analysis Overview

The basic approach for studying interested physics at neutrino experiments is to measure the cross section of corresponding processes using the information recorded in the particle detector and compare the measured values with theoretical predictions. Necessary selection criteria should be applied to filter the set of recorded events into a sub-sample, in which the interested physics signature dominates or at least results visible. The interested physics process is treated as "signal" while the remaining contributions are referred to as "background". In order to determine the number of signal events, background must be carefully studied, and to calculate the cross section, one needs to extract the selection efficiency of signal events. Furthermore, to maximize the analysis sensitivities, event selection should be op-

timized in a way that the signature is cleaner and the related uncertainties of the estimations are smaller. To achieve these analysis goals, Monte Carlo (MC) simulation is needed. MC simulation usually consists of two steps: the event generation and the detector simulation. The event generator randomly generates events of a specific process according to the preferred theory model. Those generated events go through detector simulation, in which they interact with materials and produce detector signals. The final MC events, tend to be alike the real collision events, this really depends on how tuned the MC generator is, however, the true information that can be extracted from the MC simulation is of fundamental importance. As reported in Section 1.5, the dominant interaction channels change rapidly across the few GeV neutrino energy region. In the energy range of the NuMI beam, from hundreds of MeV to tens of GeV, the description of neutrino charged-current (CC) scattering becomes increasingly more complicated because several distinct neutrino scattering mechanisms start to play a role. Five different mechanisms are included in the MC simulation for this analysis:

- Quasi-elastic (QE): in the scattering the nucleon inside the nucleus changes (if the event is a CC) or it remains the same (in the case of a NC) but it doesn't break up, as the available Q^2 increases, (Q is defined as the momentum transfer from one particle in the initial state to a particle in the final state) it becomes increasingly unlikely for the nucleon to remain intact (dominant for neutrino energies $E_\nu < 1$ GeV);

- Resonant production (RES): the target nucleon is "knocked" into a baryonic resonance, which then decays back down into a nucleon accompanied by a single pion (RES is most significant in the transition region between quasi-elastic and deep inelastic dominance, 0.5 GeV $< E_\nu <$ few GeV);

- Deep inelastic (DIS): at higher energies the neutrino is able to transfer sufficient momentum that the internal structure of the nucleon can be resolved. The neutrino can scatter directly off any of the quarks that appear inside the nucleon, including those which form the "sea" of quarks and anti-quarks. The most visible consequence of DIS is the break up of the nucleon containing the struck quark, which results in "hadronization". This appears as a jet of hadrons (dominant process for $E_\nu >$ few GeV);

- Coherent Pion Production (COH): the nucleus recoils as a whole, unfragmented, in the same state as when the neutrino arrived, it remains unaffected by this interaction. This can only be achieved if the four-momentum transfer

to the nucleus, $|t|$, is kept small since any substantial transfer absorbed by the nucleus would excite or otherwise fragment it and break the coherence;

- Meson Exchange Current (MEC): it is an interaction involved in two nucleons, or in a 2-body current, and it is classified in a "2 particles-2 holes" effect. Here, a weak boson from the leptonic current is exchanged by a pair of nucleons (2-body current), and believed to lead to a 2-nucleon emission. The importance of this process in neutrino interactions was first pointed out shortly after the MiniBooNE experiment showed their results for the CCQE differential cross section [80]. Several groups successfully reproduced the MiniBooNE CCQE cross section data [81] by adding the MEC mechanism in their models [82], [83], [84], [85], [86].

Feynman diagrams of most of the mechanisms can be found in Figure 4.1.
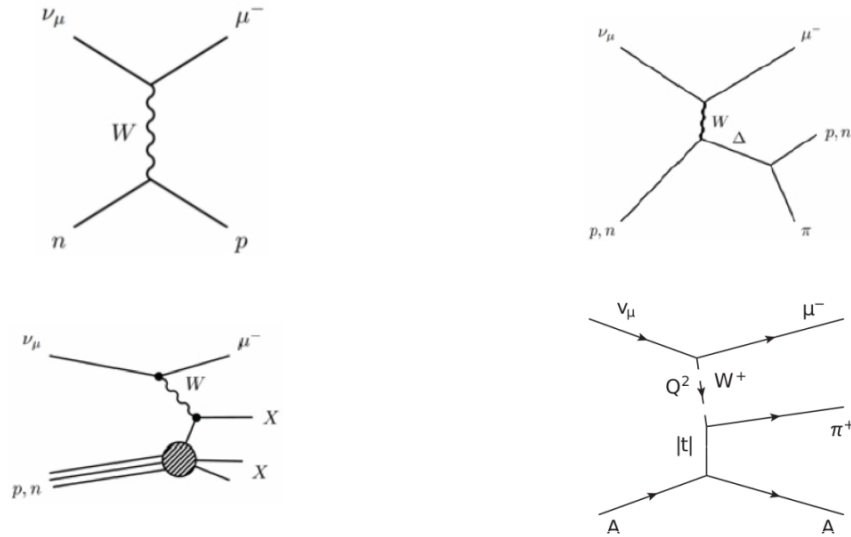
Figure 4.1: Feynman diagrams showing an example of CC event: (Top left) quasi-elastic scattering, (top right) resonant production, (bottom left) deep inelastic scattering, (bottom right) coherent pion production, where here A is a generic nucleus.

The signal selection for this analysis consists of an event with at least two charged tracks starting in the neutrino interaction vertex, one track is the muon, which identifies a charged-current event, the other one corresponds to the charged pion with a momentum higher than 100 MeV/c. No π^0 or kaons are allowed in the final state. Other charged tracks representing protons are accepted because there is not limit on the number of nucleons in the final state. In order to measure the cross section, the number of observed events, an estimate of the number of background events, the efficiency of the selection process, the number of target and the integrated

flux of the data sample are required. The background is estimated using the Monte Carlo (MC) sample. Following event selection, the differential cross section in terms of a generic measured variable u in the bin i is extracted using

$$\frac{d\sigma(u_i)}{du_i} = \frac{N_{measured,i} - N_{background,i}}{\Delta u_i \; \epsilon_i \; N_{targ} \; \phi}$$

where $N_{measured,i}$ represents the number of events in data surviving analysis selection, $N_{background,i}$ is the number of expected background events, Δu_i is the bin width, ϵ_i is the detection efficiency, N_{targ} is the number of argon nuclei in the fiducial volume and ϕ is the total neutrino flux exposure. Eight different differential cross sections are measured in this analysis, four for muon neutrino and four for muon antineutrino. The variable u may represent the outgoing muon momentum (p_μ) or the outgoing muon angle with respect to the initial neutrino direction (θ_μ) or the outgoing pion angle with respect to the initial neutrino direction (θ_π) or the angle between the outgoing muon and pion ($\theta_{\mu\pi}$).

Data Sample

The analysis in this thesis uses data collected by the ArgoNeuT detector. The ArgoNeuT detector collected neutrino and antineutrino events on the Fermilab NuMI beamline at the MINOS near detector hall from September 2009 through February 2010. The ArgoNeuT detector was positioned in front of the MINOS near detector, used as muon spectrometer in this analysis. The measurements reported in the following sections are based on data taken with the NuMI beamline operating in antineutrino mode and corresponds to $1.25 \cdot 10^{20}$ protons on target (POT) during which both the ArgoNeuT and MINOS near detector were operational. "Antineutrino mode" means that the focusing horn operates in order to focus only negative pions and defocus positive pions. In this configuration only negative pions enter the decay pipe and decay producing negative muons and muon antineutrinos. However, positive pions going along the horn center survive the defocusing action of the horn and enter the decay pipe as well. In general those are high energy pions and when decay they produce positive muons and muon neutrinos. This is the reason why the mean muon neutrinos energy is higher than the mean muon antineutrinos energy. As first step in the analysis a fully automated reconstruction procedure, from hit finding to track reconstruction and calorimetric reconstruction, as described in Section 3.5, is applied to the entire data sample.

Monte Carlo (MC) Simulation

MC simulation is essential for particle physics experiment, and it can be used in many ways, such as estimating the background, studying the signal selection efficiency, deriving systematic uncertainties, just to name a few things. The simulation of neutrino interactions in ArgoNeuT employs a GEANT4-based [87] detector model and particle propagation software in combination with the GENIE neutrino event generator [88]. The propagation of particles in the MINOS near detector is simulated with GEANT3 [89]. A standalone version of MINOS simulation and reconstruction is used to characterize the matching of muon tracks passing from the ArgoNeuT detector into the MINOS near detector. The total size of the sample generated with GENIE is 2997600 events, which corresponds to $45.6048 \cdot 10^{20}$ POT. This sample can be divided into two sub-samples of the size of 1450018 neutrino events and 1489299 antineutrino events. In this analysis the MC sample is properly scaled according to data POT. Besides GENIE (version used: v2.12.2), other neutrino event generators such as NuWro (version used: 17.01.1) [90], GiBUU (version used: 2016) [91] and NEUT (verson used: 5.3.7) [92], are used in order to produce total and differential cross sections expectations and estimate systematic uncertainties from the measurement.

4.2 Event Selection

The processes under study are:

$$\nu_\mu + Ar \rightarrow \mu^- + \pi^\pm + \alpha N$$
$$\overline{\nu}_\mu + Ar \rightarrow \mu^+ + \pi^\pm + \alpha N$$

and require the presence of a muon ($\mu^\pm$) and a charged pion ($\pi^\pm$) plus any number of nucleons (N). Therefore, the final topology selected for this analysis is composed of at least two charged tracks starting at the neutrino interaction vertex. The muon, produced in the neutrino interaction, leaves the ArgoNeuT detector volume and is reconstructed in the MINOS near detector located behind the ArgoNeuT detector. The pion, instead, which less frequently but still more than half of the times leaves the ArgoNeuT TPC fiducial volume, defined with the following coordinates values, x ∈ [3,44] cm; y ∈ [-16,16] cm; z ∈ [6,86] cm, is not reconstructed in the MINOS near detector. For an illustration of the ArgoNeuT detector volume and axes orientations see Figure 4.2.

In order to select events with the required topology a set of selection cuts is
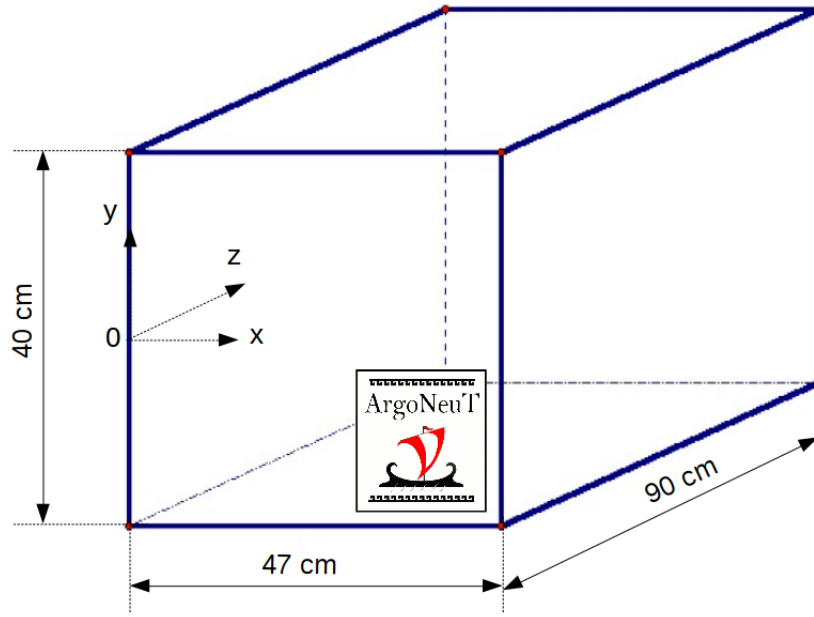
Figure 4.2: ArgoNeuT detector dimensions and axes orientations. The ArgoNeuT TPC fiducial volume is a smaller rectangular prism located within the detector, as described at the beginning of 4.2.

applied, see Section 4.2.1. After the applied cuts, other than signal events, the selected sample includes a contamination of background events, which presents the same topology. The signal and the residual background, are subsequently discriminated with the use of a Multivariate Analysis as described in Section 4.2.6.

4.2.1   Selection Cuts

Throughout the analysis, several parameter distributions are studied and cuts are applied on them. MC simulation have been used to try all possible combinations of cut values and find the one that maximizes the significance of the selection (maximize the signal and minimize the residual background contamination). The reconstruction cuts consist of the following requirements:

- "MINOS match": one track must be matched with a reconstructed track in the MINOS detector in order to identify a neutrino charged-current event. Geometrical cuts on the radial and angular differences between the projection of the ArgoNeuT track in the MINOS detector and the candidate track reconstructed in the MINOS detector must be satisfied. The required radial difference and angular difference must be lower, respectively, than 12 cm and 0.17 rad. If a track fulfills these requirements and a match in the MINOS detector is found, the track takes the name of the "matched track" and the

distance between all the reconstructed vertices and the starting point of this track is calculated. Only the vertex associated with the shortest distance is considered. If the shortest distance is lower than 4 cm and the vertex in enclosed in the ArgoNeuT TPC fiducial volume, the event is kept as a good candidate and the vertex is called the "neutrino interaction vertex", otherwise the event is rejected. Samples of candidate neutrino and antineutrino events are selected based on the charge sign of the muon reconstructed in MINOS.

- "Two tracks": the distance between the neutrino interaction vertex and the starting point of all the reconstructed tracks is measured. All the tracks presenting a distance lower than 4 cm are counted, if a track has its starting point enclosed in a sphere of radius 4 cm centered in the neutrino interaction vertex the track is said to be "in" such vertex. Events with less than two reconstructed tracks in the neutrino interaction vertex are rejected.

- "MIP-like": for each reconstructed track, with the starting point in the neutrino interaction vertex, only the reconstruction, using calorimetric information, on the plane of wires with the higher number of hits for the specific track is considered. For all the tracks reconstructed and labeled as possible MIP-like particles (this means that the track was either reconstructed as a muon or a pion) the length is measured. All the tracks with length equal or higher than 4 cm are counted. The matched track is not considered in this count. Only events with a minimum count of one MIP-like track and a maximum count of two MIP-like tracks are considered. No requirement on the containment in the ArgoNeuT TPC fiducial volume of the the MIP-like tracks is required. For events with only one MIP-like track, the track is taken as the pion candidate. For events with two MIP-like tracks, the one with lower mean dE/dx is taken as the pion candidate.

Recurring to true information in the MC samples it is possible to know how many times the MIP-like track with the lowest mean dE/dx was generated as a pion. After the "Two tracks" cut is applied, this occurs 58% of the times for antineutrino events and only 47% of the times for neutrino events. The remaining times the MIP-like track, reconstructed as a pion, was generated as a proton. Because of the small size of the detector a big percentage of the protons leaves the detector fiducial volume. An exiting proton is very easily identified as a pion since the most relevant part of its track in terms of energy loss, the last part, is not recorded by the detector. Table 4.1 shows the entity of this effect. More than half of the times the protons are not contained in the

detector and at least 70% of these times the protons are identified as MIP-like tracks. For contained protons, instead, the identification is more efficient.

Table 4.1: This table shows the number of times the MC generated protons are reconstructed, with a track length of at least 4 cm, and are contained or not in the detector fiducial volume. From the last two rows it is clear that the separation between protons and pions is much more efficient when the protons is fully contained in the detector.

	ν_μ events [%]	$\overline{\nu}_\mu$ events [%]
Contained	37	43
Not contained	63	57
Contained and reconstructed as MIP-like track	37	31
Not contained and reconstructed as MIP-like track	76	70

The information recorded by the detector is, most of the times, not enough to attempt a separation between protons and pions. The comparison between pions and protons mean dE/dx value is shown in Figure 4.3. This is the reason for the defined cut of two MIP-like tracks in the event. MC Simulations have shown that loosing the "MIP-like" cut up to two candidates, the number of signal events that are considered is higher and the statistic increases. At the same time, of course, additional background events are found in the selected samples. The rejection of the background events relies on the Multivariate Analysis (see Section 4.2.6).

4.2.2   Through-going Muons Cuts

After the "MINOS match" cut but before the "Two tracks" cut a couple of additional cuts are applied in order to remove through-going muons. These particles are muons generated in the interactions of neutrinos from the NuMI beam with the external environment and equipment that surrounds the ArgoNeuT detector. These muons are dangerous for the analysis for two different reasons. First and most important, since they cross the ArgoNeuT detector volume, they are reconstructed in it and are matched in the MINOS detector. Second, due to inefficiency of the cluster and tracking algorithms, the reconstructed track in the ArgoNeuT detector could be broken into different pieces, predominantly two. A broken though-going muon track, assuming it to be divided into two pieces, has a former reconstructed part, the one leaving the ArgoNeuT detector, which could be matched in the MINOS
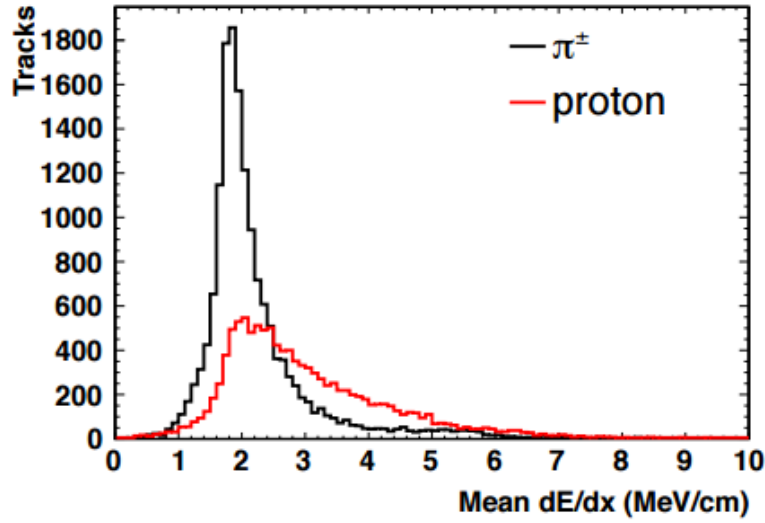
Figure 4.3: Comparison between pion and proton mean dE/dx value in the CC1π events in the ArgoNeuT detector from MC simulation. The distributions have a wide overlap, therefore it is hard to separate protons and pions using the available energy loss information in the detector.

detector and subsequently be labeled as the outgoing muon, and a latter part, the one entering the ArgoNeuT detector, which could be reconstructed as a different MIP-like particle, pointing away from what would be misidentified as the neutrino interaction vertex, the junction point of the two pieces. A lot of work has been done with the cluster and tracking algorithms in order to minimize this effect, however, a sample of these events remained. A classification into two different categories can be done:

- through-going muons entering the ArgoNeuT detector from the frontal surface, the first encountered by the neutrino beam, which are removed using the "Nearestz" cut;

- through-going muons entering the ArgoNeuT detector from the lateral and upper surface, which are removed using the "$\Theta_{\mu\pi}$" cut.

Nearestz Cut

Nearestz cut is used to exclude events where the matched track is a through-going muon entering the detector from the frontal face. For each hit on the collective plane, all the hits on the inductive plane are checked. A couple of hits is formed each time two hits, one per plane, present the same time coordinate. For all the couples formed in the event, the (wire, time) coordinates are converted into three dimensional coordinates, (x, y, z). Only the closest z-value to 0 is then considered

and labeled as "nearestz". Low values of this variable reveal some activity close to the frontal part of the detector which is associated to a through-going muon. The distribution of the nearestz variable is studied and all the events presenting a nearestz value lower than 4 cm are removed. All the other events are considered as good candidates and subsequent reconstruction cuts are later applied. The distribution of the nearestz variable before the cut is applied and banally the distribution of the same variable after the cut is applied can be found in Figure 4.4.
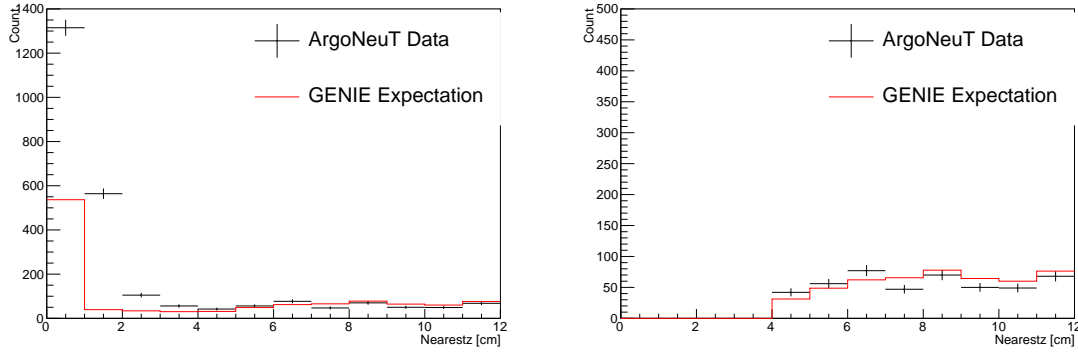
Figure 4.4: (Left) Nearestz variable before the cut is applied, for both data and MC. (Right) Nearestz variable after the cut is applied, the activity close to the frontal face of the TPC is removed.

$\Theta_{\mu\pi}$ Cut

The $\Theta_{\mu\pi}$ cut is used to remove all those events where the matched track is a through-going muon entering the detector from the upper or lateral faces and the reconstructed track results broken into two pieces. The angles between the matched track and all the other reconstructed tracks, with the starting point in the neutrino interaction vertex, are evaluated and only the largest angle, among those evaluated, is considered. It is then checked whether this angle is higher than 170 degrees. If the angle is higher than 170 degrees and the track associated to this angle is not contained in the ArgoNeuT TPC fiducial volume the event is rejected. In all other cases the event is considered as a good candidate and subsequent reconstruction cuts are later applied.

4.2.3   Wrong-Sign Muons

Out of all the muons, whose tracks are reconstructed in the ArgoNeuT detector and matched in the MINOS detector, some of them are reconstructed with the wrong charge sign. This issue occurs because the MINOS reconstruction capability

is not perfect. The entity of this effect has been estimated from the MC samples. After the "MIP-like" cut, in the MC samples, if the muon charge sign reconstructed information and the muon charge sign true information are in disagreement the event is labeled as a wrong-sign event. With the help of true information, all the events in the sample, selected through the selection cuts, that are true signal events, are moved into the true background sample. The percentage of neutrino events moved into the background sample is 6%, while for antineutrino is only 1%. The input variables used in the Multivariate Analysis don't take into account this issue, for this reason, those wrong-sign events, generated as signal and moves in the background sample, have a high probability to end up in the selected region (BDTG ≥ 0) The idea is to remove wrong-sign events generated as signal, when the background template is subtracted from the data sample, see Section 4.3.1.

4.2.4 Pion Threshold

Because of the finite detector resolution, the reconstruction of the particles depends on their kinematic variables. If a particle presents a very low kinetic energy (and momentum), the detector may not be able to reconstruct such particles. A study of the pion reconstruction efficiency has been done from MC simualtions. The detection efficiency is defined as the ratio between the distribution of the true value of a pion variable (momentum) in all true CC 1π events when the pion is reconstructed and the distribution of the same variable in all true CC 1π events, requiring in both cases only the neutrino interaction vertex to be contained in the ArgoNeuT TPC fiducial volume. In this way the numerator results a sub-sample of the denominator. The distribution of the numerator and the denominator in the calculation can be found in Figure 4.5 (top left), while the pion detection efficiency is reported in Figure 4.5 (top right). The efficiency results to be very low below $\sim$100 MeV/c. Results from different MC simulations depend on the detailed modeling of low momentum particles, therefore, it is important to set a threshold on pions information. Imposing the threshold, low momentum particles are removed from both the numerator and denominator, making the result more robust and less MC-dependent. A correlation is noticed between the true pion kinetic energy and the true pion track length (range), shown in Figure 4.5 (bottom). This correlation is used to select the value of the threshold in the pion reconstruction. The thresholds are set at 4 cm for the reconstructed pion track length and 100 MeV/c for the true pion momentum which corresponds to 32 MeV kinetic energy. Pions with true momentum lower than 100 MeV/c are not considered in the pion multiplicity because they would have a reconstructed track length shorter than 4 cm and wouldn't be efficiently reconstructed in

the ArgoNeuT detector. For this reason, in the "MIP-like" cut, the requirement on the MIP-like track length is 4 cm. In principle if a track has a hit on two different wires the algorithm should be able to reconstruct the track. Requiring a length of 4 cm means requiring a track to deposit charge on at least 10 wires which is a relatively long track but as it can be seen in Figure 4.5, the efficiency results very low for shorter tracks.
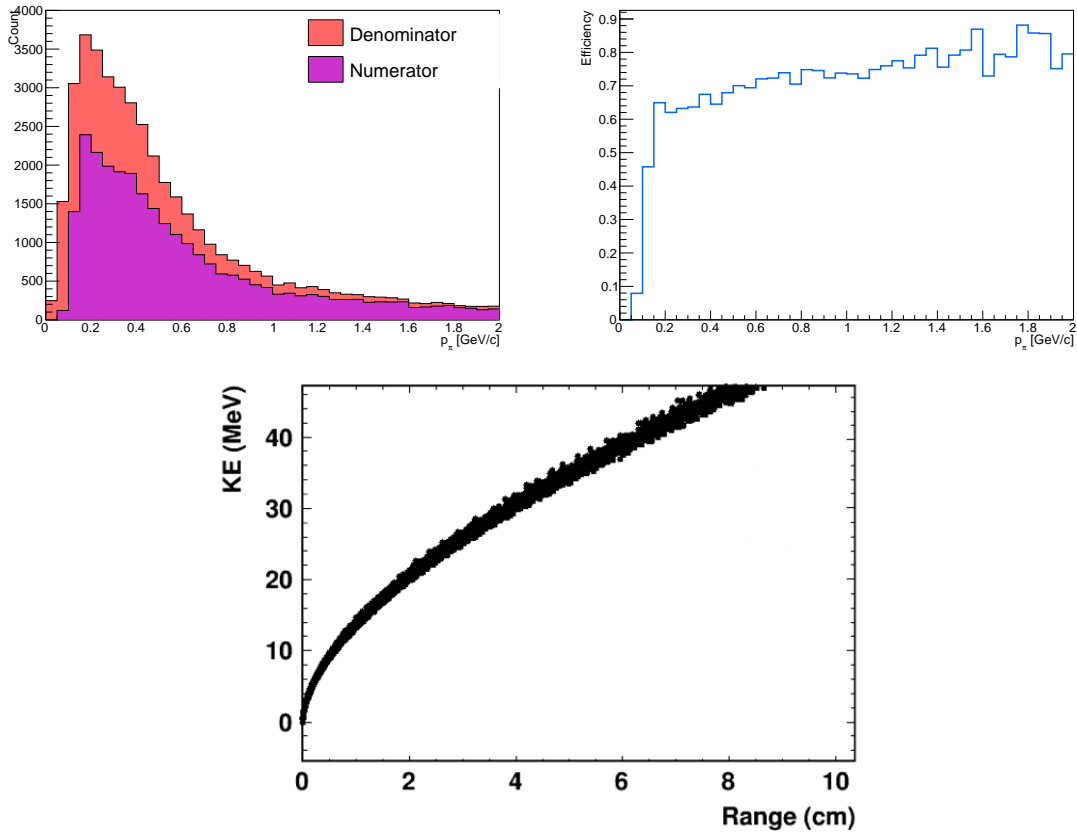
Figure 4.5: Top left: numerator and denominator for the pion detection efficiency calculation are shown. Top right: pion detection efficiency vs pion momentum. Bottom: comparison between the true pion kinetic energy and the true pion track length.

Setting a threshold places a limit in the cross section measurements but is a more preferable way to proceed in the analysis instead of considering all pions, with no limitation on their momentum value, and relying on MC simulation for acceptance correction. The measurement results can eventually be compared with different experimental and theoretical results setting the same thresholds.

4.2.5 Summary of Reconstruction Cuts

The number of selected events of the different selection cuts applied can be found in Table 4.2. The total number of data events passing all the selection cuts is 907 for the neutrino sample and 624 for the anitneutrino sample, as also shown in Table 4.2. Overall, the defined cuts set a very exclusive selection. As a consequence, the total efficiency of the selection in the MC samples is rather low: 20.5% for neutrino events and 18.1% for antineutrino events. This efficiency is defined as the ratio between the number of events selected after the cuts and the number of generated events (CC + NC) presenting the true neutrino interaction vertex inside the TPC fiducial volume.

Table 4.2: Summary table of the event selection for both neutrino and antineutirno samples: cut applied, selected events and rejected events (expressed with Δ) from MC simulations. The number of data events passing the same cuts are also shown in the last row.

	ν_μ		$\overline{\nu}_\mu$	
CC events in TPC	4269		3303	
NC events in TPC	1352		1328	
CC + NC events in TPC	5621		4631	
	Selected Events	Δ	Selected Events	Δ
MINOS match	2621	3000	2587	2044
Nearestz	2219	402	2349	238
$\theta_{\mu\pi}$	2188	31	2331	18
Two tracks	1503	685	1108	1223
MIP-like	1155	348	837	271
Total number of Data events passing cuts	907		624	

4.2.6 Multivariate Analysis

Ideally the signal events would be selected requiring only one MIP-like track starting in the neutrino interaction vertex, other than the matched track. However the ArgoNeuT data are not suitable for that approach because a large number of pions escaping from the ArgoNeuT TPC fiducial volume. For the same reason many protons that are produced in the interactions also escape the fiducial volume. The strategy adopted in the following steps of the analysis is to use reconstructed quantities in the TPC fiducial volume to attempt a classification with multivariate methods

(see below). The ROOT Toolkit for Multivariate Analysis [93] is used to create a Boosted Decision Trees with Gradient (BDTG). The BDTG is trained in order to identify the features of both signal and background and concentrate the classification in one output alone, called the BDTG Classification Value. The classification into signal or background is based on the following input parameters:

- the pion mean stopping power $\langle dE/dx\rangle_\pi$ calculated using only the last 5 cm of the track, when the event presents two MIP-like tracks only the one with the lower value is used as an input parameter;

- the number of reconstructed vertices in each event;

- the number of MIP-like tracks reconstructed at the neutrino interaction vertex, either one or two;

- the ratio between the charge associated to all the reconstructed tracks and the total charge of the event, the charge collected by the plane, measured by the collective plane only, called "Ratio cut1";

- the ratio between the charge associated to the reconstructed tracks starting in the neutrino interaction vertex and the total charge of the event, the charge collected by the plane, measured by the collective plane only, called "Ratio cut2".

MC distributions of all the input parameters used in the Multivariate Analysis training can be found in Figure 4.6 and 4.7.

Note that while for some parameters there is a clear shape difference between signal and background, others don't present it, in this way some parameters are more efficient than others in the discrimination. The result of applying the BDTG classification to neutrino and antineutrino event samples passing the selection cuts is shown in Figure 4.8.

The selected region of the BDTG classification value is defined as the region with the events with an output value ≥ 0. Table 4.3 shows the number of events in the selected regions for data and MC, both signal and background, for neutrino and antineutrino. The Multivariate Analysis presents good results with a MC signal selection efficiency of 78% for neutrino events and 75% for antineutrino events, and a MC background rejection of 69% for neutrino events and 68% for antineutrino events.

An example of neutrino event with a BDTG value ≥ 0.8 is shown is Figure 4.9.
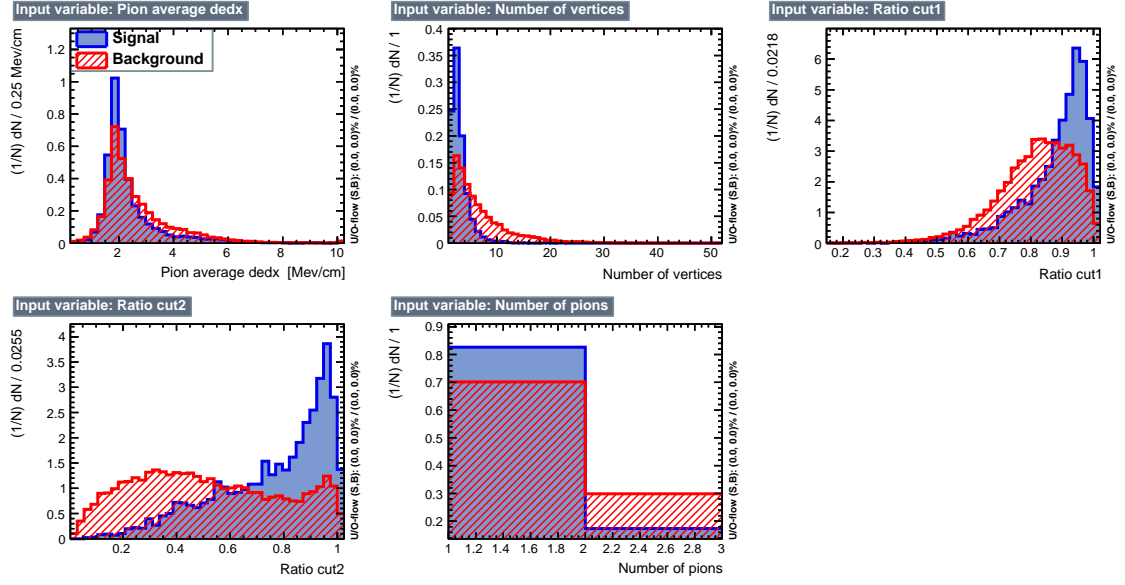
Figure 4.6: Comparison between signal and background input variables used in the neutrino training sample.
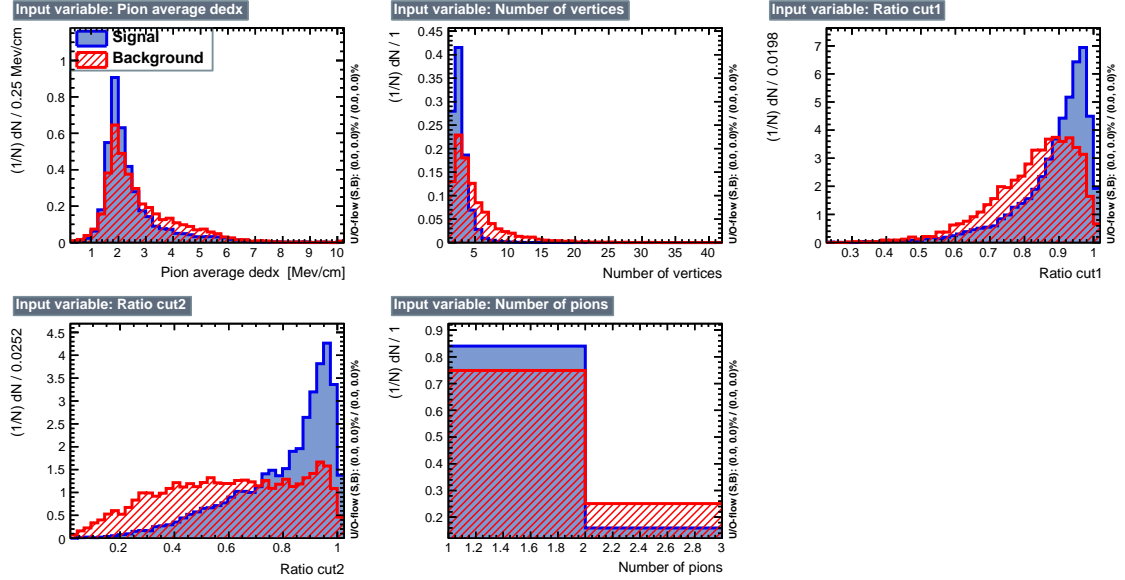
Figure 4.7: Comparison between signal and background input variables used in the antineutrino training sample.

Figure 4.8: Top: BDTG classification results for the neutrino sample, MC signal, MC background and data are shown. Bottom: BDTG classification results for the antineutrino sample, MC signal, MC background and data are shown.
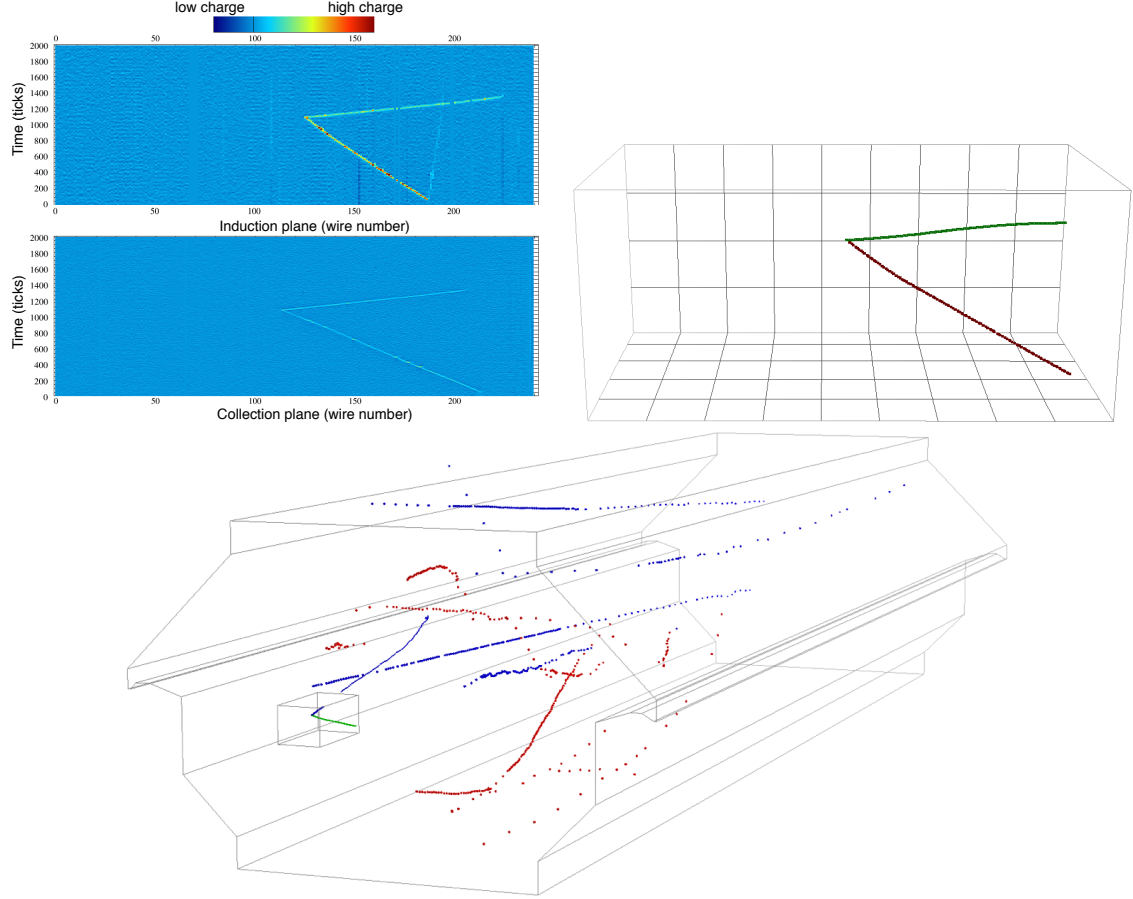
Figure 4.9: Top left: CC1π candidate event display on both wire planes (induction plane on top and collection plane on bottom). Top right: 3D reconstruction of the event, the green track is the muon, the red track is the pion. Bottom: the ArgoNeuT and MINOS detectors are shown in this view, the ArgoNeuT detector is the small box in front, where the muon and pion are created in the neutrino interaction, while the MINOS detector is the big exagonal prism in the back. It is possible to connect, visually, the blue track in the ArgoNeuT detector with the blue track in the MINOS detector pointing toward the upper face. Dispaly of the event 2512 run 722, BDTG = 0.81.

Table 4.3: Summary table of the Multivariate Analysis results choosing a selection region for events with BDTG value ≥ 0.

	ν_μ				$\overline{\nu}_\mu$			
	Data	MC Total	MC (Sig)	MC (Back)	Data	MC Total	MC (Sig)	MC (Back)
Total (after cuts)	907	1155	231	924	624	837	375	462
Selected Region	340	464	180	284	286	429	283	146
Rejected	567	691	51	640	338	408	92	316

Multivariate Algorithm

One of the most efficient ways to separate signal from background, when the separation can't be done by cutting on specific parameters, is a Multivariate Analysis. When tagged samples of background and signal events are available, it is possible to build a classifier to separate signal and background events [94]. The MC samples are used as tagged samples and have to be divided into two parts to train and test the algorithm. This can be done, for example, splitting randomly the samples in halves. The first part is used to train the classifier, the second part is used to verify that the training has been correctly performed without introducing any dependence on the set of events used (over-training). In this analysis the splitting mode is chosen to be random. The samples used in the training step have the sizes of 3369 events for the neutrino signal sample, 13329 events for neutrino background sample, 6627 events for the antineutrino signal sample and 7921 events for the antineutrino background sample (the sizes of these samples are not normalized to data POT but are counted according to the MC $45.6048 \cdot 10^{20}$ POT). The testing samples have the same sizes of the training samples. The neutrino background samples size is approximately 4 times bigger than the neutrino signal sample size, for this reason a weight of 0.25 is applied on the neutrino background events in the training process. Since in the antineutrino case the two samples, signal and background, are similar no additional weight is applied. In the BDTG method, the input parameters are used to split the training data sample as follows:

- for each variable, a splitting value which provides the best separation between signal and the background is found;

- the variable with the splitting value which provides the best signal to background separation is selected;

- using this variable as discriminating variable, the initial sample of events is split in two samples called "branches" and the process is repeated.

The splitting keeps going on until a given number of final branches ("leaves") is reached and a decision tree is completed. If most of the events ending on a leaf are signal events, the leaf is tagged as signal leaf, otherwise it is tagged as background leaf. The classification provided by one decision tree alone is very sensitive to statistical fluctuations on the training data. This is overcome by the use of Boosting. A Boosted Decision Tree combines the prediction of many decision trees to deliver a more robust classification. The boosting extends the single tree approach to a combination of several trees ("forest"). All the trees are derived from the same training sample: events most often misclassified in the previous trees receive a higher weight to force the next trees to give them the correct tag. Typically, at least 1000/2000 trees are built in this way to make the training sample stable. When the forest is complete, a score (BDTG value) is assigned to each event. For each tree, the event follows the decision path: if it ends on a signal leaf it receives a score of 1, if it ends on a background leaf it receives a score of -1. The finale score is the average of the scores of all the trees. High scores mean the event is most likely signal while low scores that it is most likely background. The same set of decision trees is used to classify the background and the signal events in the test sample. By choosing a particular BDTG value on which to cut, it is possible to select a desired ratio of signal to background. For this analysis the chosen value is 0. The distribution of the BDTG scores for the neutrino and antineutrino signal and background samples are shown in Figure 4.8.

4.3 Extraction of the Signal

After the requirement on the BDTG value, the two selected data samples, neutrino and antineutrino, still contain a sub-sample of background events each. A MC background sample that passed the same cuts is used as estimator of the background contamination and subtracted to data in order to extract the signal. The extraction of the signal is done for four different kinematic variables distributions: the outgoing muon momentum (p_μ), the outgoing muon angle with respect to the initial neutrino direction (θ_μ), the outgoing pion angle with respect to the initial neutrino direction (θ_π) and the angle between the outgoing muon and pion ($\theta_{\mu\pi}$). An interesting fact, following the comparison in Figure 4.8, is that the GENIE MC generator seems to reproduce well the shapes of the distributions but overestimates the overall normalizations. While this was previously evident comparing the total number of events passing the cuts in Table 4.2, the GENIE overestimating behavior is not new in the neutrino physics community. As an example, results from the measurement of

the muon neutrino CC single pion production cross section on water with the T2K near detector report an overextimation of the GENIE expectations as well [95]. The MC samples are scaled, signal and background together, with the final goal to make them fit the data BDTG value distribution.

4.3.1   Scaling of the MC Samples to Data

In order to normalize the MC distributions, the ROOT fitting class TFractionFitter [96] is used. The unique feature of TFractionFitter is that it deals with the statistical fluctuations of the templates. The templates can move, within their errors, to improve the fit. The scaling is thought with two different constants related to each other, "α" and "$\beta = 1-\alpha$", which are used to normalize, respectively, the MC signal and background distributions. The results of the fits are shown in Figure 4.10 and the number of events after the normalization procedure are reported in Table 4.4.

After the fits, the normalization of the events presented in Table 4.3 can be found in Table 4.4.

Table 4.4: As Table 4.3, after the normalization procedure (see Section 4.3.1.

	ν_μ				$\overline{\nu}_\mu$			
	Data	MC Total	MC (Sig)	MC (Back)	Data	MC Total	MC (Sig)	MC (Back)
Total (after cuts)	907	907	160	747	624	624	218	406
Selected Region	340	348	125	223	286	290	165	125
Rejected	567	559	35	524	338	334	53	281

4.3.2   Subtraction of the Background

The MC background distributions obtained cutting on the BDTG parameter, after further normalization (described in the previous Section 4.3.1), are used as estimators of the background contamination in the data distributions. A bin by bin subtraction is executed between the data distribution and the MC background distribution for both cases, neutrino and antineutrino. The resulting distributions, and the comparisons with the normalized MC signal samples are shown in Figure 4.11 and 4.12.
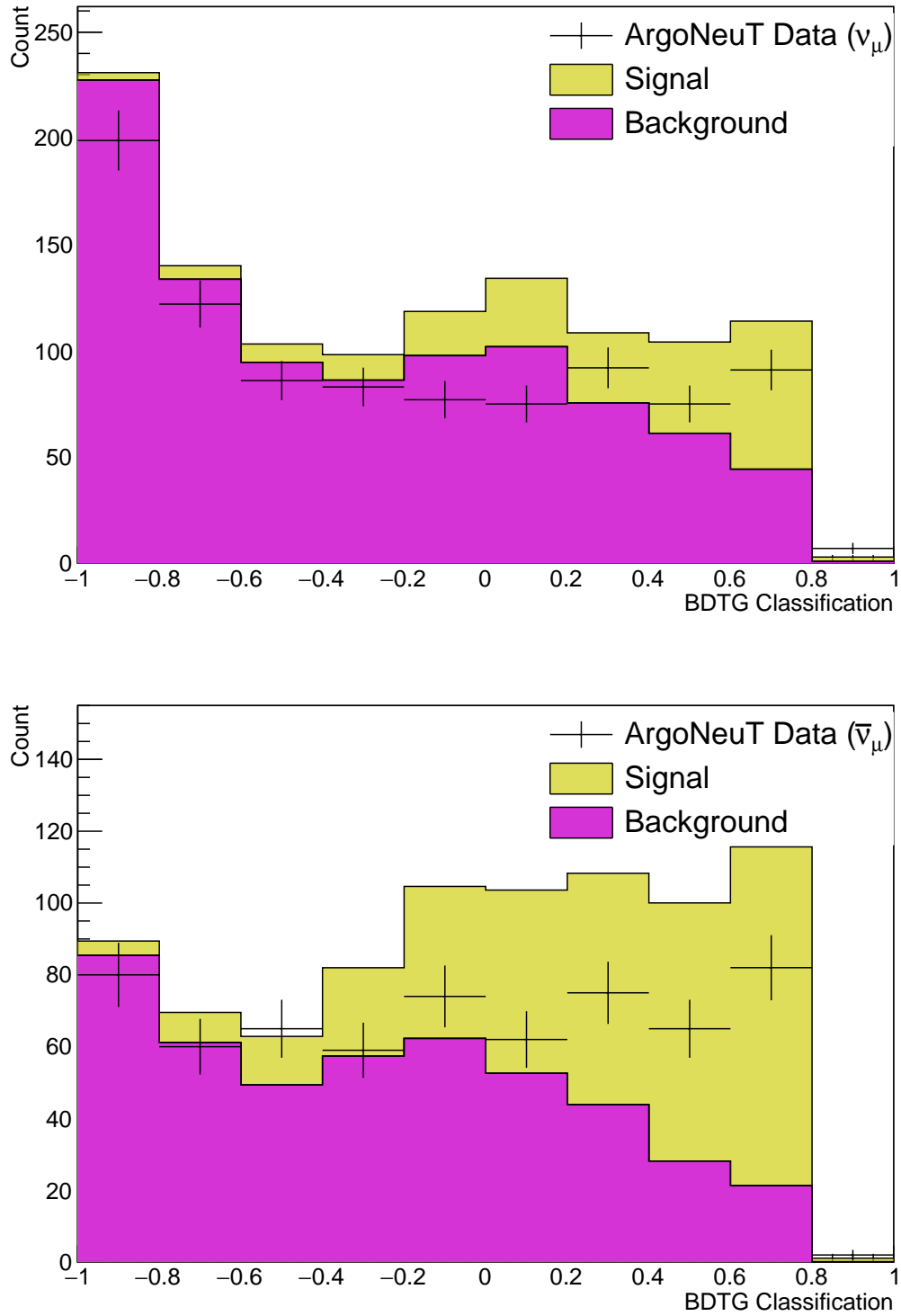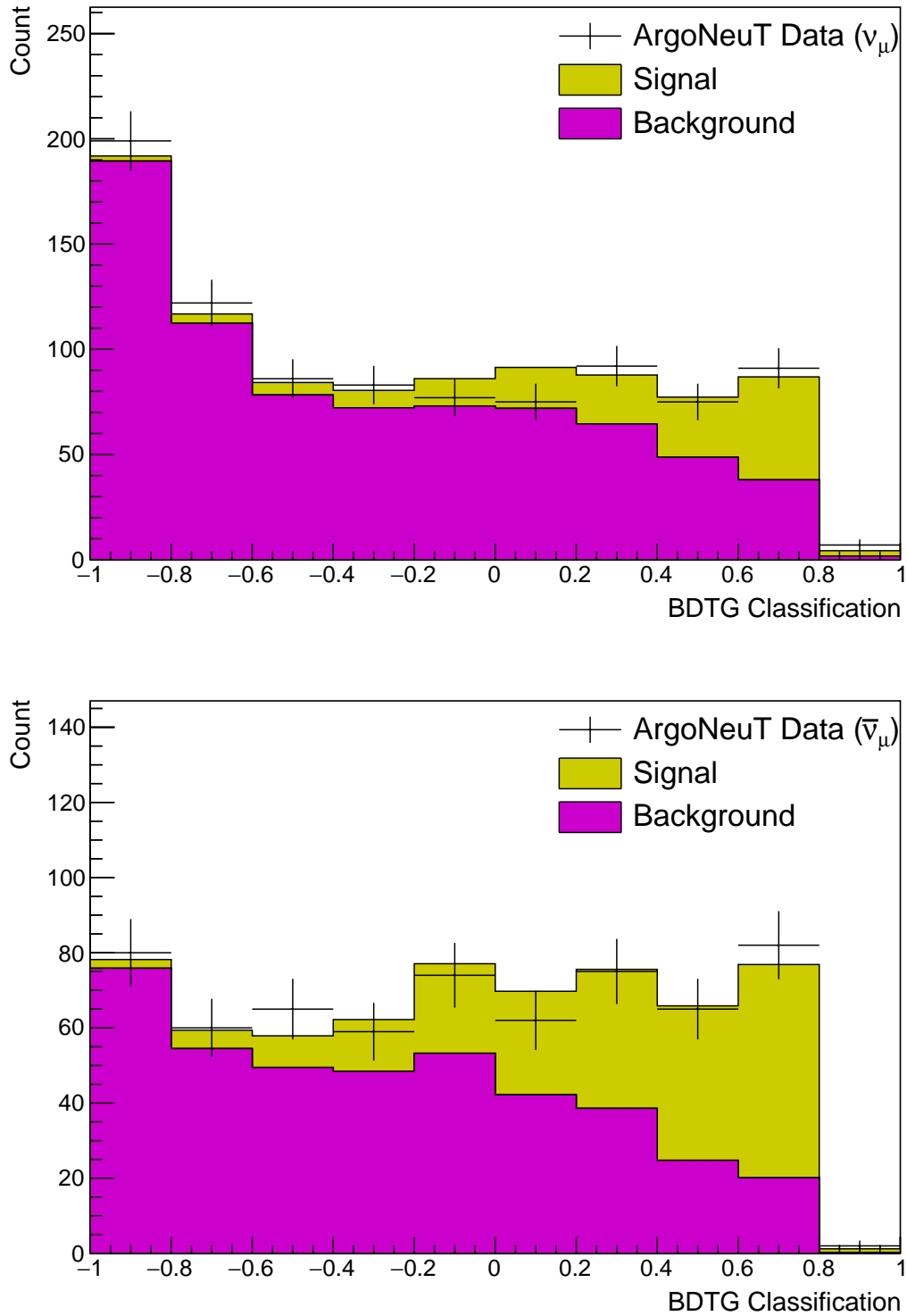
Figure 4.10: Top: BDTG classification results for the neutrino sample after the scaling, MC signal, MC background and data are shown. Bottom: BDTG classification results for the antineutrino sample after the scaling, MC signal, MC background and data are shown.
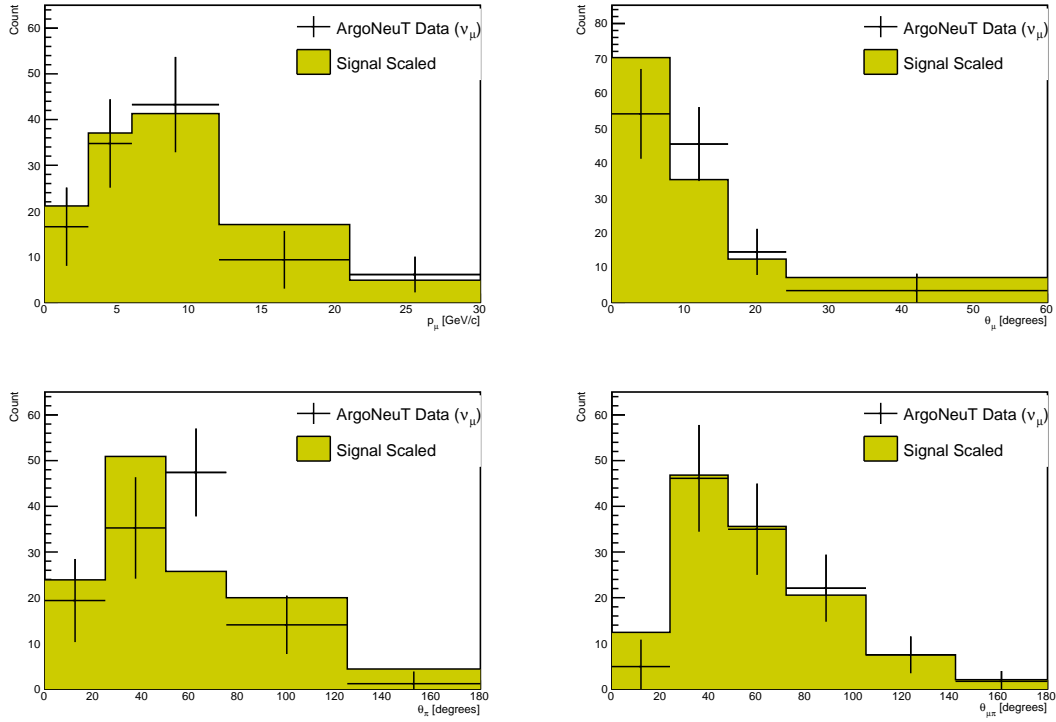
Figure 4.11: Extracted signal distributions after subtracting background from data for muon neutrino events. The distributions are compared to the normalized MC signal distributions. Clockwise starting in the top left corner: outgoing muon momentum distribution (p_μ), outgoing muon angle with respect to the initial neutrino direction distribution (θ_μ), outgoing pion angle with respect to the initial neutrino direction distribution (θ_π) and distribution of the angle between the outgoing muon and pion ($\theta_{\mu\pi}$).
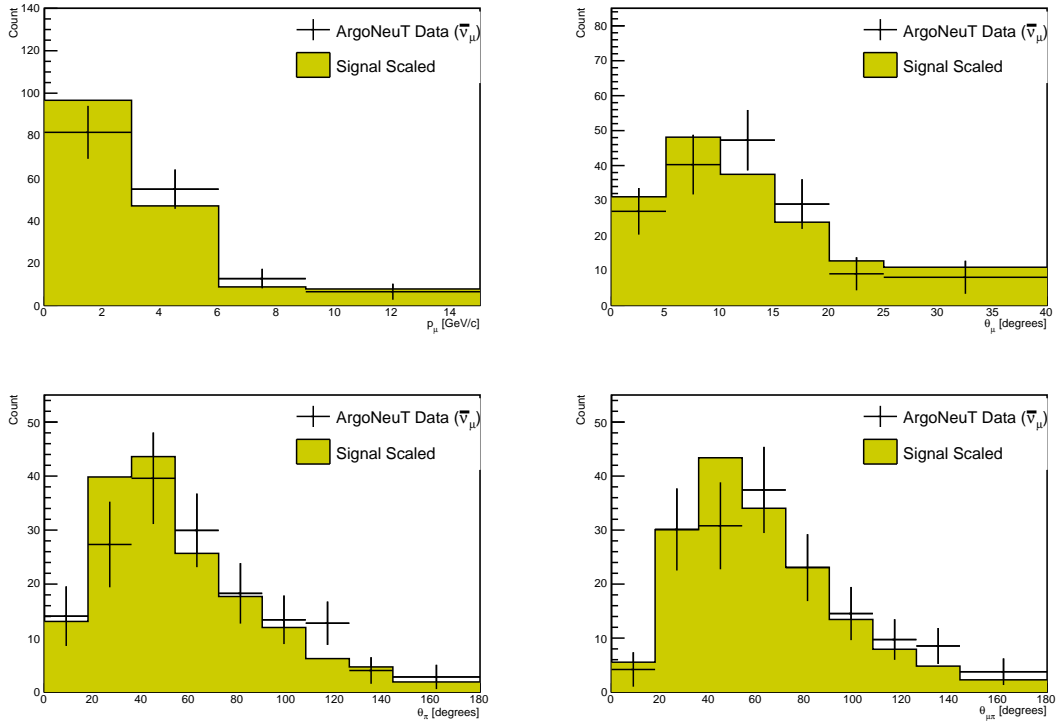
Figure 4.12: Extracted signal distributions after subtracting background from data for muon antineutrino events. The distributions are compared to the normalized MC signal distributions. Clockwise starting in the top left corner: outgoing muon momentum distribution (p_μ), outgoing muon angle with respect to the initial neutrino direction distribution (θ_μ), outgoing pion angle with respect to the initial neutrino direction distribution (θ_π) and distribution of the angle between the outgoing muon and pion ($\theta_{\mu\pi}$).

4.4   Systematic Uncertainties

The ArgoNeuT CC 1 pion muon neutrino cross section measurement is statistically limited. Nevertheless a careful study of systematic uncertainties has been performed. Several sources of systematic uncertainty affecting this cross section measurement have been considered. The estimation of the uncertainty associated with some sources of systematic error, for example flux normalization and POT, has already been performed in previous ArgoNeuT and MINOS analyses [97], [65]. The next paragraphs summarize how other sources are evaluated and their final impact on the cross section measurements.

4.4.1   GENIE Systematic Uncertainty Sources

In the process to produce the final results, expectations are involved, which are known to be imperfect and strictly dependent on the model used by the simulator. The estimated uncertainties on the various modeling contributions, give rise to the systematic errors. The systematic errors are evaluated by applying a procedure known as the many universes. For a given systematic source, the relevant model parameters are shifted within their measured $\pm 1\sigma$ uncertainties. The measured observable is then re-extracted with the complete analysis procedure using the shifted parameters. This variation is commonly referred to as an universe, which represents the deviation from the measured nominal value. In the last step of this procedure the variations from the up-shifted and down-shifted parameter are checked. If both present the same effect, both a negative variation or a positive variation, the higher, taking the absolute values, is considered with the respective sign while the other one is set to 0. On the other hand, if the two variations have different sign, the positive variation is used in the estimation of the positive systematic uncertainty while the negative is used in the negative one. Since GENIE is used to simulate the neutrino interactions observed in the ArgoNeuT detector, the total and differential cross section measurement are sensitive to GENIE models, because of their reliance on GENIE for the background subtraction 4.3.2 and efficiency correction 4.5.3. Therefore, GENIE modeling of the signal and background, as well as the hadron transportation through the nucleus all contribute to the systematic uncertainty on the measured cross section. Important systematics, for neutrino interactions in the few-GeV energy range, include the axial mass for CCQE scattering (Qema) and the axial and vector masses for both CC and NC resonance neutrino production (CcresAxial, CcresVector). Charged-current and neutral-current coherent pion production uncertainties are taken into account by modifying the corresponding axial mass (CohMA)

and the nuclear size parameter "R_0", which controls the pion absorption factor in the Rein-Sehgal model (CohR0). Uncertainties in the level of the non-resonance background are considered for all neutrino charged-current and neutral-current 1π and 2π production channels (NonResRvbarp1pi, NonResRvbarp2pi, NonResRvp1pi, NonResRvp2pi). Only a source of uncertainty in the in-medium modifications of the hadronization process (FormZone) is considered. Finally, an uncertainty affecting the intranuclear hadron transport model; uncertainty in the absorption of hadrons within the target nucleus (IntraNukePlabs). A summary of the parameters used in this analysis can be found in Table 4.5 where the $\pm 1\sigma$ variation is also shown. For the complete list of the GENIE neutrino interaction cross section systematic parameters see [98].

Table 4.5: Neutrino interaction cross section systematic parameters considered in this anaysis for GENIE, the $\pm 1\sigma$ variation is shown in the last column. The complete list, including also sources not used in this analysis, can be found in [98].

Variable	Description	Variation
Qema	Axial mass for CCQE	$^{+25\%}_{-15\%}$
CcresAxial	Axial mass for CC resonance neutrino production	$\pm 20\%$
CcresVector	Vector mass for CC resonance neutrino production	$\pm 10\%$
CohMA	Axial mass for CC and NC coherent pion production	$\pm 50\%$
CohR0	Nuclear size parameter controlling pion absorption in Rein-Sehgal model	$\pm 10\%$
NonResRvbarp1pi	Non-resonance background in CC ν+n and $\overline{\nu}$+p (1π) reactions	$\pm 50\%$
NonResRvbarp2pi	Non-resonance background in CC ν+n and $\overline{\nu}$+p (2π) reactions	$\pm 50\%$
NonResRvp1pi	Non-resonance background in CC ν+p and $\overline{\nu}$+n (1π) reactions	$\pm 50\%$
NonResRvp2pi	Non-resonance background in CC ν+p and $\overline{\nu}$+n (2π) reactions	$\pm 50\%$
FormZone	Hadron formation zone	$\pm 50\%$
IntraNukePlabs	Pion absorption probability	$\pm 20\%$

4.4.2 Other Systematic Uncertainty Sources

Other sources, which contribute to the total systematic uncertainty, include the following:

Calorimetry Constant

In the last part of this analysis the calorimetry constant was checked and tuned to its final value (see Section 3.5.4). After the ultimate tuning, the final cross section values were observed to slightly change, for this reason a conservative variation of $\pm 3\%$ on the calorimetry constant is assumed and the final effect on the measured quantities is considered as a systematic uncertainty.

POT and Flux Normalization

The POT and flux normalization systematic errors (1% and 11% respectively [97]) only affect the final cross section calculation after the signal sample is estimated, see Section 4.3.

Fiducial Volume - Number of Argon Targets in TPC

The uncertainty on the number of argon targets originates from the uncertainty on determining the active volume [65]. The uncertainty on the Y and Z dimensions, measured using the crossing positions of the wires is of 1 mm; the X dimension is obtained from the electron drift-time and presents an uncertainty of approximately 1 cm. Combined, these lead to an uncertainty on the number of argon targets of approximately 2%. As well as the POT and flux normalization, the number of targets only affect the final cross section calculation in the last step of the measurement. An error of 2% is assigned to the number of argon targets in the fiducial volume, taking into account eventual uncertainties associated with the density of the liquid argon.

4.4.3   Summary of Systematic Uncertainties

All the considered systematic uncertainty sources are summarized in Table 4.6, with their fractional cross section uncertainty.

The neutrino measurement results more sensitive to the systematic uncertainty sources. A plausible explanation is that in this analysis, neutrinos have a mean energy higher than antineutrinos, higher energy means higher probability to create pions in the interaction and for this reason the neutrino sample is contaminated with more background events. The background events are mainly DIS events and the fact of relying on the MC generator to estimate the background distribution makes the final cross section measurement more dependent on MC variations. Among all the systematic uncertainty sources, the flux normalization plays the role of the leading one in this analysis for both, neutrino and antineutrino results.

Table 4.6: List of systematic errors affecting this analysis and their estimation.

Systematic Uncertainty	Fractional cross section uncertainty [%]	
	ν_μ	$\overline{\nu}_\mu$
Qema	$+2.4$ -6.8	$+0.5$ -1.2
CcresAxial	$+6.8$ -8.0	$+2.4$ -1.7
CcresVector	$+2.8$ -4.0	$+1.0$ -1.1
CohMA	$+0.8$ -0	$+0.9$ -0
CohR0	$+0.8$ -0	$+0.9$ -0
NonResRvbarp1pi	$+8.4$ -7.6	$+1.0$ -1.2
NonResRvbarp2pi	± 2.0	$+0.7$ -0.9
NonResRvp1pi	$+0.4$ -0.8	$+0.9$ -1.0
NonResRvp2pi	± 2.0	$+0.7$ -0.9
FormZone	$+8.8$ -0	$+0.9$ -0.5
IntraNukePlabs	± 2.4	$+0.2$ -0.4
CalorimetryConstant	$+4.8$ -0	$+4.2$ -4.7
POT	± 1.0	± 1.0
Flux Normalization	$+10.0$ -12.0	$+10.0$ -12.0
Number of Argon Targets	± 2.0	± 2.0
Total systematics	$+18.7$ -18.6	$+11.6$ -13.4

4.5   Cross Section Calculation

The flux-integrated total cross section is given by

$$\langle\sigma\rangle = \frac{N}{\epsilon \; N_{Ar} \; \int \phi dE}$$

where N is the data yield after background subtraction (see Section 4.3.2), N_{Ar} represents the number of target nuclei in the detector fiducial volume (see Section 4.5.2), ϵ is the efficiency of the event selection and reconstruction (see Section 4.5.3) and $\int \phi dE$ is the integrated neutrino flux (see Section 4.5.1).

4.5.1   Integrated Flux

The neutrino and antineutrino flux estimations for the antineutrino-enhanced run are shown in Figure 4.13. These are integrated and converted to the total number of POT for the 6 month run, which corresponds to $1.25 \cdot 10^{20}$ POT, giving:

$$\int \Phi_{\bar{\nu}_\mu} = 3.063 \cdot 10^{12} \; cm^{-2}$$

$$\int \Phi_{\nu_\mu} = 6.834 \cdot 10^{11} \; cm^{-2}$$
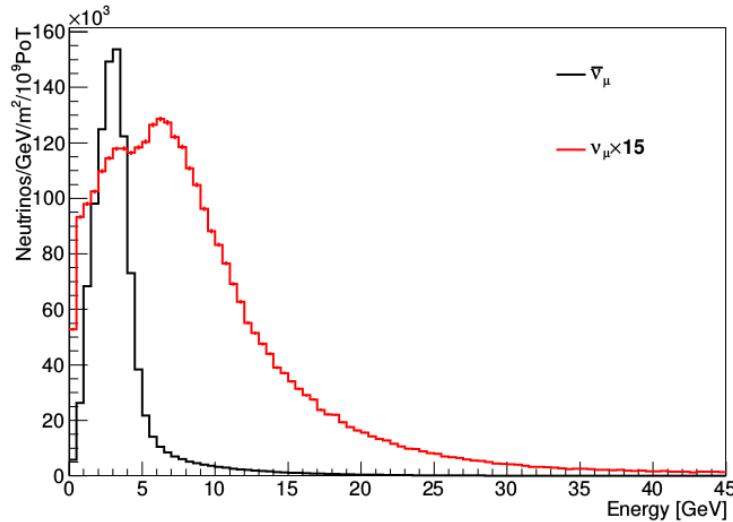
Figure 4.13: Estimated neutrino and antineutrino flux for the antineutrino-enhanced run.

4.5.2 Number of Target Nuclei in ArgoNeuT (N_{Ar})

The number of argon nuclei in the fiducial volume (V = 41 cm x 32 cm x 80 cm = 104.96 dm^3) is given by:

$$N_{Ar} = n \ N_{Avogadro} = \frac{V \cdot d}{M_{Ar}} N_{Avogadro}$$

$$= 2.215 \cdot 10^{27} \text{ nuclei}$$

where n is the number of moles calculated from the density (d = 1.4 $\frac{kg}{dm^3}$) and the molar mass M_{Ar} = 0.039948 $\frac{kg}{mol}$. Using the number of target nuclei and the integrated fluxes, the cross sections can be written as a function of the number of signal events scaled by the efficiency:

$$\langle \sigma_{\bar{\nu}_\mu} \rangle = \frac{N}{\epsilon} \cdot 1.475 \cdot 10^{-40} \ cm^2$$

$$\langle \sigma_{\nu_\mu} \rangle = \frac{N}{\epsilon} \cdot 0.661 \cdot 10^{-39} \ cm^2$$

4.5.3 Efficiency Correction

An efficiency correction is required in order to calculate the cross section. It is calculated from MC simulation and is defined as the ratio between the reconstructed kinematic variable distribution for true signal events passing the selection cuts and the true kinematic variable distribution for true signal events generated in the detector fiducial volume. Using reconstructed information in the numerator and true information in the denominator, the process is able to take into account and correct for detector smearing. Eight efficiencies are calculated, four for neutrino and four for antineutrino events, one for each kinematic variable listed in 4.1 ($p_\mu, \theta_\mu, \theta_\pi, \theta_{\mu\pi}$). Efficiencies are shown in Figure 4.14 and 4.15, while efficiency-corrected distributions are shown in 4.16 and 4.17. The efficiency corrections are performed bin by bin, dividing the extracted data distribution by the efficiency distribution. Efficiency corrected distributions for data and GENIE MC events are reported in Figure 4.16 and 4.17 for ν_μ and $\bar{\nu}_\mu$ respectively. An interesting feature to notice is that the GENIE MC predictions don't describe the ArgoNeuT data well.

4.5.4 Differential Cross Sections

In order to calculate the differential cross sections, after dividing the extracted signal distributions by the number of targets in the detector, the integrated flux and
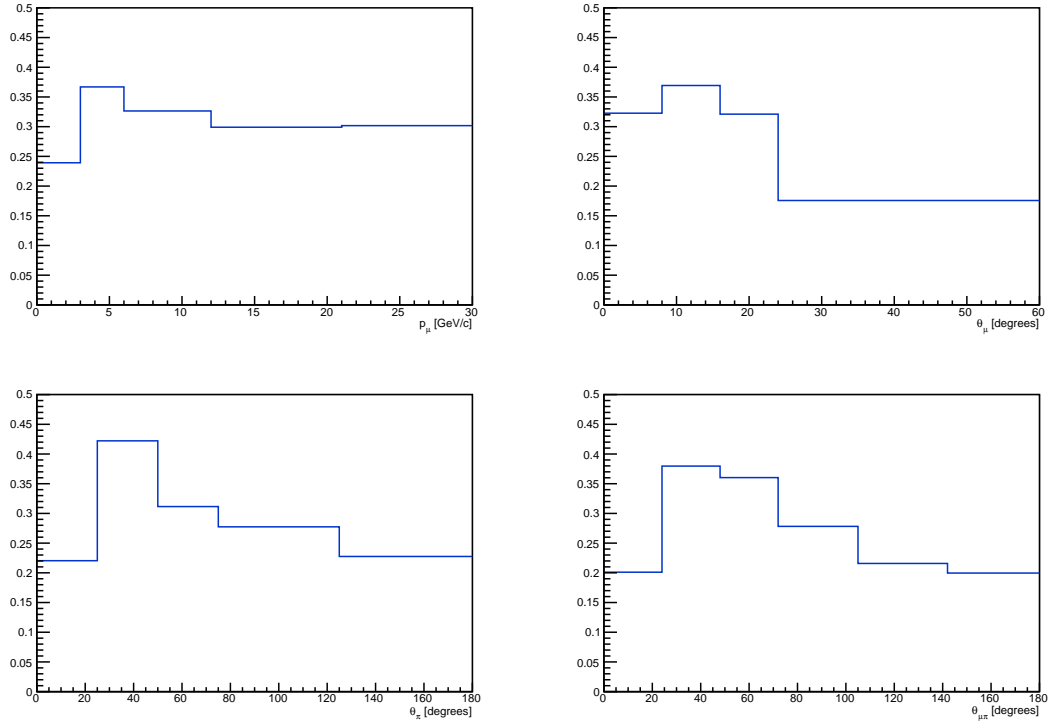
Figure 4.14: Efficiency distributions for neutrino events. Clockwise starting in the top left corner: outgoing muon momentum distribution (p_μ), outgoing muon angle with respect to the initial neutrino direction distribution (θ_μ), outgoing pion angle with respect to the initial neutrino direction distribution (θ_π) and distribution of the angle between the outgoing muon and pion ($\theta_{\mu\pi}$).
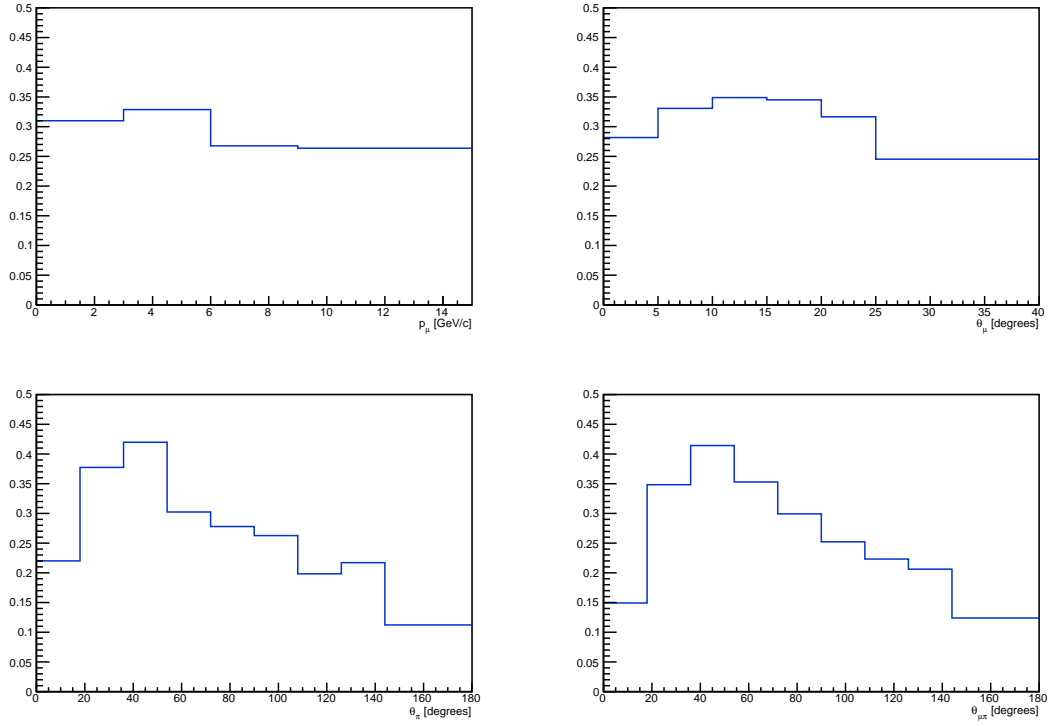
Figure 4.15: Efficiency distributions for antineutrino events. Clockwise starting in the top left corner: outgoing muon momentum distribution (p_μ), outgoing muon angle with respect to the initial neutrino direction distribution (θ_μ), outgoing pion angle with respect to the initial neutrino direction distribution (θ_π) and distribution of the angle between the outgoing muon and pion ($\theta_{\mu\pi}$).
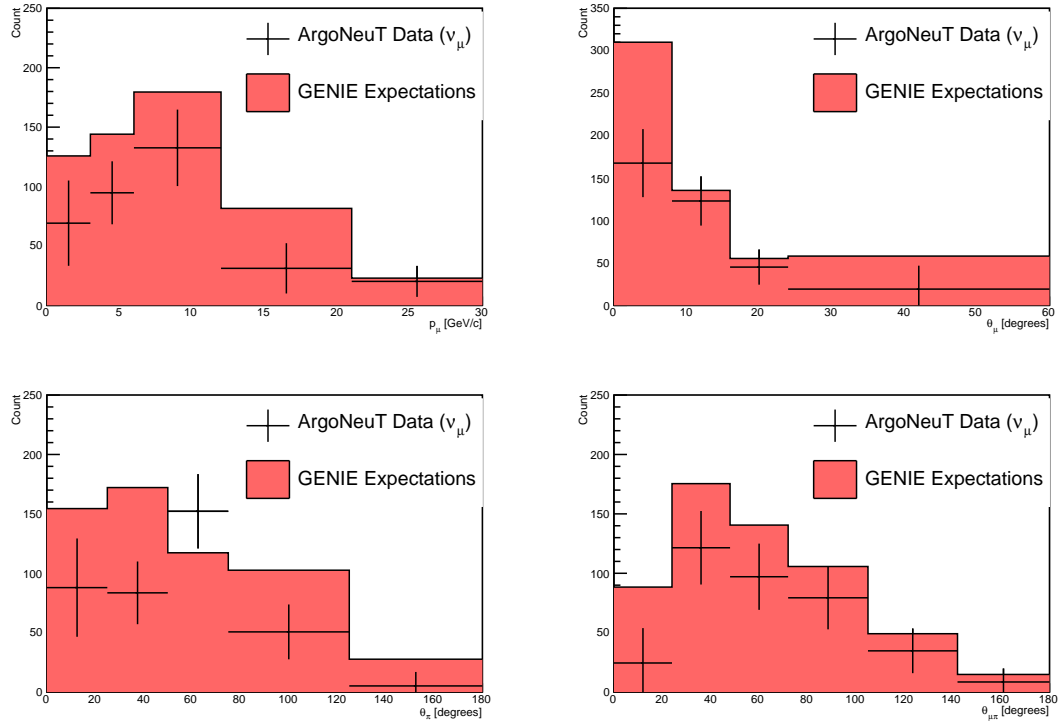
Figure 4.16: Comparison between the extracted signal sample, corrected by efficiency, and the MC true signal events generated in the detector fiducial volume for the neutrino analysis. Clockwise starting in the top left corner: outgoing muon momentum distribution (p_μ), outgoing muon angle with respect to the initial neutrino direction distribution (θ_μ), outgoing pion angle with respect to the initial neutrino direction distribution (θ_π) and distribution of the angle between the outgoing muon and pion ($\theta_{\mu\pi}$).
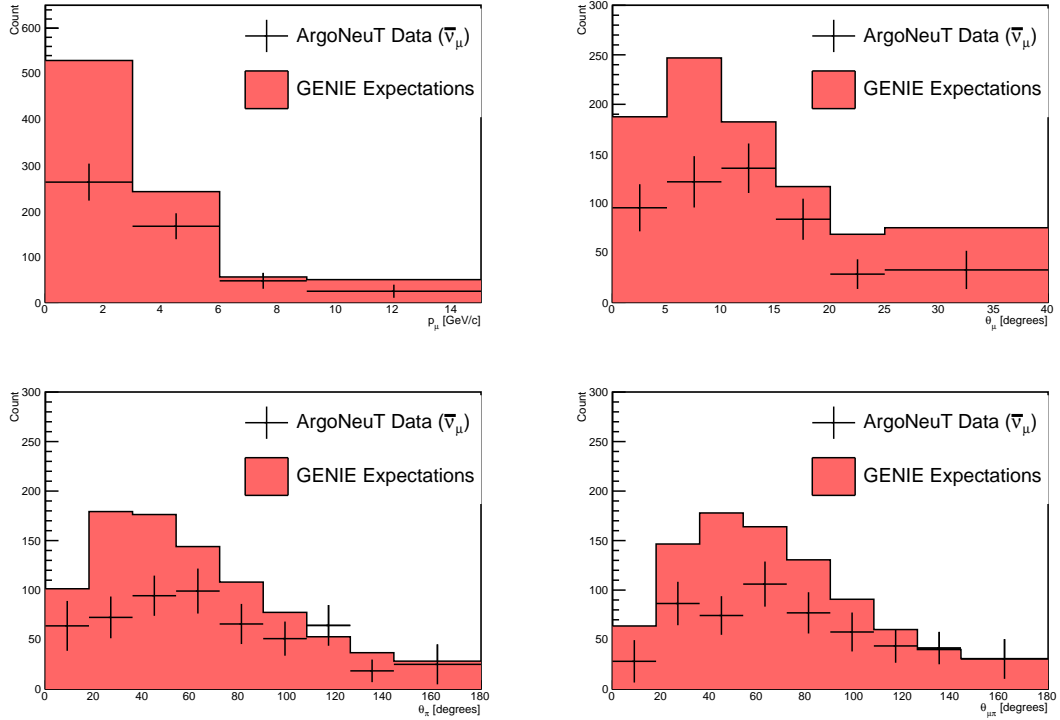
Figure 4.17: Comparison between the extracted signal sample, corrected by efficiency, and the MC true signal events generated in the detector fiducial volume for the antineutrino analysis. Clockwise starting in the top left corner: outgoing muon momentum distribution (p_μ), outgoing muon angle with respect to the initial neutrino direction distribution (θ_μ), outgoing pion angle with respect to the initial neutrino direction distribution (θ_π) and distribution of the angle between the outgoing muon and pion $(\theta_{\mu\pi})$.

the efficiency, each bin is divided by its width and by the argon mass number. Expectations are calculated using also three different MC generators, NuWro, GiBUU and NEUT. Results for the differential cross sections are shown is Figure 4.18 and 4.19 and tabulated in Table 4.7 and 4.8. Among the three MC generators, GiBUU better describes the ArgoNeuT CC 1 pion muon neutrino data and in particular the antineutrino data, while NuWro, NEUT and especially GENIE predictions substantially overestimate data.
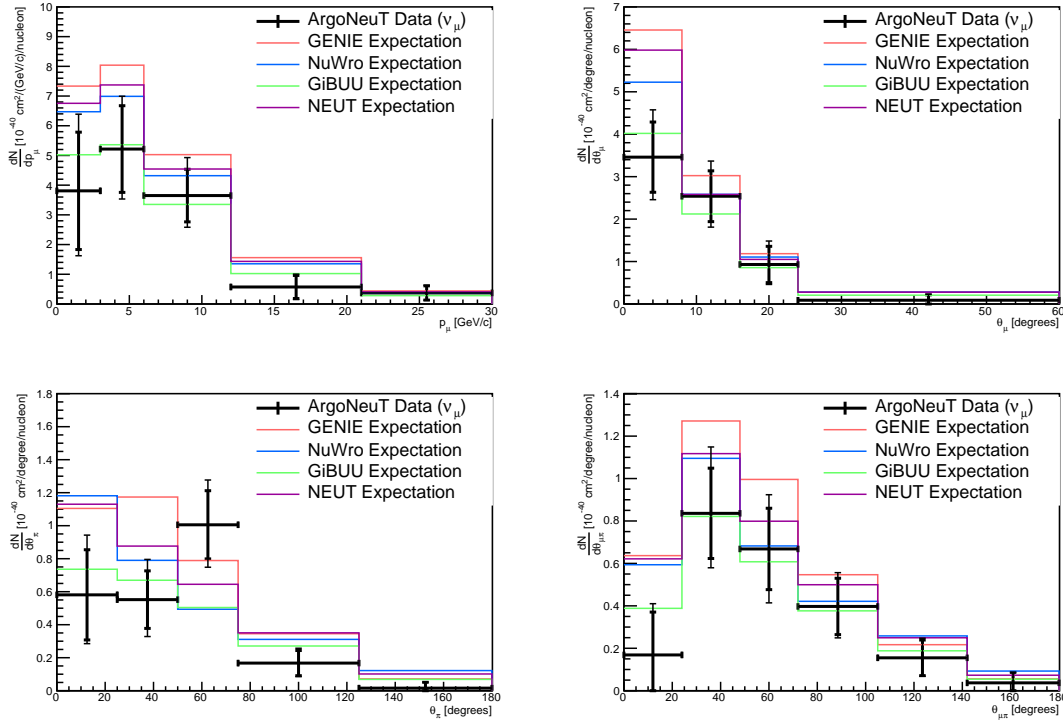
Figure 4.18: ArgoNeuT muon neutrino CC 1 pion differential cross sections compared to GENIE, NuWro, GiBUU and NEUT. Clockwise starting in the top left corner: outgoing muon momentum distribution (p_μ), outgoing muon angle with respect to the initial neutrino direction distribution (θ_μ), outgoing pion angle with respect to the initial neutrino direction distribution (θ_π) and distribution of the angle between the outgoing muon and pion ($\theta_{\mu\pi}$).

4.5.5   Total Cross Sections

Using the best signal estimation and the constants defined in the previous paragraphs the flux-averaged cross sections for this analysis are found to be:

$$\langle \sigma_{\nu_\mu} \rangle_{CC1\pi} = 2.5 \pm 0.4(stat) \pm 0.5(syst) \times 10^{-37} cm^2/Ar \text{ at } \langle E_{\nu_\mu} \rangle = 9.6 \text{ GeV}$$

$$\langle \sigma_{\bar{\nu}_\mu} \rangle_{CC1\pi} = 8.2 \pm 0.9(stat)^{+0.9}_{-1.1}(syst) \times 10^{-38} cm^2/Ar \text{ at } \langle E_{\bar{\nu}_\mu} \rangle = 3.6 \text{ GeV}$$
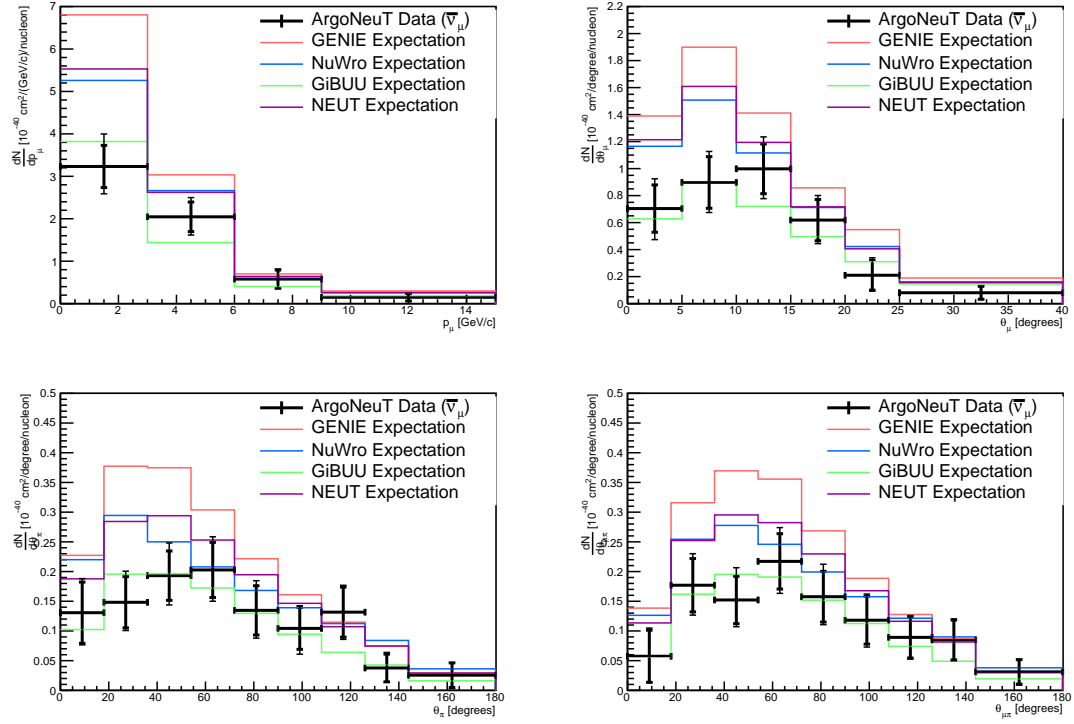
Figure 4.19: ArgoNeuT muon antineutrino CC 1 pion differential cross sections compared to GENIE, NuWro, GiBUU and NEUT. Clockwise starting in the top left corner: outgoing muon momentum distribution (p_μ), outgoing muon angle with respect to the initial neutrino direction distribution (θ_μ), outgoing pion angle with respect to the initial neutrino direction distribution (θ_π) and distribution of the angle between the outgoing muon and pion ($\theta_{\mu\pi}$).

Table 4.7: The measured differential cross sections in p_μ, θ_μ, θ_π and $\theta_{\mu\pi}$ for muon neutrino interactions in argon. Central bin value and both statistical (first) and systematic (second) errors are shown.

p_μ [GeV/c]	$d\sigma/dp_\mu$ (ν_μ) [10^{-37} cm^2/(GeV/c)/nucleon]
0-3	$3.81 \pm 1.98\ ^{+1.49}_{-1.04}$
3-6	$5.22 \pm 1.46\ ^{+0.84}_{-0.95}$
6-12	$3.65 \pm 0.89\ ^{+0.79}_{-0.68}$
12-21	$0.57 \pm 0.39\ ^{+0.17}_{-0.18}$
21-30	$0.37 \pm 0.24\ ^{+0.09}_{-0.06}$

θ_μ [degrees]	$d\sigma/d\theta_\mu$ (ν_μ) [10^{-37} cm^2/degree/nucleon]
0-8	$3.46 \pm 0.83\ ^{+0.62}_{-0.64}$
8-16	$2.54 \pm 0.60\ ^{+0.48}_{-0.47}$
16-24	$0.93 \pm 0.43\ ^{+0.31}_{-0.22}$
24-60	$0.09 \pm 0.13\ ^{+0.05}_{-0.06}$

θ_π [degrees]	$d\sigma/d\theta_\pi$ (ν_μ) [10^{-37} cm^2/degree/nucleon]
0-25	$0.58 \pm 0.27\ ^{+0.22}_{-0.13}$
25-50	$0.55 \pm 0.17\ ^{+0.15}_{-0.15}$
50-75	$1.01 \pm 0.21\ ^{+0.15}_{-0.17}$
75-125	$0.17 \pm 0.08\ ^{+0.04}_{-0.03}$
125-180	$0.02 \pm 0.04\ ^{+0.01}_{-0.01}$

$\theta_{\mu\pi}$ [degrees]	$d\sigma/d\theta_{\mu\pi}$ (ν_μ) [10^{-37} cm^2/degree/nucleon]
0-24	$0.17 \pm 0.20\ ^{+0.13}_{-0.04}$
24-48	$0.84 \pm 0.21\ ^{+0.20}_{-0.17}$
48-72	$0.67 \pm 0.19\ ^{+0.14}_{-0.18}$
72-105	$0.40 \pm 0.13\ ^{+0.08}_{-0.07}$
105-142	$0.15 \pm 0.08\ ^{+0.03}_{-0.02}$
142-180	$0.04 \pm 0.05\ ^{+0.01}_{-0.01}$

Table 4.8: The measured differential cross sections in p_μ, θ_μ, θ_π and $\theta_{\mu\pi}$ for muon antineutrino interactions in argon. Central bin value and both statistical (first) and systematic (second) errors are shown.

p_μ [GeV/c]	$d\sigma/dp_\mu$ $(\bar{\nu}_\mu)$ $[10^{-38}$ cm^2/(GeV/c)/nucleon]
0-3	3.23 ± 0.50 $^{+0.46}_{-0.44}$
3-6	2.05 ± 0.35 $^{+0.23}_{-0.27}$
6-9	0.58 ± 0.21 $^{+0.08}_{-0.08}$
9-15	0.15 ± 0.09 $^{+0.03}_{-0.02}$

θ_μ [degrees]	$d\sigma/d\theta_\mu$ $(\bar{\nu}_\mu)$ $[10^{-38}$ cm^2/degree/nucleon]
0-5	0.70 ± 0.18 $^{+0.11}_{-0.16}$
5-10	0.90 ± 0.19 $^{+0.10}_{-0.12}$
10-15	1.00 ± 0.18 $^{+0.12}_{-0.13}$
15-20	0.62 ± 0.15 $^{+0.08}_{-0.10}$
20-25	0.21 ± 0.11 $^{+0.06}_{-0.04}$
25-40	0.08 ± 0.05 $^{+0.02}_{-0.02}$

θ_π [degrees]	$d\sigma/d\theta_\pi$ $(\bar{\nu}_\mu)$ $[10^{-38}$ cm^2/degree/nucleon]
0-18	0.13 ± 0.05 $^{+0.02}_{-0.02}$
18-36	0.15 ± 0.04 $^{+0.02}_{-0.02}$
36-54	0.19 ± 0.04 $^{+0.03}_{-0.03}$
54-72	0.20 ± 0.05 $^{+0.02}_{-0.03}$
72-90	0.13 ± 0.04 $^{+0.02}_{-0.02}$
90-108	0.10 ± 0.04 $^{+0.01}_{-0.03}$
108-126	0.13 ± 0.04 $^{+0.01}_{-0.02}$
126-144	0.04 ± 0.02 $^{+0.01}_{-0.01}$
144-180	0.03 ± 0.02 $^{+0.00}_{-0.01}$

$\theta_{\mu\pi}$ [degrees]	$d\sigma/d\theta_{\mu\pi}$ $(\bar{\nu}_\mu)$ $[10^{-38}$ cm^2/degree/nucleon]
0-18	0.06 ± 0.04 $^{+0.02}_{-0.01}$
18-36	0.18 ± 0.04 $^{+0.02}_{-0.03}$
36-54	0.15 ± 0.04 $^{+0.03}_{-0.02}$
54-72	0.22 ± 0.05 $^{+0.03}_{-0.03}$
72-90	0.16 ± 0.04 $^{+0.03}_{-0.02}$
90-108	0.12 ± 0.04 $^{+0.01}_{-0.02}$
108-126	0.09 ± 0.03 $^{+0.01}_{-0.01}$
126-144	0.08 ± 0.03 $^{+0.01}_{-0.01}$
144-180	0.03 ± 0.02 $^{+0.00}_{-0.01}$

ArgoNeuT measurements and expectations for the total cross sections for different neutrino MC generator are shown in Table 4.9. As reported in Section 4.5.4, GiBUU is the MC generator that better describes the results of this analysis, while the other three generators (NuWro, NEUT and GENIE) largely overestimate the measured cross sections.

Table 4.9: Comparison between measured total cross sections and MC generators expectations for both, neutrino and antineutrino.

	Total CC1π cross section	
	ν_μ $[10^{-37}$ cm^2/Ar]	$\overline{\nu}_\mu$ $[10^{-38}$ cm^2/Ar]
ArgoNeuT data	2.5 ± 0.4 (stat) ± 0.5 (syst)	8.2 ± 0.9 (stat) $^{+0.9}_{-1.1}$ (syst)
GENIE	3.9	13.8
NuWro	3.4	11.1
GiBUU	2.6	7.4
NEUT	3.6	11.5

Conclusions

Future short and long-baseline precise neutrino oscillation experiments in the US are based on the liquid argon TPC technology. Knowledge of neutrino interactions on argon nuclei are mandatory to reduce the most important systematic uncertainty in oscillation measurements. In this thesis, a sample of single pion production charged-current interaction events is identified in the ArgoNeuT detector and the cross section values, for muon neutrino and antineutrino interactions, are measured. This process is one of the most relevant in the energy regime of oscillation experiments. The analysis is based on a set of selective cuts and a Booster Decision Tree with Gradient classification for the identification of the relevant events. The signal is extracted subtracting the Monte Carlo background estimation. The analysis results very robust as small differences in the final results are found changing the tuned cuts, the training samples dimensions and the histogram binning in the scaling fit. The reported measurements of the differential and total cross section for single pion production charged-current interaction events are a demonstration of the capabilities of the liquid argon technology. The total cross sections measured are found to be $\langle \sigma_{\nu_\mu} \rangle = 2.5 \pm 0.4(stat) \pm 0.5(syst) \times 10^{-37} cm^2/Ar$ for neutrinos at a mean energy of 9.6 GeV and $\langle \sigma_{\overline{\nu}_\mu} \rangle = 8.2 \pm 0.9(stat)^{+0.9}_{-1.1}(syst) \times 10^{-38} cm^2/Ar$ for antineutrinos at a mean energy of 3.6 GeV.

Measured differential and total cross sections have been extensively compared with the expectations from different neutrino Monte Carlo generators. Expectations results to be very different from each other and only one generator reproduces well the ArgoNeuT measurements (GIBUU). The other three generators (NuWro, NEUT and GENIE) greatly overestimate the measured cross sections. Although model testing is not the goal of this analysis, these results will contribute to the neutrino physics community as input for the tuning of the Monte Carlo generators. The ArgoNeuT neutrino data sample is limited and the low number of events available is a limiting factor. Nevertheless, this first measurement of the process in argon with a fully automated reconstruction is very important. The capabilities of the liquid argon TPC are well exploited in the analysis. Other large mass liquid argon

TPC experiments in the Short-Baseline Neutrino program at Fermilab, such as MicroBooNE and SBND, will perform the same measurement presented in this thesis with the improved factor of a much larger statistic in the data collection. The demonstrated capability to produce automated analysis of liquid argon data is a necessary feature following the increasing number of neutrino interactions expected in future experiments.

This is the first time this cross section is measured in a liquid argon TPC. The analysis method developed in this thesis, based on the use of a Multivariate Analysis to separate signal and background, will be applied to those future measurements. The results of the analysis are reported in an ArgoNeuT internal note [99]. A paper to be submitted to Physical Review D is under review by the ArgoNeuT collaboration.

Bibliography

[1] E. Fermi. "An attempt of a theory of beta radiation." In: *Z. Phys.* 88 (1934), pp. 161–177. DOI: 10.1007/BF01351864.

[2] C. L. Cowan et al. "Detection of the free neutrino: A Confirmation". In: *Science* 124 (1956), pp. 103–104. DOI: 10.1126/science.124.3212.103.

[3] G. Danby et al. "Observation of High-Energy Neutrino Reactions and the Existence of Two Kinds of Neutrinos". In: *Phys. Rev. Lett.* 9 (1962), pp. 36–44. DOI: 10.1103/PhysRevLett.9.36.

[4] K. Kodama et al. "Observation of tau neutrino interactions". In: *Phys. Lett.* B504 (2001), pp. 218–224. DOI: 10.1016/S0370-2693(01)00307-0. arXiv: hep-ex/0012035 [hep-ex].

[5] John N. Bahcall, Aldo M. Serenelli, and Sarbani Basu. "New solar opacities, abundances, helioseismology, and neutrino fluxes". In: *Astrophys. J.* 621 (2005), pp. L85–L88. DOI: 10.1086/428929. arXiv: astro-ph/0412440 [astro-ph].

[6] Raymond Davis Jr., Don S. Harmer, and Kenneth C. Hoffman. "Search for neutrinos from the sun". In: *Phys. Rev. Lett.* 20 (1968), pp. 1205–1209. DOI: 10.1103/PhysRevLett.20.1205.

[7] Q. R. Ahmad et al. "Direct evidence for neutrino flavor transformation from neutral current interactions in the Sudbury Neutrino Observatory". In: *Phys. Rev. Lett.* 89 (2002), p. 011301. DOI: 10.1103/PhysRevLett.89.011301. arXiv: nucl-ex/0204008 [nucl-ex].

[8] Y. Fukuda et al. "Evidence for oscillation of atmospheric neutrinos". In: *Phys. Rev. Lett.* 81 (1998), pp. 1562–1567. DOI: 10.1103/PhysRevLett.81.1562. arXiv: hep-ex/9807003 [hep-ex].

[9] W. Hampel et al. "Final results of the Cr-51 neutrino source experiments in GALLEX". In: *Phys. Lett.* B420 (1998), pp. 114–126. DOI: 10.1016/S0370-2693(97)01562-1.

[10] L. Bornschein. "The KATRIN experiment - a direct measurement of the electron antineutrino mass in the sub-eV region". In: *Nuclear Physics A* 752 (2005), pp. 14 –23. ISSN: 0375-9474. DOI: http://dx.doi.org/10.1016/j. nuclphysa.2005.02.105. URL: http://www.sciencedirect.com/science/ article/pii/S0375947405001478.

[11] S. Mertens et al. "Sensitivity of Next-Generation Tritium Beta-Decay Experiments for keV-Scale Sterile Neutrinos". In: *JCAP* 1502.02 (2015), p. 020. DOI: 10.1088/1475-7516/2015/02/020. arXiv: 1409.0920 [physics.ins-det].

[12] L. Montanet et al. "Review of particle properties. Particle Data Group". In: *Phys. Rev.* D50 (1994), pp. 1173–1823. DOI: 10.1103/PhysRevD.50.1173.

[13] K. S. Hirata et al. "Observation in the Kamiokande-II Detector of the Neutrino Burst from Supernova SN 1987a". In: *Phys. Rev.* D38 (1988), pp. 448–458. DOI: 10.1103/PhysRevD.38.448.

[14] J. Adam et al. "New limit on the lepton-flavour violating decay $\mu^+ \rightarrow e^+\gamma$". In: *Phys. Rev. Lett.* 107 (2011), p. 171801. DOI: 10.1103/PhysRevLett.107. 171801. arXiv: 1107.5547 [hep-ex].

[15] Samoil M. Bilenky and B. Pontecorvo. "Lepton Mixing and Neutrino Oscillations". In: *Phys. Rept.* 41 (1978), pp. 225–261. DOI: 10.1016/0370-1573(78) 90095-9.

[16] Ziro Maki, Masami Nakagawa, and Shoichi Sakata. "Remarks on the unified model of elementary particles". In: *Prog. Theor. Phys.* 28 (1962), pp. 870–880. DOI: 10.1143/PTP.28.870.

[17] K.A. Olive and Particle Data Group. "Review of Particle Physics". In: *Chinese Physics C* 38.9 (2014), p. 090001. URL: http://stacks.iop.org/1674- 1137/38/i=9/a=090001.

[18] J. N. Bahcall and R. Davis Jr. "Solar Neutrinos: A Scientific Puzzle". In: *Science* 191 (Jan. 1976), pp. 264–267. DOI: 10.1126/science.191.4224.264.

[19] Y. Fukuda et al. "Solar neutrino data covering solar cycle 22". In: *Phys. Rev. Lett.* 77 (1996), pp. 1683–1686. DOI: 10.1103/PhysRevLett.77.1683.

[20] V. N. Gavrin. "Measurement of the solar neutrino capture rate in SAGE and the value of the pp-neutrino flux at the earth". In: *Nucl. Phys. Proc. Suppl.* 138 (2005). [,87(2005)], pp. 87–90. DOI: 10.1016/j.nuclphysbps.2004.11.021.

[21] P. Anselmann et al. "Solar neutrinos observed by GALLEX at Gran Sasso." In: *Phys. Lett.* B285 (1992), pp. 376–389. DOI: 10.1016/0370-2693(92)91521-A.

[22] M. Altmann et al. "Complete results for five years of GNO solar neutrino observations". In: *Phys. Lett.* B616 (2005), pp. 174–190. DOI: `10.1016/j.physletb.2005.04.068`. arXiv: `hep-ex/0504037 [hep-ex]`.

[23] S. Fukuda et al. "Determination of solar neutrino oscillation parameters using 1496 days of Super-Kamiokande I data". In: *Phys. Lett.* B539 (2002), pp. 179–187. DOI: `10.1016/S0370-2693(02)02090-7`. arXiv: `hep-ex/0205075 [hep-ex]`.

[24] Q. R. Ahmad et al. "Measurement of the rate of $\nu_e + d \to p + p + e^-$ interactions produced by ^8B solar neutrinos at the Sudbury Neutrino Observatory". In: *Phys. Rev. Lett.* 87 (2001), p. 071301. DOI: `10.1103/PhysRevLett.87.071301`. arXiv: `nucl-ex/0106015 [nucl-ex]`.

[25] Arthur B. McDonald John N. Bahcall Frank Calaprice and Yoji Totsuka. "Solar neutrino experiments: The next generation". In: *Physics Today* 49 (1996), pp. 30–36.

[26] L. Wolfenstein. "Neutrino Oscillations in Matter". In: *Phys. Rev.* D17 (1978), pp. 2369–2374. DOI: `10.1103/PhysRevD.17.2369`.

[27] S. Abe et al. "Precision Measurement of Neutrino Oscillation Parameters with KamLAND". In: *Phys. Rev. Lett.* 100 (2008), p. 221803. DOI: `10.1103/PhysRevLett.100.221803`. arXiv: `0801.4589 [hep-ex]`.

[28] A. Gando et al. "Constraints on θ_{13} from A Three-Flavor Oscillation Analysis of Reactor Antineutrinos at KamLAND". In: *Phys. Rev.* D83 (2011), p. 052002. DOI: `10.1103/PhysRevD.83.052002`. arXiv: `1009.4771 [hep-ex]`.

[29] Vassily Plyaskin. "Calculation of atmospheric neutrino flux". In: *Phys. Lett.* B516 (2001), pp. 213–235. DOI: `10.1016/S0370-2693(01)00907-8`. arXiv: `hep-ph/0103286 [hep-ph]`.

[30] K. Abe et al. "Evidence for the Appearance of Atmospheric Tau Neutrinos in Super-Kamiokande". In: *Phys. Rev. Lett.* 110.18 (2013), p. 181802. DOI: `10.1103/PhysRevLett.110.181802`. arXiv: `1206.0328 [hep-ex]`.

[31] M. H. Ahn et al. "Measurement of Neutrino Oscillation by the K2K Experiment". In: *Phys. Rev.* D74 (2006), p. 072003. DOI: `10.1103/PhysRevD.74.072003`. arXiv: `hep-ex/0606032 [hep-ex]`.

[32] P. Adamson et al. "Measurement of the Neutrino Mass Splitting and Flavor Mixing by MINOS". In: *Phys. Rev. Lett.* 106 (2011), p. 181801. DOI: `10.1103/PhysRevLett.106.181801`. arXiv: `1103.0340 [hep-ex]`.

[33] P. Adamson et al. "Measurements of atmospheric neutrinos and antineutrinos in the MINOS Far Detector". In: *Phys. Rev.* D86 (2012), p. 052007. DOI: 10.1103/PhysRevD.86.052007. arXiv: 1208.2915 [hep-ex].

[34] K. Abe et al. "Precise Measurement of the Neutrino Mixing Parameter theta-23 from Muon Neutrino Disappearance in an Off-Axis Beam". In: *Phys. Rev. Lett.* 112.18 (2014), p. 181801. DOI: 10.1103/PhysRevLett.112.181801. arXiv: 1403.1532 [hep-ex].

[35] P. Adamson et al. "First measurement of electron neutrino appearance in NOvA". In: *Phys. Rev. Lett.* 116.15 (2016), p. 151806. DOI: 10.1103/PhysRevLett.116.151806. arXiv: 1601.05022 [hep-ex].

[36] F. Ardellier et al. "Letter of intent for Double-CHOOZ: A Search for the mixing angle theta(13)". In: (2004). arXiv: hep-ex/0405032 [hep-ex].

[37] Y. Abe et al. "Indication of Reactor $\bar{\nu}_e$ Disappearance in the Double Chooz Experiment". In: *Phys. Rev. Lett.* 108 (2012), p. 131801. DOI: 10.1103/PhysRevLett.108.131801. arXiv: 1112.6353 [hep-ex].

[38] F. P. An et al. "Observation of electron-antineutrino disappearance at Daya Bay". In: *Phys. Rev. Lett.* 108 (2012), p. 171803. DOI: 10.1103/PhysRevLett.108.171803. arXiv: 1203.1669 [hep-ex].

[39] J. K. Ahn et al. "Observation of Reactor Electron Antineutrino Disappearance in the RENO Experiment". In: *Phys. Rev. Lett.* 108 (2012), p. 191802. DOI: 10.1103/PhysRevLett.108.191802. arXiv: 1204.0626 [hep-ex].

[40] F. P. An et al. "New Measurement of Antineutrino Oscillation with the Full Detector Configuration at Daya Bay". In: *Phys. Rev. Lett.* 115.11 (2015), p. 111802. DOI: 10.1103/PhysRevLett.115.111802. arXiv: 1505.03456 [hep-ex].

[41] J. A. Formaggio and G. P. Zeller. "From eV to EeV: Neutrino Cross Sections Across Energy Scales". In: *Rev. Mod. Phys.* 84 (2012), pp. 1307–1341. DOI: 10.1103/RevModPhys.84.1307. arXiv: 1305.7513 [hep-ex].

[42] Joachim Kopp et al. "Sterile Neutrino Oscillations: The Global Picture". In: *JHEP* 05 (2013), p. 050. DOI: 10.1007/JHEP05(2013)050. arXiv: 1303.3011 [hep-ph].

[43] C. Giunti et al. "Pragmatic View of Short-Baseline Neutrino Oscillations". In: *Phys. Rev.* D88 (2013), p. 073008. DOI: 10.1103/PhysRevD.88.073008. arXiv: 1308.5288 [hep-ph].

[44] C. Athanassopoulos et al. "Candidate events in a search for anti-muon-neutrino —¿ anti-electron-neutrino oscillations". In: *Phys. Rev. Lett.* 75 (1995), pp. 2650–2653. DOI: `10.1103/PhysRevLett.75.2650`. arXiv: `nucl-ex/9504002 [nucl-ex]`.

[45] A. A. Aguilar-Arevalo et al. "Improved Search for $\bar{\nu}_\mu \to \bar{\nu}_e$ Oscillations in the MiniBooNE Experiment". In: *Phys. Rev. Lett.* 110 (2013), p. 161801. DOI: `10.1103/PhysRevLett.110.161801`. arXiv: `1303.2588 [hep-ex]`.

[46] Carlo Giunti and Marco Laveder. "Statistical Significance of the Gallium Anomaly". In: *Phys. Rev.* C83 (2011), p. 065504. DOI: `10.1103/PhysRevC.83.065504`. arXiv: `1006.3244 [hep-ph]`.

[47] G. Mention et al. "The Reactor Antineutrino Anomaly". In: *Phys. Rev.* D83 (2011), p. 073006. DOI: `10.1103/PhysRevD.83.073006`. arXiv: `1101.2755 [hep-ex]`.

[48] Feng Peng An et al. "Measurement of the Reactor Antineutrino Flux and Spectrum at Daya Bay". In: *Phys. Rev. Lett.* 116.6 (2016). [Erratum: Phys. Rev. Lett.118,no.9,099902(2017)], p. 061801. DOI: `10.1103/PhysRevLett.116.061801,10.1103/PhysRevLett.118.099902`. arXiv: `1508.04233 [hep-ex]`.

[49] A. A. Aguilar-Arevalo et al. "The Neutrino Flux prediction at MiniBooNE". In: *Phys. Rev.* D79 (2009), p. 072002. DOI: `10.1103/PhysRevD.79.072002`. arXiv: `0806.1449 [hep-ex]`.

[50] T. S. Nigmanov et al. "Electromagnetic and hadron calorimeters in the MIPP experiment". In: *Nucl. Instrum. Meth.* A598 (2009), pp. 394–399. DOI: `10.1016/j.nima.2008.08.153`. arXiv: `0903.2463 [physics.ins-det]`.

[51] C. Alt et al. "Inclusive production of charged pions in p+C collisions at 158-GeV/c beam momentum". In: *Eur. Phys. J.* C49 (2007), pp. 897–917. DOI: `10.1140/epjc/s10052-006-0165-7`. arXiv: `hep-ex/0606028 [hep-ex]`.

[52] L. Aliaga et al. "Neutrino Flux Predictions for the NuMI Beam". In: *Phys. Rev.* D94.9 (2016). [Addendum: Phys. Rev.D95,no.3,039903(2017)], p. 092005. DOI: `10.1103/PhysRevD.94.092005,10.1103/PhysRevD.95.039903`. arXiv: `1607.00704 [hep-ex]`.

[53] Christian Lippmann. "Performance of the ALICE Time Projection Chamber". In: *Physics Procedia* 37 (2012), pp. 434 –441. ISSN: 1875-3892. DOI: `http://dx.doi.org/10.1016/j.phpro.2012.02.390`. URL: `http://www.sciencedirect.com/science/article/pii/S187538921201721X`.

[54] V. A. Andreev et al. "Muon Capture on the Deuteron – The MuSun Experiment". In: (2010). arXiv: 1004.1754 [nucl-ex].

[55] D. S. Akerib et al. "The Large Underground Xenon (LUX) Experiment". In: *Nucl. Instrum. Meth.* A704 (2013), pp. 111–126. DOI: 10.1016/j.nima.2012.11.135. arXiv: 1211.3788 [physics.ins-det].

[56] W. J. Willis and V. Radeka. "Liquid Argon Ionization Chambers as Total Absorption Detectors". In: *Nucl. Instrum. Meth.* 120 (1974), pp. 221–236. DOI: 10.1016/0029-554X(74)90039-1.

[57] C. Rubbia. "The Liquid Argon Time Projection Chamber: A New Concept for Neutrino Detectors". In: (1977).

[58] Paul Musset and Jean-Pierre Vialle. "Neutrino physics with gargamelle". In: *Physics Reports* 39.1 (1978), pp. 1 –130. ISSN: 0370-1573. DOI: http://dx.doi.org/10.1016/0370-1573(78)90051-0. URL: http://www.sciencedirect.com/science/article/pii/0370157378900510.

[59] T. Heindl et al. "The scintillation of liquid argon". In: *Europhys. Lett.* 91 (2010), p. 62002. DOI: 10.1209/0295-5075/91/62002. arXiv: 1511.07718 [physics.ins-det].

[60] A. N. Kalinovsky, N. V. Mokhov, and Yu. P. Nikitin. *PASSAGE OF HIGH-ENERGY PARTICLES THROUGH MATTER.* 1989.

[61] R. Acciarri et al. "A study of electron recombination using highly ionizing particles in the ArgoNeuT Liquid Argon TPC". In: *JINST* 8 (2013), P08005. DOI: 10.1088/1748-0221/8/08/P08005. arXiv: 1306.1712 [physics.ins-det].

[62] R. Acciarri et al. "Measurements of Inclusive Muon Neutrino and Antineutrino Charged Current Differential Cross Sections on Argon in the NuMI Antineutrino Beam". In: *Phys. Rev.* D89.11 (2014), p. 112003. DOI: 10.1103/PhysRevD.89.112003. arXiv: 1404.4809 [hep-ex].

[63] C. Anderson et al. "Analysis of a Large Sample of Neutrino-Induced Muons with the ArgoNeuT Detector". In: *JINST* 7 (2012), P10020. DOI: 10.1088/1748-0221/7/10/P10020. arXiv: 1205.6702 [physics.ins-det].

[64] R. Acciarri et al. "Detection of back-to-back proton pairs in charged-current neutrino interactions with the ArgoNeuT detector in the NuMI low energy beam line". In: *Phys. Rev.* D90.1 (2014), p. 012008. DOI: 10.1103/PhysRevD.90.012008. arXiv: 1405.4261 [nucl-ex].

[65] R. Acciarri et al. "First Measurement of Neutrino and Antineutrino Coherent Charged Pion Production on Argon". In: *Phys. Rev. Lett.* 113.26 (2014). [erratum: Phys. Rev. Lett.114,no.3,039901(2015)], p. 261801. DOI: `10.1103/PhysRevLett.113.261801,10.1103/PhysRevLett.114.039901`. arXiv: `1408.0598 [hep-ex]`.

[66] R. Acciarri et al. "First Observation of Low Energy Electron Neutrinos in a Liquid Argon Time Projection Chamber". In: *Phys. Rev.* D95.7 (2017). [Phys. Rev.D95,072005(2017)], p. 072005. DOI: `10.1103/PhysRevD.95.072005`. arXiv: `1610.04102 [hep-ex]`.

[67] C. Anderson et al. "The ArgoNeuT Detector in the NuMI Low-Energy beam line at Fermilab". In: *JINST* 7 (2012), P10019. DOI: `10.1088/1748-0221/7/10/P10019`. arXiv: `1205.6747 [physics.ins-det]`.

[68] K. Anderson et al. "The NuMI Facility Technical Design Report". In: (1998).

[69] D. G. Michael et al. "The Magnetized steel and scintillator calorimeters of the MINOS experiment". In: *Nucl. Instrum. Meth.* A596 (2008), pp. 190–228. DOI: `10.1016/j.nima.2008.08.003`. arXiv: `0805.3170 [physics.ins-det]`.

[70] Eric D. Church. "LArSoft: A Software Package for Liquid Argon Time Projection Drift Chambers". In: (2013). arXiv: `1311.6774 [physics.ins-det]`.

[71] M. Antonello et al. "Precise 3D track reconstruction algorithm for the ICARUS T600 liquid argon time projection chamber detector". In: *Adv. High Energy Phys.* 2013 (2013), p. 260820. DOI: `10.1155/2013/260820`. arXiv: `1210.5089 [physics.ins-det]`.

[72] James Strait et al. "Long-Baseline Neutrino Facility (LBNF) and Deep Underground Neutrino Experiment (DUNE)". In: (2016). arXiv: `1601.05823 [physics.ins-det]`.

[73] H. Chen et al. "Proposal for a New Experiment Using the Booster and NuMI Neutrino Beamlines: MicroBooNE". In: (2007).

[74] A. A. Aguilar-Arevalo et al. "The MiniBooNE Detector". In: *Nucl. Instrum. Meth.* A599 (2009), pp. 28–46. DOI: `10.1016/j.nima.2008.10.028`. arXiv: `0806.4201 [hep-ex]`.

[75] Scanavini G. *Expectation for neutrino charged-current 0 pion and 1 pion events and neutrino-electron elastic scattering events in SBND*. SBND Internal Note, SBN-doc-874-v1, 2015.

[76]   P. Cennini et al. "Performance of a 3-ton liquid argon time projection chamber". In: *Nucl. Instrum. Meth.* A345 (1994), pp. 230–243. DOI: 10.1016/0168-9002(94)90996-2.

[77]   F. Arneodo et al. "First observation of 140-cm drift ionizing tracks in the ICARUS liquid-argon TPC". In: *Nucl. Instrum. Meth.* A449 (2000), pp. 36–41. DOI: 10.1016/S0168-9002(99)01296-6.

[78]   P Cennini et al. "Detection of scintillation light in coincidence with ionizing tracks in a liquid argon time projection chamber". In: *Nuclear Instruments and Methods in Physics Research Section A: Accelerators, Spectrometers, Detectors and Associated Equipment* 432.2–3 (1999), pp. 240 –248. ISSN: 0168-9002. DOI: https://doi.org/10.1016/S0168-9002(99)00519-7. URL: http://www.sciencedirect.com/science/article/pii/S0168900299005197.

[79]   S. Amerio et al. "Design, construction and tests of the ICARUS T600 detector". In: *Nucl. Instrum. Meth.* A527 (2004), pp. 329–410. DOI: 10.1016/j.nima.2004.02.044.

[80]   A. A. Aguilar-Arevalo et al. "First Measurement of the Muon Neutrino Charged Current Quasielastic Double Differential Cross Section". In: *Phys. Rev.* D81 (2010), p. 092005. DOI: 10.1103/PhysRevD.81.092005. arXiv: 1002.2680 [hep-ex].

[81]   A. A. Aguilar-Arevalo et al. "Measurement of the Neutrino Neutral-Current Elastic Differential Cross Section on Mineral Oil at $E_\nu \sim 1$ GeV". In: *Phys. Rev.* D82 (2010), p. 092005. DOI: 10.1103/PhysRevD.82.092005. arXiv: 1007.4730 [hep-ex].

[82]   M. Martini, M. Ericson, and G. Chanfray. "Neutrino quasielastic interaction and nuclear dynamics". In: *Phys. Rev.* C84 (2011), p. 055502. DOI: 10.1103/PhysRevC.84.055502. arXiv: 1110.0221 [nucl-th].

[83]   J. Nieves, I. Ruiz Simo, and M. J. Vicente Vacas. "Inclusive Charged-Current Neutrino-Nucleus Reactions". In: *Phys. Rev.* C83 (2011), p. 045501. DOI: 10.1103/PhysRevC.83.045501. arXiv: 1102.2777 [hep-ph].

[84]   A. Bodek, H. S. Budd, and M. E. Christy. "Neutrino Quasielastic Scattering on Nuclear Targets: Parametrizing Transverse Enhancement (Meson Exchange Currents)". In: *Eur. Phys. J.* C71 (2011), p. 1726. DOI: 10.1140/epjc/s10052-011-1726-y. arXiv: 1106.0340 [hep-ph].

[85] O. Lalakulich, K. Gallmeister, and U. Mosel. "Many-Body Interactions of Neutrinos with Nuclei - Observables". In: *Phys. Rev.* C86.1 (2012). [Erratum: Phys. Rev.C90,no.2,029902(2014)], p. 014614. DOI: 10.1103/PhysRevC.86.014614, 10.1103/PhysRevC.90.029902. arXiv: 1203.2935 [nucl-th].

[86] M. B. Barbaro et al. "Superscaling in electron-nucleus scattering and its link to CC and NC QE neutrino-nucleus scattering". In: *AIP Conf. Proc.* 1663 (2015), p. 090002. DOI: 10.1063/1.4919497. arXiv: 1303.6508 [nucl-th].

[87] S. Agostinelli et al. "GEANT4: A Simulation toolkit". In: *Nucl. Instrum. Meth.* A506 (2003), pp. 250–303. DOI: 10.1016/S0168-9002(03)01368-8.

[88] C. Andreopoulos et al. "The GENIE Neutrino Monte Carlo Generator". In: *Nucl. Instrum. Meth.* A614 (2010), pp. 87–104. DOI: 10.1016/j.nima.2009.12.009. arXiv: 0905.2517 [hep-ph].

[89] René Brun et al. "GEANT Detector Description and Simulation Tool". In: (1994).

[90] Jakub Żmuda et al. "NuWro Monte Carlo generator of neutrino interactions - first electron scattering results". In: *Acta Phys. Polon.* B46.11 (2015), p. 2329. DOI: 10.5506/APhysPolB.46.2329. arXiv: 1510.03268 [hep-ph].

[91] *GiBUU MC generator.* http://gibuu.hepforge.org.

[92] Yoshinari Hayato. "A neutrino interaction simulation program library NEUT". In: *Acta Phys. Polon.* B40 (2009), pp. 2477–2489.

[93] Andreas Hocker et al. "TMVA - Toolkit for Multivariate Data Analysis". In: *PoS* ACAT (2007), p. 040. arXiv: physics/0703039 [PHYSICS].

[94] Byron P. Roe et al. "Boosted decision trees, an alternative to artificial neural networks". In: *Nucl. Instrum. Meth.* A543.2-3 (2005), pp. 577–584. DOI: 10.1016/j.nima.2004.12.018. arXiv: physics/0408124 [physics].

[95] K. Abe et al. "First measurement of the muon neutrino charged current single pion production cross section on water with the T2K near detector". In: *Phys. Rev.* D95.1 (2017), p. 012010. DOI: 10.1103/PhysRevD.95.012010. arXiv: 1605.07964 [hep-ex].

[96] *ROOT TFractionFitter class reference.* https://root.cern.ch/doc/master/classTFractionFitter.html.

[97] P. Adamson et al. "Neutrino and Antineutrino Inclusive Charged-current Cross Section Measurements with the MINOS Near Detector". In: *Phys. Rev.* D81 (2010), p. 072002. DOI: 10.1103/PhysRevD.81.072002. arXiv: 0910.2201 [hep-ex].

[98] Costas Andreopoulos et al. "The GENIE Neutrino Monte Carlo Generator: Physics and User Manual". In: (2015). arXiv: `1510.05494 [hep-ph]`.

[99] Yang T. Scanavini G. Palamara O. *First Measurement of Single Charged Pion Production in Charged Current Neutrino and Antineutrino Events on Argon.* ArgoNeuT Internal Note, Projects-doc-3954-v1, 2017.